

Iron nanostructures studied by spin-polarised scanning tunneling microscopy

Dissertation
zur Erlangung des Doktorgrades
des Fachbereichs Physik
der Universität Hamburg

vorgelegt von
Kirsten von Bergmann
aus Bonn

Hamburg
2004

Gutachter der Dissertation:
Prof. Dr. R. Wiesendanger
Prof. Dr. R. L. Johnson
Prof. Dr. V. Moshchalkov

Gutachter der Disputation:
Prof. Dr. R. Wiesendanger
Prof. Dr. H. P. Oepen

Datum der Disputation:
08.04.2004

Vorsitzender des Prüfungsausschusses:
Priv.-Doz. Dr. D. Grundler

Vorsitzender des Promotionsausschusses:
Prof. Dr. R. Wiesendanger

Dekan des Fachbereichs Physik:
Prof. Dr. G. Huber

Abstract

Scanning tunneling microscopy (STM) is a powerful tool to study the interplay between structural, electronic and magnetic properties with high spatial and energy resolution. In this thesis iron (Fe) nanostructures on tungsten (W) single crystals are investigated.

A systematic study of the well-known helical magnetic structure of Fe double-layer stripes on W(110) proves that domain walls always run approximately along the $[1\bar{1}0]$ direction regardless of the orientation of the substrate miscut. The magnetic structure of the double-layer of Fe on W(110) is unchanged by the adsorption of single oxygen atoms. In the vicinity of isolated oxygen impurities energy-dependent spatial variations of the local density of states (LDOS) are observed. They are interpreted as electron standing waves and compared to spin-resolved electronic structure calculations. The result is the assignment of the observed LDOS oscillations to scattering states involving minority-spin bands of *d*-like character. Spin-polarised (SP) measurements show that they are only observed on one particular type of magnetic domain, confirming the unique ability of SP-STM to study the spin character of electronic states together with their orbital symmetry.

The investigation of the system of Fe on W(001) shows a layer-dependent electronic structure in the low coverage regime. The domain structure in the pseudomorphic growth regime is studied and the fourfold anisotropy can be directly deduced from differential conductance maps. Quantitative analysis shows a layer-dependent magnetic easy axis which is along $\langle 110 \rangle$ for the second and third monolayer, but along $\langle 100 \rangle$ for the fourth monolayer. The capability of the STM to distinguish between up to eight different magnetic directions with spatial resolution demonstrates the efficiency of this method to study the magnetism of systems with reduced dimensions.

Inhaltsangabe

Rastertunnelmikroskopie (STM) ist eine leistungsstarke Methode um das Zusammenspiel von strukturellen, elektronischen und magnetischen Eigenschaften mit hoher Orts- und Energieauflösung zu erforschen. In dieser Arbeit werden Eisen (Fe) Nanostrukturen auf Wolfram (W) Einkristallen untersucht.

Eine systematische Studie der gut bekannten helikalen magnetischen Struktur von Fe-Doppellagenstreifen auf W(110) zeigt, dass Domänenwände immer ungefähr entlang der $[1\bar{1}0]$ Richtung verlaufen, unabhängig von der Orientierung des Substratfehlschnitts. Die magnetische Struktur der Doppellage Fe auf W(110) bleibt unverändert bei der Adsorption von einzelnen Sauerstoffatomen. In der Umgebung isolierter Sauerstoffadsorbate werden energieabhängige räumliche Variationen der lokalen Zustandsdichte (LDOS) beobachtet. Diese werden als stehende Elektronenwellen interpretiert und mit Rechnungen der spinabhängigen elektronischen Struktur verglichen. Das Ergebnis ist eine Zuordnung der beobachteten LDOS-Oszillationen zu Streuzuständen unter Beteiligung von Minoritäts-Spin Bändern mit d -ähnlichem Charakter. Spinpolarisierte Messungen zeigen, dass sie nur auf der einen Domänenart beobachtet werden. Dies bestätigt die einzigartige Fähigkeit der spinpolarisierten Rastertunnelmikroskopie, den Spincharakter von elektronischen Zuständen zusammen mit der orbitalen Symmetrie zu erforschen.

Die Untersuchung des Systems Fe auf W(001) zeigt eine lagenabhängige elektronische Struktur im niedrigen Bedeckungsbereich. Die Domänenstruktur im Bereich pseudomorphes Wachstum wird erforscht und die vierzählige Anisotropie kann direkt anhand der Karten der differentiellen Leitfähigkeit abgeleitet werden. Die quantitative Auswertung zeigt eine lagenabhängige Richtung der magnetisch leichten Achse, die für die zweite und dritte Lage entlang $\langle 110 \rangle$, für die vierte Lage aber entlang $\langle 100 \rangle$ verläuft. Das Vermögen der Rastertunnelmikroskopie zwischen bis zu acht unterschiedlichen magnetischen Richtungen mit örtlicher Auflösung zu unterscheiden, demonstriert die Effizienz dieser Methode, den Magnetismus in Systemen mit reduzierten Dimensionen zu erforschen.

Contents

1	Introduction	1
2	Scanning tunneling microscopy	3
2.1	The tunnel effect	3
2.2	Experimental realisation	6
2.3	Topography: surface structure	7
2.4	Spectroscopy: electronic properties	11
2.5	Spin-polarised STM: magnetism	13
3	Instrumental setup	17
3.1	The UHV system	17
3.2	Scanning tunneling microscopes	18
3.2.1	Variable-temperature STM (VT-STM)	19
3.2.2	Low-temperature STM (cryo-STM)	19
3.3	Preparation	20
3.3.1	Sample preparation	20
3.3.2	Tip preparation	21
4	Iron on tungsten (110)	25
4.1	Structure, growth, magnetic anisotropy	26
4.2	Double-layer (DL) stripes: previous results	28
4.2.1	Magnetism and substrate miscut	28
4.2.2	Magnetic structure of wide stripes	30
4.2.3	Spin-orbit coupling	31
4.3	DL stripes: magnetism and temperature	33
4.4	DL stripes: direction of domain walls	36
4.5	Chirality	42
5	Oxygen on Fe/W(110)	45
5.1	Preparation	46
5.2	LDOS oscillations	48
5.3	Scattering theory and analysis	51
5.4	Comparison: experiment and calculation	52

5.5	Conclusion	56
5.6	Spin-resolved measurements	57
6	Iron on tungsten (001)	61
6.1	Three-dimensional growth	62
6.1.1	Compact island shape	62
6.1.2	Long island shape	63
6.2	Beginning of strain relief	64
6.2.1	Topography	65
6.2.2	Electronic structure	68
6.3	Pseudomorphic Regime	70
6.3.1	Topography	70
6.3.2	Magnetism: wetting layer and 4 th ML islands	72
6.3.3	Magnetism: 3 rd ML and 4 th ML islands	77
6.3.4	Magnetism: conclusions	79
7	Summary and Outlook	81
	Bibliography	83
	Publications	88
	Conferences	89
	Acknowledgements	91

Chapter 1

Introduction

Magnetism in reduced dimensions is a fascinating topic with a lot of barely understood phenomena [1, 2]. For the understanding of magnetic properties in general it is indispensable to study the basic properties in nanometre scale systems, where changes in structure or size have large effects on the magnetic properties. Spin-polarised scanning tunneling microscopy (STM) is a powerful tool to study magnetism down to the atomic scale. This method is magnetically sensitive and has a high spatial resolution which allows not only the investigation of magnetic properties but also the direct correlation to electronic structure measurements and topographic studies.

Magnetic thin films or islands on non-magnetic substrates are model systems to study magnetism in reduced dimensions. The investigation of the response of a system to a perturbation can also reveal information about magnetic properties. Recently scattering processes at magnetic impurities on non-magnetic surfaces have been studied intensely [3, 4, 5, 6]. Scattering states at non-magnetic adsorbates on magnetic surfaces should result in spin-polarised electron standing waves. These are of fundamental importance for the understanding of single-particle as well as many-body processes, e.g., the RKKY-interaction or the interaction between Kondo-impurities. The more classical approach of studying unperturbed thin films or islands allows the investigation of various interesting magnetic properties. A wide variety of thin film systems exhibit a thickness-dependent change in anisotropy [7, 8, 9, 10, 11, 12, 13]. Size-dependent effects have also been studied and it has been observed that different magnetic ground states are found depending on the morphology of the system [14, 15, 16].

In this thesis the correlation of topographic, electronic and magnetic properties of nanostructures is investigated by STM. After a brief introduction to the basic theoretical and practical aspects of STM (Chap. 2), a presentation of the instrumental setup and preparatory techniques is given (Chap. 3). Then experimental observations on iron (Fe) nanostructures on tungsten (W) single crystals are discussed.

First a review on previous results on the system Fe/W(110) is given with a focus on double-layer stripes. New measurements concerning the width of the stripes, the temperature dependence and the period of the magnetic structure are presented. The direction of domain walls is investigated by a variation of the orientation of the substrate miscut with respect to the crystallographic axes of the surface (Chap. 4).

The spin-resolved electronic properties of the double-layer Fe on W(110) are investigated via the analysis of scattering states. Distortion of the potential at the surface caused by adsorption of single impurities leads to an interference of incoming and reflected electron waves. The resulting standing electron waves hold information not only on the dispersion and orbital symmetry of the bands involved in the scattering process, but also on their spin character. Experimental results are compared to spin-resolved electronic structure calculations (Chap. 5).

The system of Fe on W(001) is also investigated. A survey on different growth modes is given and layer-resolved electronic structure measurements are presented. Spin-polarised measurements in the low coverage regime are the main topic. The intensities of differential conductance signals are analysed quantitatively and the layer-dependent direction of the easy axis is determined (Chap. 6).

Finally the results of the measurements presented in this thesis are summarised (Chap. 7).

Chapter 2

Scanning tunneling microscopy

The method of scanning tunneling microscopy (STM) is a powerful tool to study surfaces of conducting samples. The most obvious strength of this method is the correlation of structural, electronic and magnetic properties with high spatial and energy resolution.

This chapter summarises the general physics involved to understand the phenomenon of the tunnel process. Together with the theoretical background the experimental realisation of data acquisition and the interpretation of measurements are outlined. A more detailed treatment of these topics can be found in the literature [17]. After an introduction to tunnel theory in one dimension (Sec. 2.1) and the experimental realisation of tunnel current measurements (Sec. 2.2), the physics of constant-current imaging mode is presented, which is used to study the topography of a surface (Sec. 2.3). Aside from the investigation of the structure of surfaces, the STM is also able to measure electronic and magnetic properties of samples. This is done by the modes of scanning tunneling spectroscopy (STS) (Sec. 2.4) and spin-polarised (SP)-STM (Sec. 2.5) respectively, which are explained at the end of this chapter.

2.1 The tunnel effect

In classical mechanics a particle of energy E can overcome a potential barrier of V_0 only if $E > V_0$, otherwise it is reflected as sketched in Fig. 2.1(a). When considering very small particles like electrons they have to be treated in terms of quantum physics. Then the probability of an electron to traverse a potential barrier is non-zero even if $E < V_0$. This is sketched in Fig. 2.1(b) for an electron of energy E and mass m , and a potential barrier of height V_0 and width s . Three different regions can be distinguished:

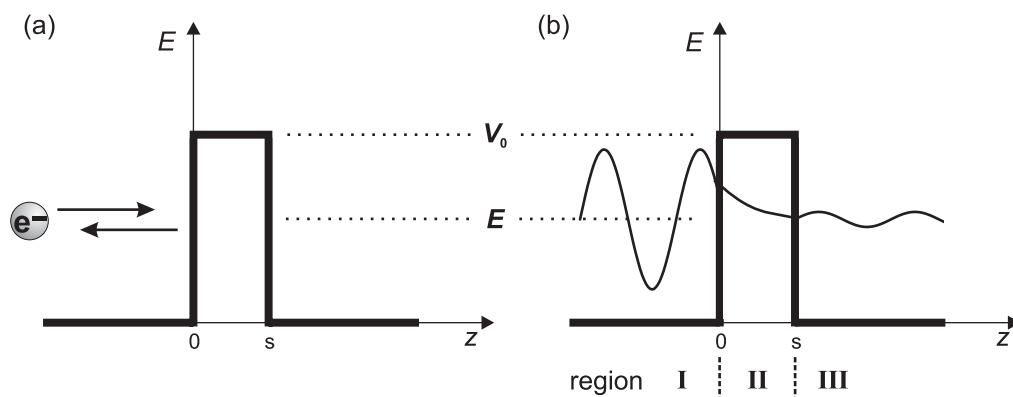


Figure 2.1: Tunnel effect in one dimension. (a) in classical mechanics an electron (e^-) of energy E is reflected by a potential barrier V_0 if $E < V_0$; (b) in quantum physics the probability of the electron wave to traverse the potential barrier is non-zero.

region I:	$z < 0$	in front of the barrier,
region II:	$0 < z < s$	inside the barrier,
region III:	$s < z$	behind the barrier.

In each region the electron can be described by the time-independent Schrödinger equation

$$\left(-\frac{\hbar^2}{2m} \frac{d^2}{dz^2} + V(z) \right) \psi(z) = E\psi(z) \quad (2.1)$$

where ψ is the electron wave function and \hbar is Planck's constant divided by 2π .

The wave functions for the different regions are:

region I:

$$\begin{aligned} -\frac{\hbar^2}{2m} \frac{d^2 \psi_1}{dz^2} &= E\psi_1 \\ \psi_1 &= e^{ikz} + A e^{-ikz} \\ k^2 &= \frac{2mE}{\hbar^2} \end{aligned} \quad (2.2)$$

region II:

$$\begin{aligned}
 -\frac{\hbar^2}{2m} \frac{d^2 \psi_2}{dz^2} + V_0 \psi_2 &= E \psi_2 \\
 \psi_2 &= B' e^{ik'z} + C' e^{-ik'z} = B e^{-\kappa z} + C e^{\kappa z} \\
 \kappa^2 &= -k'^2 = \frac{2m(V_0 - E)}{\hbar^2}
 \end{aligned} \tag{2.3}$$

region III:

$$\begin{aligned}
 -\frac{\hbar^2}{2m} \frac{d^2 \psi_3}{dz^2} &= E \psi_3 \\
 \psi_3 &= D e^{ikz} .
 \end{aligned} \tag{2.4}$$

The incident current density j_i and the transmitted current density j_t can be described by

$$j_i = \frac{\hbar k}{m} \tag{2.5}$$

$$j_t = \frac{-i\hbar}{2m} \left(\psi_3^*(z) \frac{d\psi_3(z)}{dz} - \psi_3(z) \frac{d\psi_3^*(z)}{dz} \right) = \frac{\hbar k}{m} |D|^2 \tag{2.6}$$

and the barrier transmission coefficient T is given by the transmitted current density related to the incident current density

$$T = \frac{j_t}{j_i} = |D|^2 . \tag{2.7}$$

To derive the overall wave function, the different wave functions $\psi(z)$ and their derivatives $d\psi(z)/dz$ are matched at the discontinuity points of the potential $z = 0$ and $z = s$. This results in a transmission coefficient

$$T = \frac{1}{1 + (k^2 + \kappa^2)^2 / (4k^2 \kappa^2) \sinh^2(\kappa s)} \tag{2.8}$$

and in the limit of a strongly attenuating barrier (decay constant $\kappa \gg 1$)

$$T \approx \frac{16k^2 \kappa^2}{(k^2 + \kappa^2)^2} \cdot e^{-2\kappa s} \tag{2.9}$$

$$\text{with } \kappa = \frac{\sqrt{2m(V_0 - E)}}{\hbar} . \tag{2.10}$$

This theoretical treatment of the tunnel effect in one dimension is called the 'wave matching method'. It explains the phenomenon of electron tunneling well, but application to realistic STM experiments in three dimensions is extremely difficult.

2.2 Experimental realisation

To investigate sample properties by measuring tunnel currents various requirements have to be met. The sample must be conductive in order to allow a tunnel current flow between the sample and a conducting counter-electrode, in the case of STM this is a sharp probe tip. The width of the insulating tunnel barrier has to be on the order of a few Ångstrom (\AA) to obtain measurable tunnel currents. In STM measurements typical tunnel currents I are in the regime of $I = 0.1 - 1 \text{ nA}$. The approach between the two electrodes has to be extremely well controlled in order to avoid mechanical contact. For this reason the experimental setup has to be very rigid and a lot of care has to be taken to reduce mechanical instabilities. The movement of one electrode with respect to the other is realised by mounting one electrode on a piezoelectric device. Figure 2.2(a) shows the sketch of a tip mounted on a tube scanner, which is the most compact device for this application. When applying a voltage U_z to the z -electrode inside the scanner the piezoelectric material, and thus the whole tube, elongates or contracts depending on the polarity. In this way the fine adjustment of the distance between tip and sample is achieved. With a coarse positioning device made out of piezoelectric material as well, the whole scanner including the tip can be moved stepwise by making use of friction in a slip-stick mode. Figure 2.2(b-d) shows the scanner mounted on a slide and connected to the body of the microscope via piezoelectric stacks and ruby balls. In (b) the piezoelectric stacks are in the resting position. When applying a rapid voltage pulse to them they shear, and due to the inertia of the slide its position is unchanged as shown in (c). When ramping the voltage

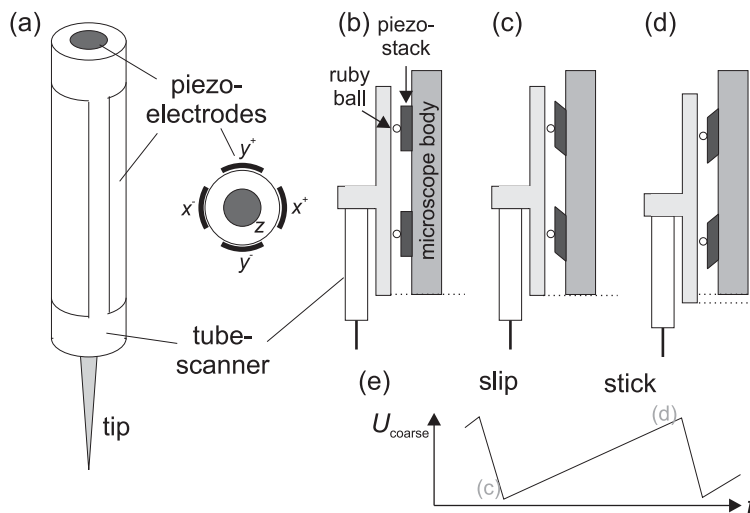


Figure 2.2: Approach mechanism. (a) tube scanner with tip; coarse positioning device in (b) resting and (c,d) extreme positions; (e) sawtooth voltage for the slip-stick mode.

U_{coarse} to the original value more slowly, the slide follows the shear motion of the piezoelectric stacks due to friction (d). After this movement of the tip towards the sample the tube scanner is elongated to its maximum length while trying to detect a tunnel current. If no tunnel current is detected the tip is retracted again. This cycle of slipping, sticking and elongating the scanner is repeated automatically until tunnel contact is reached and the approach is finished. The sawtooth voltage U_{coarse} applied to the coarse positioning device is sketched in Fig. 2.2(e). To investigate the sample surface with lateral resolution the tube scanner cannot only be moved normal to the surface (z -direction) but it can also be bent. This is done by applying appropriate voltages U_x, U_y to the electrodes on the sides of the tube scanner (x, y -electrodes in Fig. 2.2(a)) which allows a precise lateral positioning of the tip with respect to the sample surface.

2.3 Topography: surface structure

The interpretation of scanning tunneling microscopy (STM) measurements is based on an approach different from the wave matching method (see Sec. 2.1). To describe a tunnel current Bardeen used first-order time-dependent perturbation theory [18]. Instead of calculating the Schrödinger equation of the coupled system this approach derives the tunnel current from the overlap of the wave functions of the two electrodes. Tersoff and Hamann were the first to apply Bardeen's transfer Hamiltonian to tunnel experiments with a STM [19]. They approximated a locally spherical symmetry for the tip and allowed only s -type wave functions to contribute to the tunnel matrix element. In the limit of low temperature T and small applied bias voltage U between tip and sample, the tunnel current I can be described by

$$I \propto U \cdot \rho_t(E_F) \cdot e^{2\kappa R} \cdot \underbrace{\sum_s |\psi_s(r_0)|^2 \cdot \delta(E_s - E_F)}_{\rho_s(E_F, r_0)} \quad (2.11)$$

$$\text{with } \kappa = \frac{\sqrt{2m\phi_{\text{eff}}}}{\hbar}$$

where ρ_t is the density of states of the tip, E_F is the Fermi energy and r_0 and R are properties of the tip related to the geometry as sketched in Fig. 2.3. The decay constant κ depends on the effective local potential barrier height ϕ_{eff} , which is in good approximation equal to the average of the tip and sample surface work functions ϕ_t and ϕ_s . The last term of Eq. 2.11 sums the sample wave functions ψ of discrete electronic states E_s . The expression can be described as the surface density of states ρ_s at the Fermi energy.

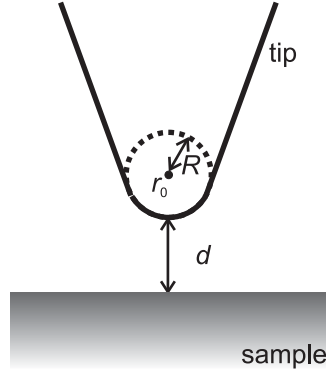


Figure 2.3: Geometry of the STM tip in the Tersoff-Hamann model: r_0 is the centre of the curvature of the spherical tip apex with radius R , d is the distance from the foremost end of the tip to the sample surface.

Since the wave functions decay exponentially into the vacuum one can derive that the tunnel current depends exponentially on the distance d between the tip and the sample (see Fig. 2.3):

$$I \propto e^{-2\kappa d} . \quad (2.12)$$

In the small bias voltage limit the tunnel current may be interpreted as proportional to the sample density of states. At larger bias voltage the tunnel current represents a weighted integral over a range of energies

$$I \propto \int_0^{eU} \rho_s(E) \cdot \rho_t(E, eU) \cdot T(E, eU) dE \quad (2.13)$$

with a transmission factor

$$T(E, eU) = \exp \left[-d \cdot \sqrt{\frac{4m}{\hbar^2} (\phi_t + \phi_s + eU - 2E)} \right] . \quad (2.14)$$

Figure 2.4 shows the system of tip and sample in tunnel contact in equilibrium and with applied sample bias voltage. The occupied states are indicated by the shaded region below the Fermi energy, the sample density of states is sketched by the curve inside the tunnel barrier. The difference between the Fermi energy E_F and the vacuum level E_v is the work function ϕ (index t for tip and s for sample). In the equilibrium state in Fig. 2.4(a) the net tunnel current is zero. At negative sample bias voltage U electrons from the sample in the energy interval from $E_F - eU$ to E_F can tunnel into unoccupied states of the tip (b). For positive U the situation is reversed and electrons from occupied tip states tunnel into unoccupied states of the sample (c).

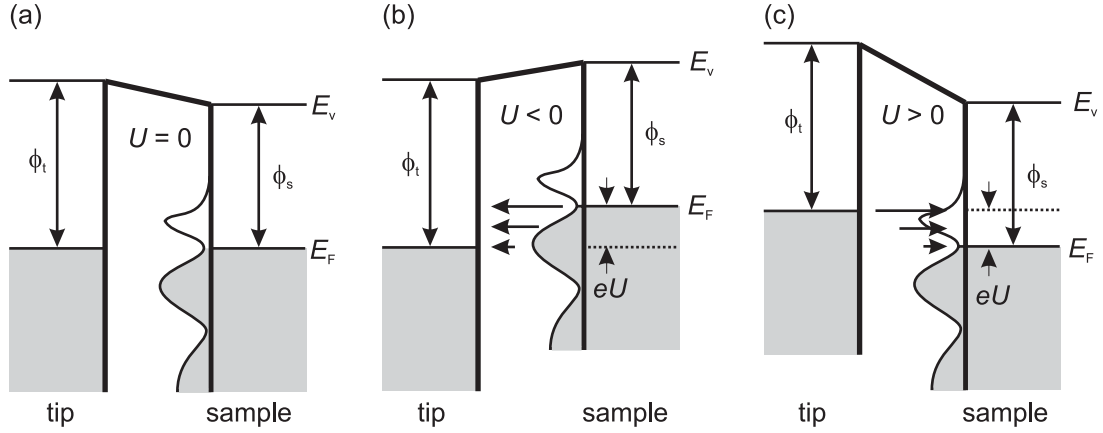


Figure 2.4: System of tip and sample in tunnel contact. (a) equilibrium, no net tunnel current; (b) negative sample bias, net tunnel current from sample to tip; (c) positive sample bias, net tunnel current from tip to sample. Note the energy-dependent sample density of states sketched by the curve inside the barrier.

To experimentally investigate the surface structure, or topography, of a sample one takes advantage of the exponential dependence of the tunnel current I on the distance d between tip and sample (see Eq. 2.12). A difference in tip height z of about 1 \AA typically leads to a variation in the tunnel current I on the order of one magnitude, which is also the reason for the high vertical resolution of the STM. When scanning the sample surface with the tip there are two different modes of operation, the constant-height and the constant-current mode which are sketched in Fig. 2.5. In constant-height mode (a) the vertical position z of the tip is held constant while scanning and the resulting tunnel current between tip and sample is measured. Since d_1 is larger than d_2 in this example the tunnel current I_1 is smaller than I_2 at a given sample voltage U . In constant-current mode (b) a feedback loop provides a constant tunnel current between tip and sample at every position (x, y) . This means that the z -position of the tip has to be adjusted during scanning which is done by applying an appropriate voltage U_z to the z -piezo of the tube scanner. One distinguishes between these two extreme modes of operation even though neither of them can be realised experimentally and one can only approximate one or the other by choosing the appropriate parameters for the feedback loop gain and the scan speed.

In this work topographic images were acquired under conditions close to constant-current mode. For small U this means that the topographic image of a sample corresponds, as a first approximation, to a contour map of constant surface local density of states at E_F (see Eq. 2.11). For larger bias voltage the dependence of the tunnel current on the electronic structure of the sample has to be taken into account (see Eq. 2.13) to avoid incorrect interpretations of STM images.

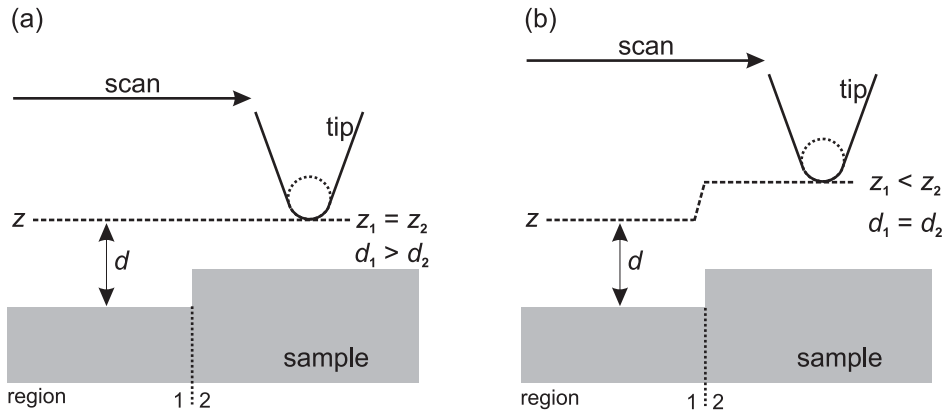


Figure 2.5: Modes of STM operation. (a) constant-height mode, measurement of the tunnel current; (b) constant-current mode, measurement of the height z of the tip.

To demonstrate the difficulties of STM image interpretation the sketch in Fig. 2.6 shows a sample with a plane surface but areas with different local density of states ρ_s or work function ϕ_s . In region 1 with the density of states ρ_{s1} or the work function ϕ_{s1} the tunnel current is I_1 at a tip sample distance d_1 . To keep the tunnel current constant when scanning ($I_2 = I_1$), the tip has to be moved closer to the sample surface in region 2 ($d_2 < d_1$) due to the reduced density of states ρ_{s2} or work function ϕ_{s2} in that surface area. This means that in constant-current mode the resulting topography image $z(x, y)$ shows a depression for region 2 in comparison to region 1 even though the sample surface is flat. In the following this phenomenon is referred to as the 'topographic effect'.

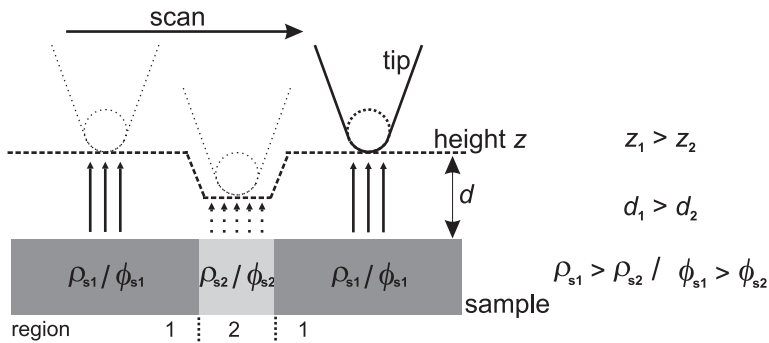


Figure 2.6: Sketch of the 'topographic effect': sample areas with different local density of states ρ_s or work function ϕ_s can lead to a variation in tip height z when operating in constant-current mode even though the surface is flat (the number and strength of the arrows illustrate the tunnel current density).

The data of topographic measurements can be corrected if the work function ϕ_s in the different sample areas is known. The square root of the work function is proportional to the decay constant κ (see Eq. 2.11). Recalling Eq. 2.12 a method to obtain κ experimentally is obvious. When measuring the dependence of the tunnel current I with the distance d between tip and sample, i.e. of height z of the tip with respect to the sample, one derives the decay constant κ from the slope of a logarithmic graph $\ln I(z)$:

$$\ln I \propto -2\kappa z . \quad (2.15)$$

Now a normalised tunnel current I_{norm} , simulating a constant-height measurement, can be calculated using the experimentally observed current I_{exp} and the measured height z :

$$I_{\text{norm}} = I_{\text{exp}} \cdot e^{2\kappa z} . \quad (2.16)$$

Considerations about the topographic effect are mentioned and discussed in this thesis where appropriate. In all other cases it can be neglected.

2.4 Spectroscopy: electronic properties

To gain information about the electronic properties of a sample the differential conductance dI/dU can be analysed. Differentiation of Eq. 2.13 with the approximation that ρ_t is constant results in

$$\frac{dI}{dU} \propto \rho_t(0) \cdot \rho_s(eU) \cdot T(E, eU) + \int_0^{eU} \rho_s(E) \cdot \rho_t(eU - E) \cdot \frac{dT(E, eU)}{dU} dE \quad (2.17)$$

The second term can often be neglected and then, under the assumption of a monotonic variation of T with U the differential conductance dI/dU is a good measure of the energy-dependent density of states of the sample ρ_s [20].

Experimentally this is realised by positioning the tip above the surface with the stabilisation parameters I and U . Then the feedback loop is switched off and the voltage is ramped from the initial voltage to a final voltage. Meanwhile the tunnel current is acquired with the z -position of the tip held constant. The resulting $I(U)$ curve holds information on the electronic properties of the sample. A more comprehensive measure is the differential conductance dI/dU . As a first approximation one obtains (cf. Eq. 2.17)

$$\frac{dI}{dU} \propto \rho_t(0) \cdot \rho_s(eU) \cdot T(E, eU) . \quad (2.18)$$

The differential conductance reflects the density of states of the sample ρ_s . The energy-dependent differential conductance can be obtained by either differentiating $I(U)$ curves numerically or by means of a lock-in technique.

All dI/dU signals shown in this thesis were recorded using a lock-in technique with a modulation voltage $U_{\text{mod}} = 10 - 20$ mV added to the bias voltage. The frequency f of the modulation voltage was $f = 3 - 8$ kHz for the low-temperature STM and $f \approx 0.8$ kHz for the variable-temperature STM (see Chap. 3.2 for details on the microscopes). Figure 2.7 shows the system of tip and sample in tunnel contact (see also Fig. 2.4). Three examples out of a voltage sweep are presented. Figure 2.7(a) shows the dI/dU signal detected at the positive sample bias U_1 . Electrons from the Fermi energy of the tip probe the local density of states of the sample at $E_F + eU_1$. Since the sample density of states shows a peak at $E_F + eU_2$ the dI/dU signal at that voltage U_2 is larger compared to the one at U_1 (b). When reaching negative sample bias voltage electrons from E_F of the sample probe unoccupied states of the tip (c). This illustrates that at positive U the unoccupied states of the sample are probed while at negative U the dI/dU signal is dominated by the density of states of the sample at E_F [17].

Investigation of the electronic structure of a sample with lateral resolution can be done by performing full dI/dU spectroscopy at different positions of the sample. Ideally this is done at every measurement point of one image area to obtain a three-dimensional parameter space of x, y -position and energy-dependent dI/dU signal. This allows a direct correlation of topographic $z(x, y)$ and spectroscopic properties $dI/dU(x, y, U)$ of the sample.

If the interest is focused on one particular energy only a very time-saving alternative to full dI/dU spectroscopy is the acquisition of dI/dU maps. While dI/dU spectra are acquired with an open feedback loop at the given stabilisation

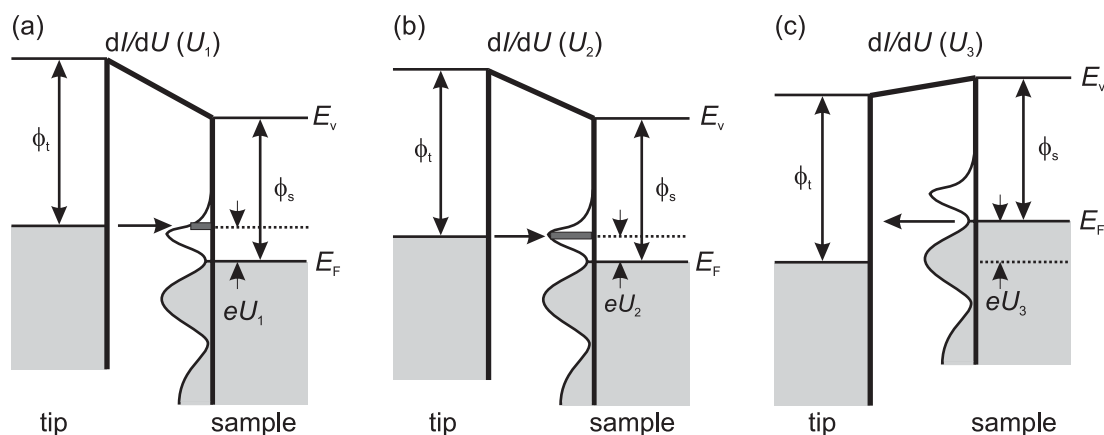


Figure 2.7: System of tip and sample in tunnel contact: measurement of the dI/dU signal. (a) the dI/dU signal at U_1 corresponds to the density of states of the sample at $E_F + eU_1$; (b) large dI/dU signal at the peak position $\rho_s(E_F + eU_2)$; (c) at negative sample bias $\rho_s(E_F)$ dominates the dI/dU signal.

parameters, for the measurement of dI/dU maps the feedback loop is not switched off at any time but simultaneously to the topographic measurement a lock-in technique derives the dI/dU signal at the corresponding voltage. Due to the reduction of measurement parameters, i.e. no energy resolution, the spatial resolution can be enhanced to perform measurements in even shorter time without the loss of correlation between topography $z(x, y)$ and differential conductance $dI/dU(x, y)$.

Great care has to be taken when analysing the data obtained in dI/dU measurements. The stabilisation parameters for full spectroscopy as well as for maps can have an impact on the measured dI/dU data. Especially when comparing spectra taken on areas with different electronic structure or work function one has to bear in mind that the topographic effect can have an influence on the measurement which may lead to incorrect interpretations (see Sec. 2.3). To compare dI/dU data quantitatively a normalisation of the experimental data may be necessary to account for a variation in the distance between tip and sample (cf. Eq. 2.16):

$$\left(\frac{dI}{dU}\right)_{\text{norm}} = \left(\frac{dI}{dU}\right)_{\text{exp}} \cdot e^{2\kappa z}. \quad (2.19)$$

Again this is discussed in connection with the measurements of this thesis where necessary.

2.5 Spin-polarised STM: magnetism

This section deals with the dependence of the tunnel current on the spin of the electrons involved. To be sensitive to the spin imbalance of the tunneling electrons of one electrode, the other electrode has to be spin-polarised as well. A theoretical treatment of electron tunneling between two spin-polarised electrodes has been done by Slonczewski [21]. In the limit of a vanishing bias voltage U and under the assumption of a free-electron behaviour of the conduction electrons, the spin-polarised tunnel current I_{SP} between two spin-polarised electrodes can be described by

$$I_{\text{SP}}(U_0) = I_0[1 + P_s \cdot P_t \cdot \cos(\vec{M}_s, \vec{M}_t)] \quad (2.20)$$

where I_0 is the non-spin-polarised current. P is the spin polarisation, \vec{M} the magnetisation, and the indices stand for sample (s) and tip (t). Since I_0 , P_s , P_t and \vec{M}_t are constant at a given voltage U_0 for an electronically uniform sample region, a variation in I_{SP} and therefore also dI_{SP}/dU can be attributed to different directions of the sample magnetisation \vec{M}_s with respect to \vec{M}_t . When the direction of the magnetic moment of the tip is unknown, SP-STM measurements only hold information about variations of the sample magnetisation with respect to the tip magnetisation but are unable to determine the absolute direction of magnetisation.

Figure 2.8(a) demonstrates the angular dependence of I_{SP} for two spin-polarised electrodes. Considering the two extreme cases of parallel (b) and antiparallel (c) alignment of the magnetic moments of the two electrodes one derives:

$$\begin{aligned} I_{\text{SP}}(U_0) &= I_0(1 + P_s \cdot P_t) \quad \text{for } \alpha = 0^\circ \quad \text{parallel } (\uparrow\uparrow) \\ I_{\text{SP}}(U_0) &= I_0(1 - P_s \cdot P_t) \quad \text{for } \alpha = 180^\circ \quad \text{antiparallel } (\uparrow\downarrow). \end{aligned} \quad (2.21)$$

The effective polarisation for the whole tunnel junction is defined as

$$P = P_s \cdot P_t = \frac{I_{\uparrow\uparrow} - I_{\uparrow\downarrow}}{I_{\uparrow\uparrow} + I_{\uparrow\downarrow}}. \quad (2.22)$$

$I_{\uparrow\uparrow}$ and $I_{\uparrow\downarrow}$ are the tunnel currents for parallel and antiparallel alignment of tip and sample magnetisation, respectively.

The most important characteristic of electron tunneling between spin-polarised electrodes is the spin conservation. Bearing this in mind the simple sketch in Fig. 2.9 clarifies the basic principle of spin-polarised tunneling on the basis of a spin-split density of states. Considering an electron with spin \downarrow in an occupied tip state and a positive sample voltage U this electron can tunnel into an empty sample state with spin \downarrow only as indicated by the arrow in Fig. 2.9(a). The sketch in (b) shows a reversed sample spin polarisation and it is obvious that in this configuration there are less unoccupied sample states with spin \downarrow available close to the Fermi energy. Since the tunnel probability depends on the number of electronic states available for the tunnel process the spin-polarised tunnel current will

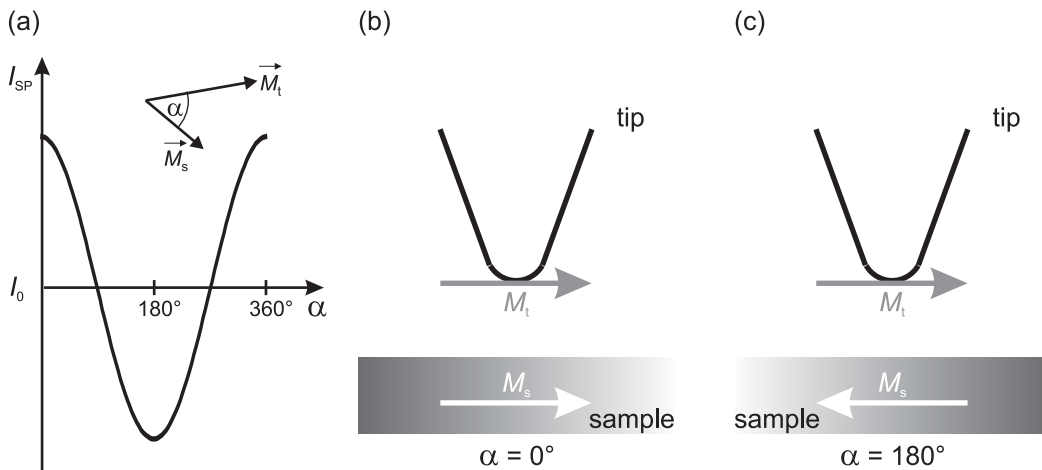


Figure 2.8: Spin-polarised tunneling. (a) angular dependence of the spin-polarised current I_{SP} ; sketch of a (b) parallel and (c) antiparallel alignment of the spin-polarised electrodes.

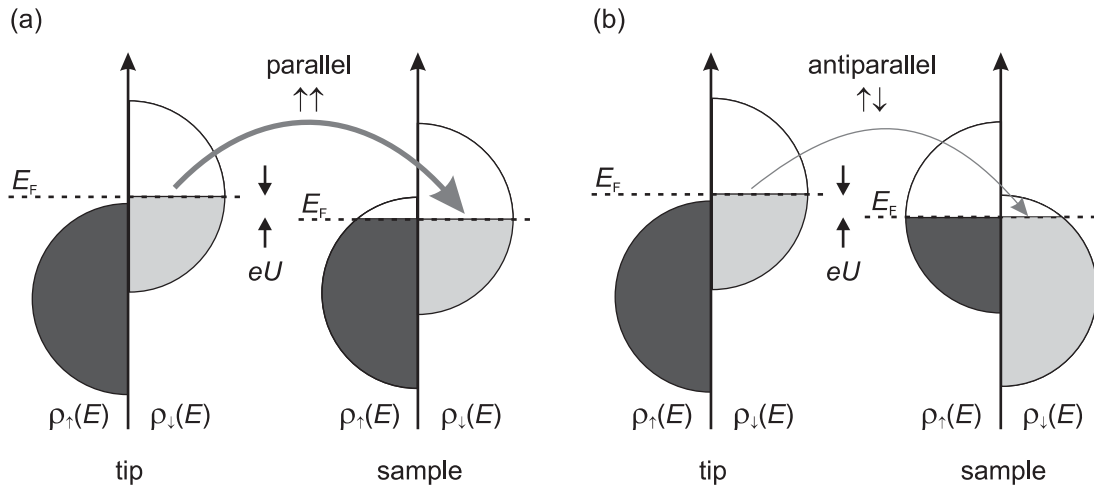


Figure 2.9: Spin-polarised tunneling with spin conservation at positive sample bias. (a) electrons from the tip with spin \downarrow can tunnel into unoccupied states of the sample with spin \downarrow , due to a large number of states the tunnel probability is high; (b) reversed sample spin polarisation with less unoccupied states \downarrow , therefore the tunnel probability is smaller.

be larger in the example of Fig 2.9(a) than in (b). The need for careful interpretation of data as mentioned already in Sec. 2.3 and 2.4 of course also holds for the magnetic measurements of this thesis. In addition to the previously mentioned parameters, a topographic effect may also result from measurements on different magnetic domains, which differ in their spin-resolved density of states [22].

Chapter 3

Instrumental setup

Scanning tunneling microscopy (STM) measurements of nanostructures on single crystals aim at the investigation of fundamental questions concerning structural, electronic and magnetic properties. It has to be guaranteed that well-defined samples can be prepared reproducibly. For this reason experiments are performed in ultra high vacuum (UHV) which allows preparation of clean samples and reduces subsequent contamination.

In this chapter the instrumental setup of the UHV system is described (Sec. 3.1) followed by an introduction to the scanning tunneling microscopes used for the measurements presented in this thesis (Sec. 3.2). Finally the experimental procedure to prepare samples and tips is commented on (Sec. 3.3).

3.1 The UHV system

The experiments were performed in an ultra high vacuum (UHV) system which is shown in Fig. 3.1. It consists of four different satellite chambers connected via a distribution chamber. The base pressure in all of them is in the low 10^{-9} Pa regime. A fast-entry lock is attached to introduce samples and tips into the system without breaking the vacuum. Suitable holders allow the transfer of samples and tips between the different satellite chambers. They can be inserted into x, y, z -manipulators and thus be precisely positioned in each chamber. Furthermore there are heating facilities in the manipulators of three satellite chambers. For substrate preparation one chamber (see Fig. 3.1) is equipped with an ion sputter gun and an electron beam heater. Preparation of thin films on single crystal surfaces is done by molecular beam epitaxy (MBE) in the assigned chamber (see Fig. 3.1). The use of different chambers for substrate preparation and metal evaporation is crucial to ensure good UHV conditions during MBE. A metal rod, or a crucible filled with the material to be evaporated, is heated by electron bombardment. The evaporation rate can be adjusted by choosing appropriate parameters and simultaneous

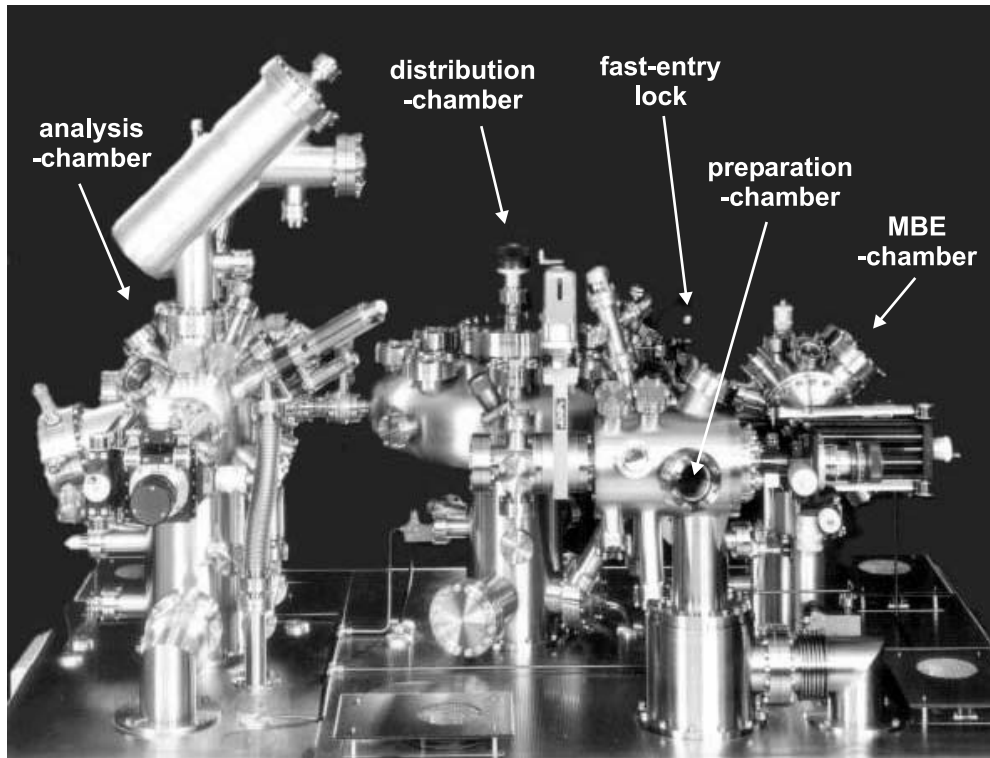


Figure 3.1: Photography of the UHV system (prior to the extension with the cryo-STM, which is attached to the distribution chamber next to the fast-entry lock).

or subsequent heating of the sample influences the growth of the material on the substrate. The analysis-chamber (see Fig. 3.1) holds standard surface characterisation methods to gain insight into surface properties of samples. The periodicity of a surface and an estimate of the quality of its structure can be determined by low energy electron diffraction (LEED). Auger electron spectroscopy (AES) is an element specific method and allows a quantitative measure of the components at the surface. Furthermore there are three different types of STMs in the UHV system. A room-temperature STM is installed in the MBE-chamber, the analysis chamber holds a variable-temperature STM while a low-temperature STM is in a separate chamber not shown in Fig. 3.1. The two latter STMs are used in this work and introduced in detail in Sec. 3.2.

3.2 Scanning tunneling microscopes

The direct investigation of the sample surfaces was done by scanning tunneling microscopy (STM). It allows the characterisation not only of the topography of a surface, but also of electronic as well as magnetic properties (see Chap. 2).

Measurements in this thesis were performed either with the commercially available variable-temperature STM or a home-built low-temperature STM. Individual strengths and weaknesses arise from their design characteristics which are described in the following.

3.2.1 Variable-temperature STM (VT-STM)

The VT-STM is available commercially from Omicron NanoTechnology GmbH. The tip is always at ambient temperature, and the temperature T of the sample can be varied. It is decreased by pumping liquid helium (He) through a continuous-flow cryostat while an integrated heating device allows an opposing increase in temperature. The temperature is controlled by shifting the equilibrium between cooling and heating which allows a convenient variation between $T = 50$ K up to room temperature $T_{\text{RT}} = 300$ K. The samples are introduced into the STM with a wobble stick, and a screw is used to clamp the sample holder to the body of the STM to ensure good thermal contact. The sample temperature can be adjusted with an absolute accuracy of ± 10 K and a relative accuracy of ± 2 K. After insertion of the sample into the STM the temperature reaches equilibrium within one hour. A x, y -sample stage allows access to different surface areas of a sample. The STM tip is mounted on a tip holder which has a baseplate made out of magnetic steel. For measurements it is placed on the front end of the tube scanner where it is fixed due to magnetic interaction. The tip can be exchanged within a few minutes.

3.2.2 Low-temperature STM (cryo-STM)

The cryo-STM is a home-designed and -built scanning tunneling microscope [23]. It is in thermal contact with a bath cryostat filled with liquid helium (He). A tank of liquid nitrogen (N_2) shields the bath cryostat and the STM from the radiation of the surrounding. The sample is positioned in the STM with a wobble stick and held in place by leaf springs which are also responsible for the thermal contact. During measurements tip and sample are held at $T = 13$ K which is reached within about one hour after the sample is inserted into the STM. The tip is mounted on a pin made out of molybdenum (Mo) which is held by a leaf spring at the end of the tube scanner. The tip exchange can be performed within a few minutes. With a superconducting split-coil magnet a magnetic field perpendicular to the sample surface of up to $B = 2.5$ T can be applied. The cryo-STM is characterised by a much higher thermal as well as mechanical stability in comparison to the VT-STM.

3.3 Preparation

In this thesis the results of investigations on iron (Fe) nanostructures on tungsten (W) single crystals with surface orientation (110) and (001) are presented. Measurements were performed with non-magnetic tips for spin-integrated measurements as well as magnetic tips for spin-polarised measurements. In this section a detailed report on sample preparation procedures is given followed by a description of the tip preparation for the two different STMs used. Finally, guidance is given on how to achieve the desired magnetic sensitivity of a tip for a given experimental problem.

3.3.1 Sample preparation

The tungsten single crystals were cleaned in a two-step process. First the crystal was annealed ($T_{W(110)} = 1500$ K, $T_{W(001)} = 1700$ K) in oxygen atmosphere (oxygen partial pressure $p_{O_2} \approx 5 \cdot 10^{-5}$ Pa) for twenty minutes. At these temperatures the carbon dissolved in the bulk crystal segregates to the surface and is oxidised. The product desorbs thermally from the surface. In a second step the tungsten oxide formed at the surface was removed by a short flash of the crystal to high temperature ($T_{W(110)} \geq 2200$ K, $T_{W(001)} \geq 2500$ K). These steps were repeated until the substrate was sufficiently clean [24, 25]. Figure 3.2(a) shows an overview of the topography of an as-prepared W(110) single crystal surface. The remaining adsorbates on the surface can be recognised in the closer view (b). With a contamination of about 0.1 ± 0.01 adsorbates per nm^2 (0.7% of the surface atoms)

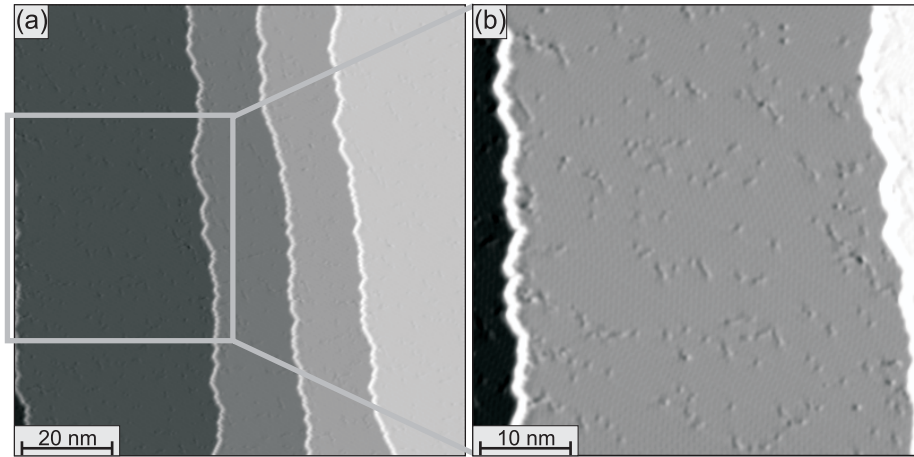


Figure 3.2: Topography of a W(110) surface after preparation. Measurement parameters: (a) $U = +1.0$ V, $I = 0.25$ nA; (b) $U = +1.0$ V, $I = 0.1$ nA, closer view of the image area indicated in (a), adsorbate density is 0.1 ± 0.01 adsorbates per nm^2 or 0.7% of the surface atoms.

this surface was adequately clean. In the following only a short flash of the crystal was needed to prepare the W-surface until it was contaminated again due to the segregation of carbon from the bulk to the surface at elevated temperature.

Fe was evaporated from a rod heated by electron bombardment. Typical evaporation rates were in the range of approximately 0.5 monolayers (ML) per minute at a pressure $p \leq 10^{-8}$ Pa. The coverage θ is always given in pseudomorphic monolayers referring to the specific substrate. In the context of spatially resolved measurements θ refers to the local coverage. The growth mode of Fe on the surface can be influenced by simultaneous or subsequent annealing of the substrate (for details see Chap. 4 for Fe/W(110) and Chap. 6 for Fe/W(001)). The temperature was measured with a thermocouple attached to the manipulator close to the sample.

To investigate single oxygen (O) adsorbates (see Chap. 5) gaseous oxygen (O_2) was introduced into the chamber through a valve leak. The adjusted oxygen partial pressure p_{O_2} and the time the surface is exposed together with the affinity of the surface to the gas determines the mode and degree of adsorption. One differentiates between physisorption for weak interaction due to van-der-Waals forces and chemisorption for stronger interaction (> 50 kJ/mol or 0.5 eV/atom) with partial charge transfer between adsorbate and surface [26]. A dose of one Langmuir (L) is defined as a gas pressure of $p = 1 \cdot 10^{-6}$ Torr for the time $t = 1$ s.

3.3.2 Tip preparation

General procedure

To achieve distinct structures in STM measurements the preparation of sharp and stable tips is crucial. Tips used in this work were made out of poly-crystalline W wire (diameter $D = 0.38$ mm for the VT-STM and $D = 0.75$ mm for the cryo-STM) which was etched electrochemically in sodium hydroxide solution (2M NaOH). After fixing the tip in the holder it was inserted into the vacuum chamber. The oxide film covering the tungsten tip was removed by a short flash to $T \geq 2000$ K. Since the cryo-STM has been designed for this tip preparation procedure, appropriate materials (tungsten, molybdenum, tantalum) for holders and transport facilities are used. The removal of the oxide film or other contaminants from the tip is very simple in this case and was done by flashing the tip together with the holder and transporter by electron bombardment. In contrast, the tip holders of the VT-STM are manufactured from magnetic steel which is not suitable for high temperatures. Therefore a much more complicated procedure has to be performed in order to remove the oxide layer from the tungsten tips intended for the use in the VT-STM. A thin thorium oxide covered tungsten wire ($D = 0.25$ mm) was coiled to form a spiral which was positioned around the

front part of the tip. When heating the spiral resistively, electrons are emitted which are accelerated towards the tip by applying a high voltage. In this way high temperatures at the front end of the tip were reached while the tip holder stayed at a much lower temperature and retained its magnetic properties. The as-prepared tungsten tips were used for spin-integrated measurements.

If the imaging conditions are instable or if a multiple tip is detected a supplementary sharpening of tips can be done *in-situ* while measuring. By applying a voltage pulse between tip and sample a rearrangement at the front end of the tip on the atomic scale or a loss or gain of material is probable. Furthermore the properties of the tip can be changed by mechanical contact with the sample surface. Of course this is not a controlled way to tailor the shape of the tip but one has to continue to modify the tip until sufficient imaging conditions are achieved. Alternatively one has to induce a change at the front end of the tip by a flash to high temperature as described before, or eventually replace the tip with a new one.

Spin-polarised tips

In order to investigate magnetic properties of a surface with scanning tunneling microscopy a spin-polarised tip is required (see Chap. 2.5) and there are different approaches to realise this [27]. In this work the clean tungsten tips were coated with magnetic thin films and the choice of the material and its thickness determines the magnetic sensitivity of the tip. The temperature of the tip during measurement also plays an important role because of reorientation transitions and the Curie- or Néel-temperature of the magnetic thin film.

The tip of the cryo-STM is held at $T = 13$ K during measurements. The magnetic sensitivity of tips covered with different magnetic materials under these conditions is shown in Fig. 3.3. Thin Fe films covering the W tip are ferromagnetic at this temperature and are sensitive to a sample magnetisation parallel to the surface plane (a) [27, 28]. Best results were achieved after deposition of an amount of Fe equivalent to a coverage of $\theta = 8$ ML and subsequent moderate annealing ($T \approx 500$ K). When co-evaporating Gadolinium (Gd) and Fe with a ratio of 15 : 1 and moderate annealing ($T \approx 500$ K) the magnetic configuration of the tip allows an investigation of the component of the sample magnetisation perpendicular to the surface (b). Antiferromagnetic Chromium (Cr) thin films on W tips also provide magnetic sensitivity [29]. This results from the dominating contribution to the tunnel current of the outermost atom, which magnetic orientation is of course also fixed in an antiferromagnet as illustrated in Fig. 3.3(c). For Cr-coated W tips the magnetic sensitivity is normal to the sample surface plane at low coverage ($\theta = 25-45$ ML) and changes to parallel for higher coverage ($\theta > 45$ ML).

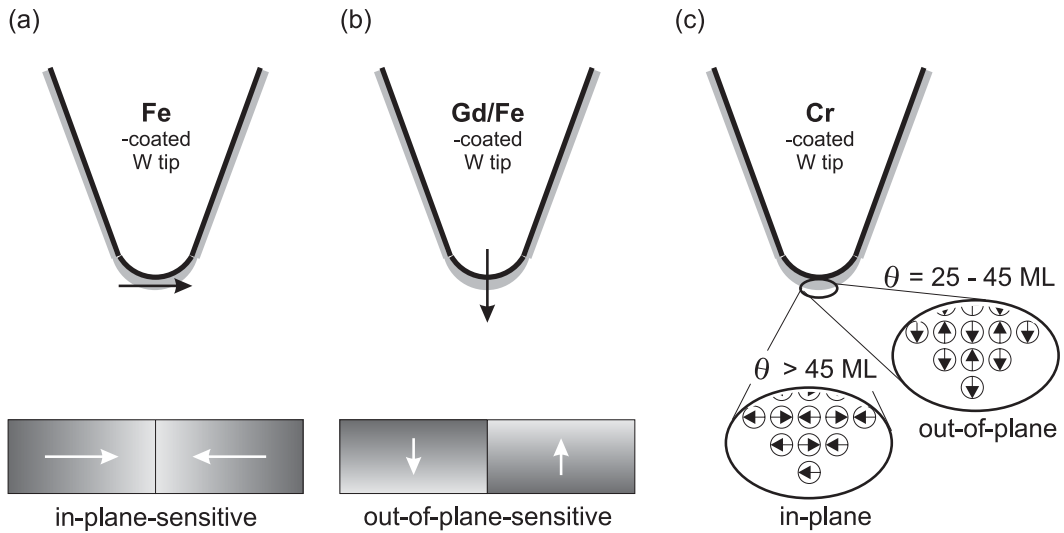


Figure 3.3: Magnetic sensitivity of W tips coated with different magnetic material. (a) Fe-coated tips are sensitive to the in-plane component of surface magnetisation; (b) Gd/Fe-coated tips are useful for the investigation of samples with an out-of-plane magnetisation; (c) Cr-coated tips show a thickness-dependent reorientation from in-plane magnetisation to out-of-plane magnetisation.

As a consequence of the tip being at room temperature during measurements with the VT-STM, more material is necessary to ensure ferro- or antiferromagnetism at the outermost tip atom. Even though ferromagnetism has been reported for a double-layer of iron above room temperature [30], with the VT-STM a much higher coverage of Fe ($\theta = 15 - 50$ ML) with subsequent annealing of the tips was necessary to obtain a magnetic sensitivity for the in-plane component of the sample. Preparation of a tip with a magnetic sensitivity to the component perpendicular to the sample surface plane with Gd and Fe has not been successful. Since the Néel-temperature of chromium is just above room temperature ($T_N(\text{Cr}) = 311$ K) the preparation of thin Cr films on W tips for magnetic measurements with the VT-STM has not been attempted.

Another possibility to get magnetic material to the front end of the tip to achieve magnetic sensitivity is the use of voltage pulses between tip and a magnetic material [31]. The most convenient way is to pulse on the magnetic sample to be investigated and afterwards move the tip to an unaffected sample area for measurements. For W tips and a sample of Fe on W suitable parameters were sample voltages of $U = -1$ V and tunnel currents I greater than 1 nA. However, the mechanism of material exchange is not reproducible and the configuration of the atoms at the end of the tip and their magnetic properties are unknown. This technique can be used when the magnetic properties of the sample are sufficiently known so that measurements can be interpreted unambiguously.

In general one can summarise that any spin-polarised material can be used as a thin film coating to produce magnetically sensitive tips. For ferromagnetic materials a balance has to be found between thin films which tend to be magnetically unstable with increasing temperature, and thicker films which have a large stray field which can influence the magnetic structure of the sample. A solution to overcome the problems with tip stray fields is the use of antiferromagnetic materials for tips. Thin film coating has been done with Cr, but signal strengths are not as large as with the ferromagnetic coatings described above. Also a higher degree of contamination of the antiferromagnetic elements Cr and Manganese (Mn) is a drawback for deposition of thin films. In principle bulk materials can be used as tips as well but the brittleness of antiferromagnetic elements and composites is the reason that wires are not available.

Chapter 4

Iron on tungsten (110)

In the past the system of Fe on W(110) has been studied intensely and a great number of measurements with various techniques have been reported. In the low coverage regime extremely interesting and multi-faceted structural, electronic and magnetic properties have been observed. Double-layer (DL) stripes of Fe on W(110) have been investigated with spin-integrated as well as spin-polarised scanning tunneling microscopy (STM) and together with first-principle calculations this has led to a comprehensive understanding of various properties of this system [14, 29, 32, 33, 34, 35, 36]. But still a lot of open questions remain, since these STM measurements on the double-layer have been performed at low temperature and on substrates with a large miscut. To gain further insight into the magnetic properties of this system, the investigation of the response of the system to the variation of these parameters is useful. The stability of a magnetic structure is connected to the temperature of the system while the structure itself depends strongly on the crystallographic anisotropy and on the dimensions, i.e. for stripes on the direction and size of the substrate miscut.

This chapter is assigned to the system of Fe on W(110). Due to the large amount of literature, the overview given in this chapter is mainly restricted to reports which are in direct relation to the new results presented here. First a short survey on the system concerning structure, growth and magnetic anisotropy is given (Sec. 4.1). Then a more detailed summary of previous results on DL stripes of Fe on W(110) is presented (Sec. 4.2). The influence of the surface miscut, and hence the width of the stripes, on the magnetic coupling mechanism is discussed. The formerly observed transition from antiferromagnetic coupling between narrow stripes to the formation of domain walls in wider stripes with ferromagnetic coupling between them is recalled. In this thesis DL stripes with a width much larger than half of the magnetic period are investigated and the magnetic structure is found to be unchanged in the [001] direction and simply continued in the $[1\bar{1}0]$ direction of the surface. After a characterisation of the

observed magnetic structure in more detail, the effect of spin-orbit coupling is introduced which is exploited when investigating the topics of the last sections of this chapter. Temperature-dependent measurements reveal a coverage-dependent reorientation transition temperature of the magnetic structure of the DL stripes with a temperature- and coverage-independent magnetic period (Sec. 4.3). Finally the direction of domain walls is investigated with the surprising result that domain walls in DL stripes of Fe on W(110) always run approximately along the $[1\bar{1}0]$ direction of the surface. This observation gave rise to Monte-Carlo simulations to analyse this phenomenon (Sec. 4.4) which can also be understood phenomenologically on the basis of a simple model. The chapter closes with a section on chirality and the application of fundamental principles to the double-layer Fe on W(110) system (Sec. 4.5).

The STM measurements were performed with two different microscopes (described in Chap. 3.2). While the cryo-STM measurements presented in this chapter originate from previous work according to the references, the measurements done with the VT-STM show new results. Details on preparation techniques are given in Chap. 3.3.

4.1 Structure, growth, magnetic anisotropy

The structure of Fe on W(110) depends on various parameters, for example coverage and growth temperature. One feature of this system with extensive consequences is the large lattice mismatch between the two materials (lattice constant of W: $a_W = 3.165 \text{ \AA}$ and of Fe: $a_{\text{Fe}} = 2.8665 \text{ \AA}$ [37]) which leads to high strain in the pseudomorphic growth regime. As a result a layer-dependent topographic structure in the low coverage regime is observed. Figure 4.1 shows a sample of Fe on W(110) with total coverage $\theta = 2.5 \text{ ML}$. Fe was deposited onto the sample

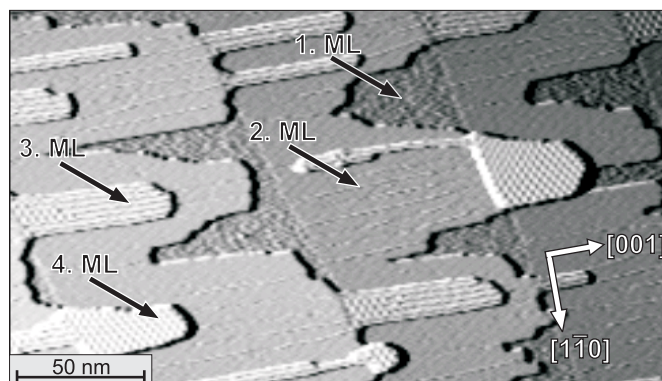


Figure 4.1: Sample of 2.5 ML Fe on W(110) grown at $T = 500 \text{ K}$, local coverage is indicated in monolayers.

held at elevated temperature ($T = 500$ K). Areas with different local coverage are observed and indicated in monolayers. Fe grows pseudomorphically only for the first monolayer. The large lattice mismatch leads to the formation of sporadic dislocation lines in the 2nd ML along the $[001]$ direction of the surface. They form a regular pattern for the 3rd ML and areas with local coverage of 4 ML up to 12 ML show a two-dimensional reconstruction network with a lattice constant of 40.5 \AA in $[\bar{1}10]$ and 28.6 \AA in the $[001]$ direction. At higher coverage Fe is completely relaxed and reaches the bulk Fe lattice constant [38, 39].

By varying the substrate temperature during or after deposition of Fe, the growth mode can be controlled. A wetting layer of one monolayer is always observed, which is thermodynamically stable up to $T = 1000$ K [41]. In Fig. 4.2 the temperature-dependent growth modes are presented. When the substrate is held at room temperature, islands of the 2nd ML grow with their long axis along $[001]$ as shown in (a) [40, 42]. Moderate annealing of the substrate ($T = 500$ K) leads to step flow growth of the 2nd ML which is a simple way to prepare double-layer stripes (b). Higher temperatures lead to three-dimensional island growth on top of the one monolayer thick wetting layer (c) [15].

The monolayer is magnetised in the film plane along the $[\bar{1}10]$ direction of the surface with a Curie-temperature of $T_C = 230$ K [43]. The double-layer of Fe on W(110) has an out-of-plane magnetic anisotropy at low temperatures which leads to interesting magnetic structures (described in Sec. 4.2). For a local coverage of more than two monolayers the magnetic easy axis switches from perpendicular back to in-plane with yet another transition from the $[\bar{1}10]$ direction to the $[001]$ direction at approximately $\theta = 22$ ML [44]. Different magnetic structures are observed for three-dimensional islands depending on their size. Smaller islands form a single domain state while larger islands show magnetic vortices [15].

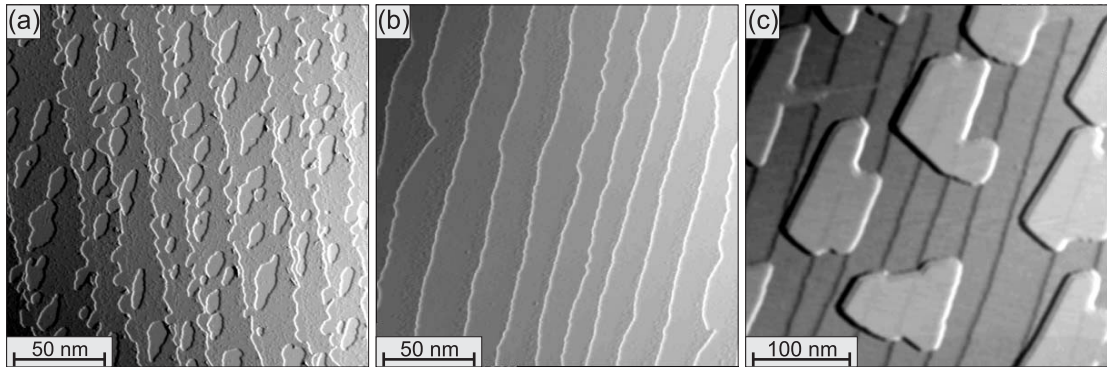


Figure 4.2: Temperature-dependent growth modes of Fe on W(110). (a) 1.3 ML Fe grown at room temperature $T = 300$ K [40]; (b) 1.7 ML Fe grown at $T = 500$ K [34]; (c) 2.0 ML Fe grown at $T = 700$ K.

4.2 Double-layer (DL) stripes: previous results

4.2.1 Magnetism and substrate miscut

When preparing a sample of $\theta = 1 - 2$ ML of Fe on W(110) with moderate annealing during deposition ($T = 500$ K) one induces step-flow growth which results in double-layer (DL) stripes separated by monolayer patches [12, 14, 32, 33, 36, 46]. At a measurement temperature of $T = 13$ K the DL stripes show a magnetic easy axis perpendicular to the surface [14, 32, 33, 36]. This means that the magnetic properties can be investigated using Gd/Fe-coated tips which are sensitive to the out-of-plane component of magnetism (see Chap. 3.3.2). The substrate miscut together with the total coverage determines the resulting magnetic structure of the DL stripes.

Fig. 4.3(a-c) shows topographies (upper panel) and dI/dU maps (lower panel) of Fe DL stripes on three different W substrates. For better visibility the dI/dU images have been inverted. The Fe DL stripes can be distinguished from sample locations which are covered by only one monolayer due to their different electronic properties. A dI/dU spectrum of the monolayer Fe on W(110) in comparison to the double-layer is shown in Fig. 4.3(d). In the dI/dU maps shown in Fig. 4.3(a) and (c) the darkest signal corresponds to the monolayer (not observed in (b)) while the medium and bright regions indicate the two oppositely magnetised domains of the double-layer. Figure 4.3(e) shows spin-resolved dI/dU spectra of two oppositely magnetised domains of the double-layer. The substrate with W terraces of width $w \approx 9$ nm (a) shows one-dimensional wires, each mainly magnetised homogeneously. A quasi antiferromagnetic coupling between adjacent stripes is observed due to dipolar interaction [12, 32, 33]. Wider terraces, and therefore also wider DL stripes, lead to the formation of domain walls due to the stray field of out-of plane areas (b) [14, 36]. The direction of the domain walls is approximately along the $[1\bar{1}0]$ direction of the surface. A closer inspection of this observation follows in Sec. 4.4. Depending on the total coverage and thus on the width of monolayer stripes separating the DL stripes, different coupling mechanisms are observed. Samples with a coverage very close to two monolayers show ferromagnetic coupling between adjacent DL stripes (b). When the DL stripes are separated by monolayer stripes quasi antiferromagnetic coupling between adjacent stripes is observed due to dipolar coupling and wider separating monolayer stripes lead to no distinct coupling at all (not shown here). In this thesis DL stripes are investigated which show a width larger than $w \approx 20$ nm, which is equivalent to about half of the magnetic period (see Sec. 4.3). Figure 4.3(c) shows a sample of 1.7 ML Fe on W(110) with $w \approx 60$ nm measured at $T = 75$ K with an Fe-coated tip (the in-plane sensitivity of this tip is not relevant for the interpretation in this context as shown in Sec. 4.2.2). The magnetic structure is found to be unchanged (c) in comparison to samples of terrace width $w \approx 20$ nm (b). The

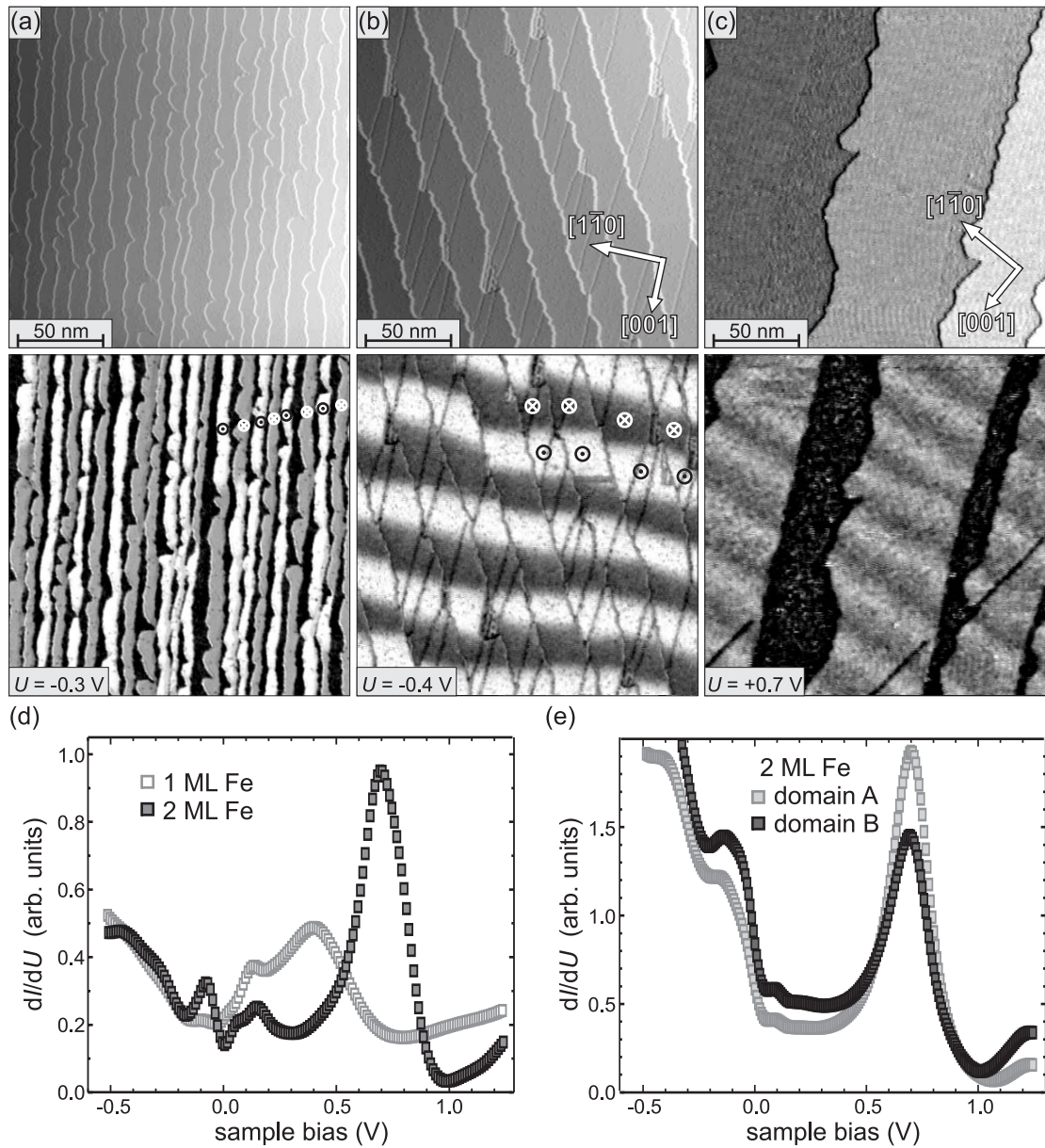


Figure 4.3: Samples of Fe on W(110) with different substrate miscut (a-c): topography (upper panel) and corresponding (inverted) dI/dU map (lower panel); (a) 1.7 ML Fe measured with a Gd/Fe-coated tip, $w \approx 9$ nm, the symbols illustrate the antiferromagnetic coupling between adjacent stripes [45]; (b) 2.1 ML Fe measured with a Gd/Fe-coated tip, $w \approx 20$ nm, the symbols illustrate the ferromagnetic coupling between adjacent stripes [29]; (c) 1.7 ML Fe measured with a Fe-coated tip, $w \approx 60$ nm, $T = 75$ K; (d) dI/dU spectra of 1 ML and 2 ML Fe on W(110) measured with a W tip; (e) spin-resolved spectra of 2 ML Fe on W(110) measured with a Gd/Fe-coated tip showing two oppositely magnetised domains A and B.

domains extend along the $[\bar{1}\bar{1}0]$ direction, while in the $[001]$ direction they seem to have reached the equilibrium size which is governed by the competition of the different relevant energies.

4.2.2 Magnetic structure of wide stripes

Since the domain walls separate patches of perpendicularly magnetised sample areas they have to include a magnetisation component in the film plane. To investigate their properties a Fe-coated tip was used which is sensitive to the in-plane component of the magnetisation (see Chap. 3.3.2). One distinguishes between walls of Bloch- and Néel-character. Bloch-type walls are magnetised parallel to the plane of the domain wall, while Néel walls show a direction of the spins perpendicular to the wall. In the case of the double-layer Fe on W(110) Bloch-type walls are considered to be more probable due to their smaller dipole energy. The consequence of these considerations is that the spins inside the wall must be aligned along the direction of the wall, i.e. $[\bar{1}\bar{1}0]$. Figure 4.4 shows dI/dU maps of DL stripes measured with a Gd/Fe-coated tip (a) and a Fe-coated tip (b). The alternating sequence of perpendicularly magnetised domains along each stripe is clearly visible in (a). In contrast, the perpendicularly magnetised domains cannot

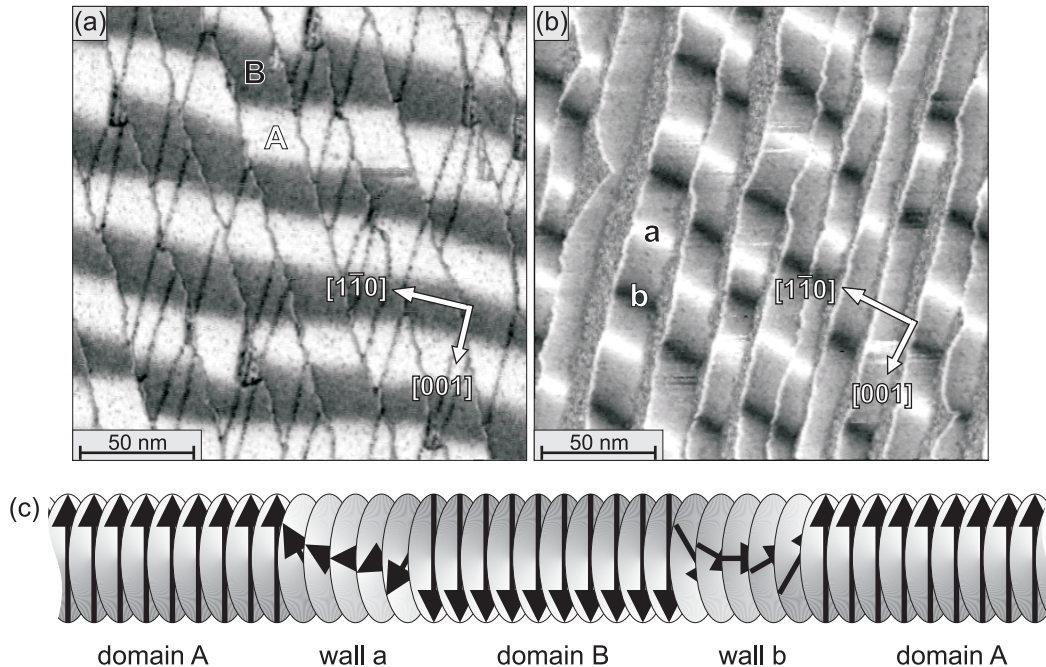


Figure 4.4: dI/dU maps of Fe double-layer stripes on W(110). (a) $\theta = 2.1$ ML Fe, Ge/Fe-coated tip [29]; (b) $\theta = 1.8$ ML Fe, Fe-coated tip [36]; (c) sketch of the helical magnetic structure of the double-layer stripes.

be distinguished in (b) but due to the in-plane sensitivity of the magnetic tip the walls appear as bright or dark lines. It is eye-catching, that an alternating in-plane magnetisation component within the domain walls is present. Joining the results of the two dI/dU maps of Fig. 4.4(a) and (b) the consequence is an overall helical magnetic structure along the stripes as sketched in (c). Measurements applying a magnetic field have demonstrated that the relative sense of rotation is identical for all stripes in the investigated image area [36]. The absolute sense of rotation has not been identified up to now. Considerations about these surprising results are presented in Sec. 4.5.

4.2.3 Spin-orbit coupling

First-principles calculations for the system of the double-layer Fe on W(110) have shown that the spin-orbit-induced mixing between minority d_{xy+xz} and minority d_{z^2} spin states depends on the direction of magnetisation. The consequence is a different local density of states in the easy and hard axis of magnetisation. For experimental investigations this means that it is possible to gain information about the magnetic structure of this system with a non-magnetic tip. Due to spin-orbit coupling the electronic structure of the domains and domain walls is different which is detectable with W tips, as has been demonstrated previously [34, 35].

Figure 4.5 shows the topography (a) and dI/dU map (b) at $U = +0.05$ V of a sample of 1.7 ML of Fe on W(110) measured with a W tip. The dI/dU spectra on a domain and on a domain wall are plotted in the upper panel of (c). Due to the difference in work function the spectra are shifted by $\Delta E = 11$ meV with respect to each other. The inset shows a closer view of the energy regime in which the difference between the two spectra is significant. The normalised difference of the spectra is presented in the lower panel together with a corrected plot. It is clearly visible that at $E = +0.08$ eV a reduced dI/dU signal for the domain wall is observed in comparison to the domain, while at small negative sample bias the dI/dU signal of the wall is enhanced in comparison to the signal on the domain. This observation allows the interpretation of the dI/dU map in (b): the dark lines across the double-layer stripes correspond to domain walls. This effect is very useful to study properties of the magnetic structure without the time-consuming preparation of magnetically sensitive tips. It is expected to be a common phenomenon but its use requires detailed knowledge about the system under investigation.

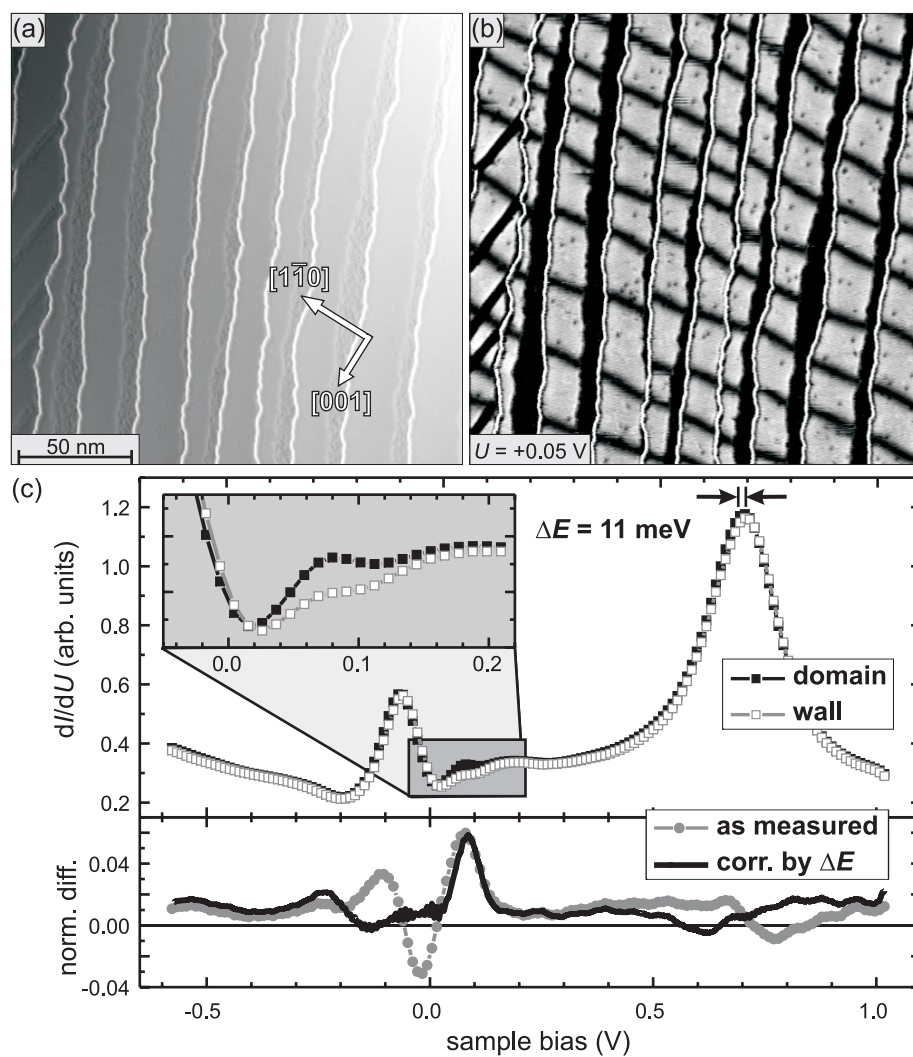


Figure 4.5: Effect of spin-orbit coupling observed on a sample of 1.7 ML of Fe on W(110) measured with a W tip [34]. (a) topography and (b) dI/dU map, domain walls are imaged as dark lines; (c) dI/dU spectra on domains and domain walls (upper panel) and normalised difference (lower panel).

4.3 DL stripes: magnetism and temperature

By using a variable-temperature STM the existence or absence of a known magnetic structure with temperature and coverage can be studied and the system of Fe on W(110) is investigated regarding these aspects. While the double-layer is magnetised perpendicular to the surface at low temperature there is a reorientation transition to an in-plane easy axis at higher temperature [46]. Samples with coverage $\theta = 1.5 - 2.2$ ML Fe on W(110) were analysed in the temperature range $T = 55 - 250$ K. The well-known helical magnetic structure of the DL stripes of Fe on W(110) (see Sec. 4.2.2) was identified via the observation of domain walls. This was done by taking advantage of the effect of spin-orbit coupling (see Sec. 4.2.3) to avoid the complicated preparation of magnetic tips for the VT-STM (see Chap. 3.3.2).

The experimental procedure as shown in Fig. 4.6 was performed for each sample: starting with a temperature where the domain walls were observed (a), the temperature was increased until the dI/dU signal was uniform on the DL stripes (b), i.e. after the breakdown of the known magnetic structure. A decrease in temperature then again led to a reappearance of the walls in dI/dU maps (c). At the bias voltage chosen for this measurement, $U = +5$ mV, the domain walls are imaged as bright lines (cf. Fig. 4.5(c)). The temperature range where the reorientation transition takes place was determined for samples with various coverage. Figure 4.7 shows some topographic images (upper panel) and dI/dU maps of samples with different coverage at temperatures below the reorientation transition. While in (a) and (b) only the first and second monolayer are present, in (c) layers up to

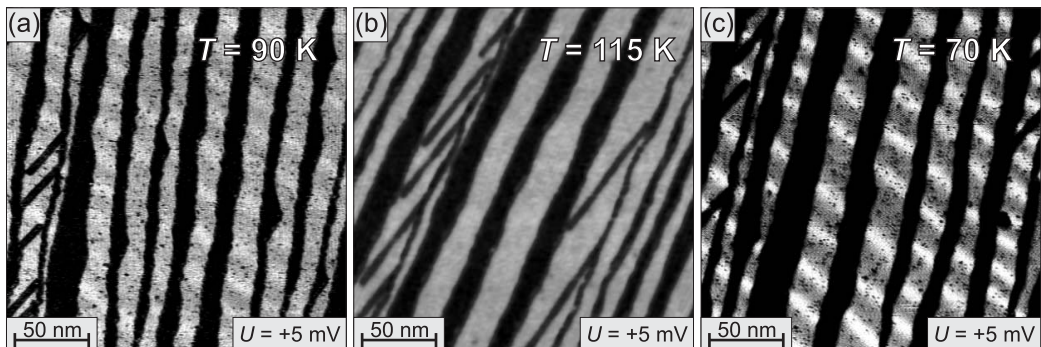


Figure 4.6: Experimental procedure: dI/dU maps of the same sample of 1.6 ML Fe on W(110) at different temperatures as indicated. (a) initial state; (b) above the temperature of the reorientation transition; (c) after reappearance of domain walls below the transition temperature.

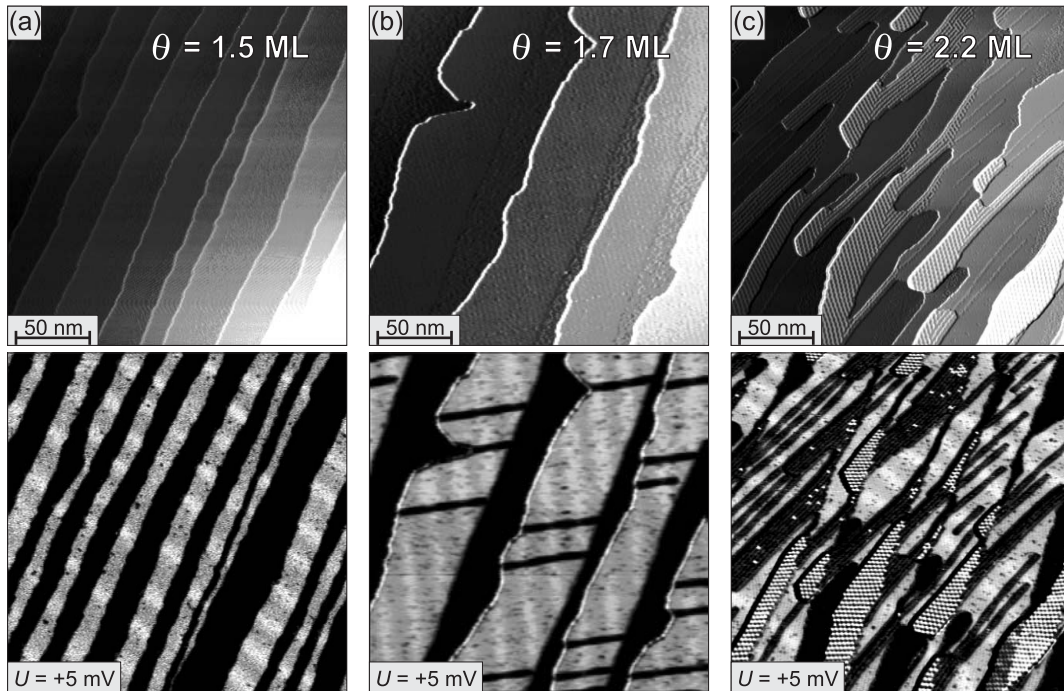


Figure 4.7: Experimental procedure: topography (upper panel) and dI/dU maps (lower panel) of samples of Fe on W(110) below the temperature of reorientation transition at different coverage as indicated. (a) $T = 75$ K; (b) $T = 120$ K; (c) $T = 125$ K.

the fourth monolayer can be observed. The magnetic domain walls of the double-layer of Fe on W(110) are still clearly visible. No hysteresis of the formation and breakdown of the well-known magnetic structure of the DL stripes was found on the time scale and the temperature accuracy of this STM measurement.

Figure 4.8 shows the dependence of the temperature of the reorientation transition on coverage. Sample areas with a terrace width $w = 25 - 60$ nm were investigated. Filled dots indicate data points where the magnetic structure was identified via the electronic contrasts of domains walls, hollow dots correspond to measurements where no electronic contrast was observed. A rise of the reorientation transition temperature is found with increasing coverage. At a coverage of $\theta = 1.6$ ML the transition is at approximately 100 K, at a coverage of 1.95 ML it is at $T \approx 220$ K. A maximum is observed close to $\theta = 2.0$ ML. As soon as the third monolayer starts to nucleate the temperature of the transition decreases which can be understood phenomenologically on the basis of the in-plane magnetic anisotropy of this layer. The measured data corresponds well to measurements of the magneto optical Kerr effect (MOKE) which have been performed at $T = 165 \pm 10$ K. Out-of-plane remanence has been observed for coverage $\theta = 1.8 - 2.1$ ML [12].

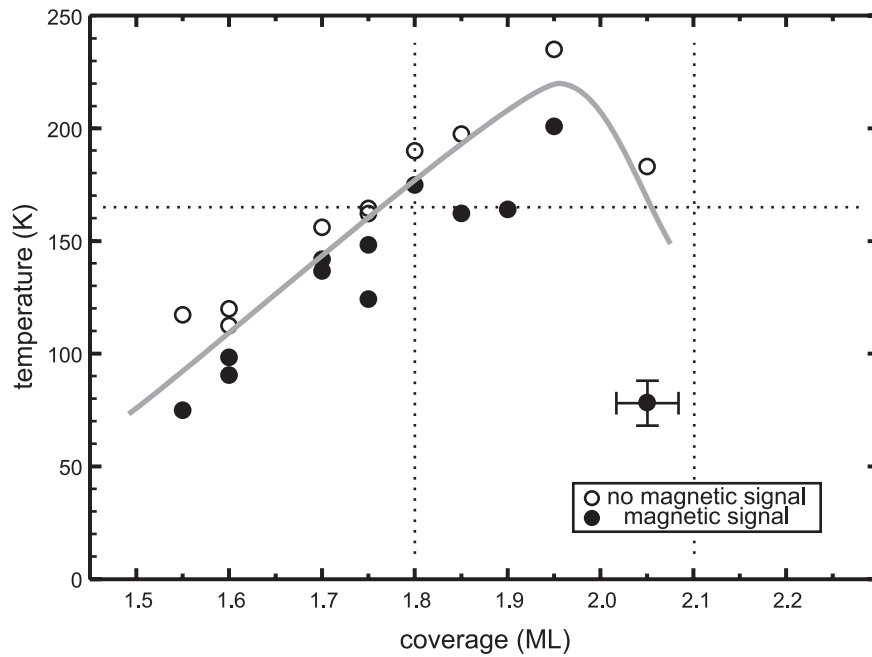


Figure 4.8: Data from dI/dU measurements of different samples of Fe on W(110) acquired with a W tip. The coverage-dependent reorientation transition temperature lies in the regime between filled and hollow dots. An estimate of the error is indicated for one data point, the grey line is simply a guide to the eye and dotted lines refer to MOKE measurements [12].

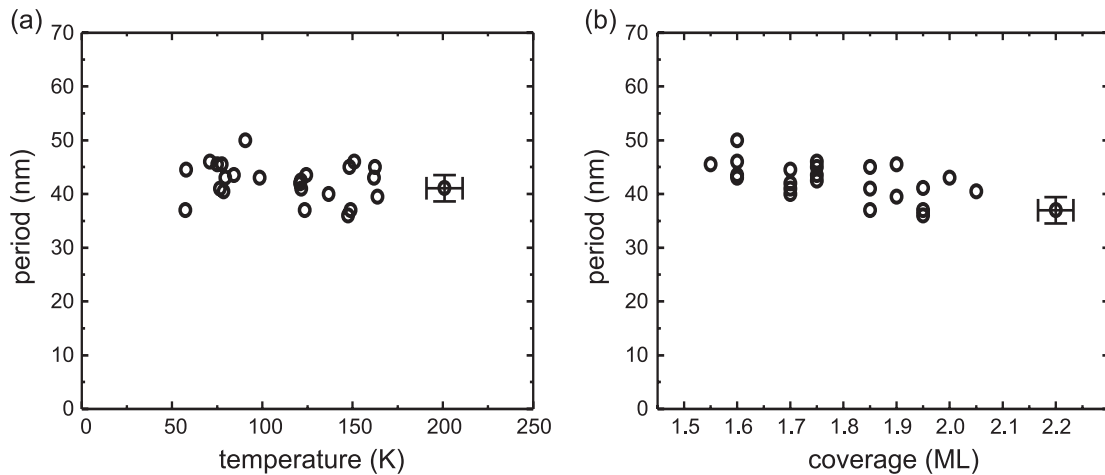


Figure 4.9: Data from dI/dU measurements of Fe on W(110) with a W tip: period versus (a) temperature and (b) coverage, an estimate of the error is indicated for one data point.

The period of the helical magnetic structure in the temperature and coverage regime investigated was also analysed. Figure 4.9 shows that the period does not depend either on temperature or on coverage. The period has a value of $P = 42 \pm 3$ nm, regardless of the other parameters. This means that the ratio between stray field and domain wall energy is unchanged in this regime [2].

4.4 DL stripes: direction of domain walls

In this section a detailed investigation of the direction of the domain walls with respect to the crystallographic axes in the system of the DL stripes of Fe on W(110) is presented. Previous work on this system has shown that the angle between the domain walls and the long axis of the DL stripes is approximately 80° (see Figs. 4.3, 4.4 and 4.5). This result is in contradiction to the expectation that the domain walls are always aligned along the shortest possible distance due to their large energy. However, this system seems to show a correlation between domain wall direction and the $[1\bar{1}0]$ direction of the surface.

To study this phenomenon in more detail a single crystal of W(110) with a variety of miscut orientations was chosen. This means that on different areas of the crystal the steps may run along different directions with respect to the high-symmetry axes of the surface. Thus DL stripes with any direction of the long axis can be observed. The measurements were performed with the VT-STM (described in Chap. 3.2.1) to take advantage of its ability to access different areas of one and the same sample with the x, y -positioning facility. Again, the effect of electronic structure variations due to spin-orbit coupling was used to identify domain walls (see Sec. 4.2.3). Figure 4.10 shows the topography (a) and three differential conductance maps (b-d) of a sample of $\theta = 1.7$ ML of Fe on W(110) grown at $T = 500$ K. The dI/dU map of Fig. 4.10(b) was measured simultaneously with the topographic image, the dI/dU maps of Fig. 4.10(c) and (d) show areas of the same sample which exhibit different local miscut orientations. The DL stripes shown in (a,b) extend approximately along $[001]$, the ones in (c) along $[1\bar{1}0]$, while in (d) the stripe direction is intermediate. Due to unequal diffusion energies along the two high-symmetry axes of the surface the Fe stripes grow smoothest along the $[001]$ direction of the surface and DL stripes along $[1\bar{1}0]$ do not show a regular boundary [47]. At the bias voltage chosen for this measurement, $U = +5$ mV, the domain walls are imaged as bright lines (cf. Fig. 4.5(c)). The crystallographic axes of the surface can easily be identified with the knowledge, that the dislocation lines always run along the $[001]$ direction (see Sec. 4.1). At $U = +5$ mV they are imaged as narrow dark lines in the dI/dU maps. Analysis of the measurements reveals that regardless of the direction of the DL stripes with respect to the crystallographic axis of the surface, the domain walls run approximately along the $[1\bar{1}0]$ direction, i.e. perpendicular to the dislocation lines. As a consequence, the

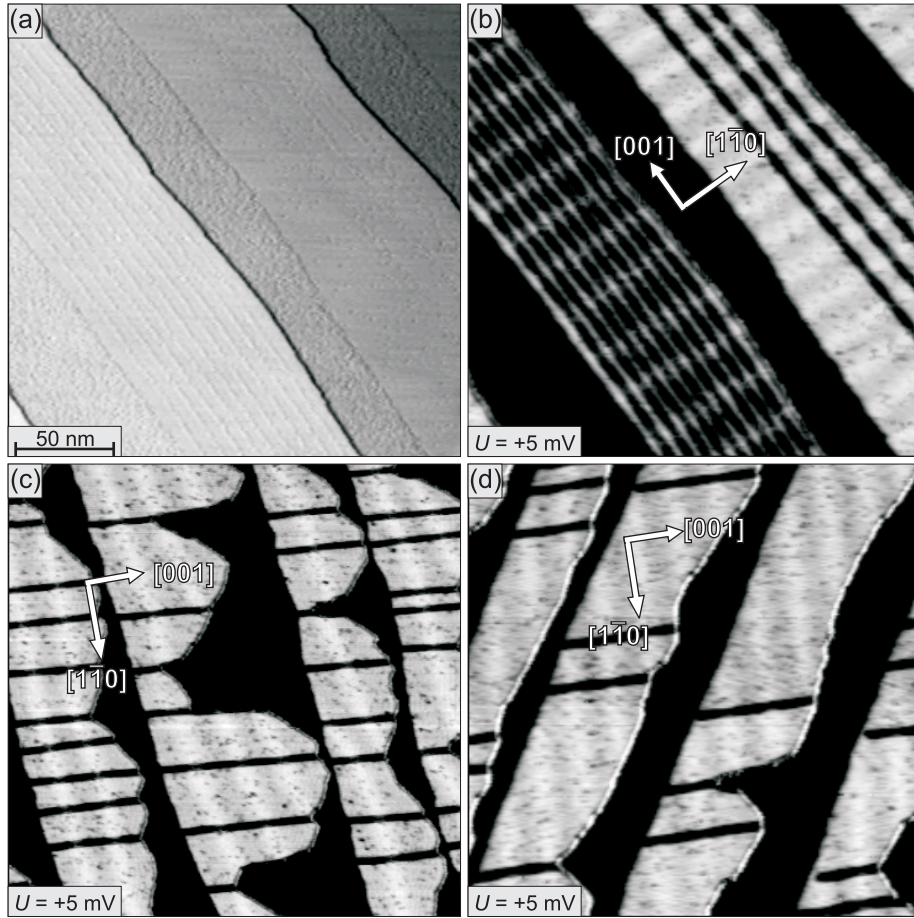


Figure 4.10: Sample of 1.7ML Fe on W(110). (a) topography; (b) corresponding dI/dU map; (c),(d) dI/dU maps at different local miscut orientations; the lateral scale is the same in all images; domain walls on the double-layer (bright lines) are oriented along $[1\bar{1}0]$, regardless of the orientation of the double-layer stripes, (a-c) $T = 75$ K and (d) 120 K.

domain walls within the DL stripes are infinitely long in the case of Fig. 4.10(c) (disregarding interruptions due to structural imperfections), and very short in case of (b) where they run perpendicular to the long axis of the DL stripes.

A theoretical approach to explain these surprising results has been performed using Monte-Carlo simulations [48]. The influence of the discrete nature of an atomic lattice on the orientation of domain walls in nanometre scale structures has been studied. First an ideal body-centred cubic (bcc) (110) double-layer has been investigated and then the system of the double-layer Fe on W(110) has been considered. Figure 4.11(a) shows the dI/dU map of a DL stripe of Fe on W(110). The long axis of the stripe is approximately along $[1\bar{1}\bar{1}]$ and the domain

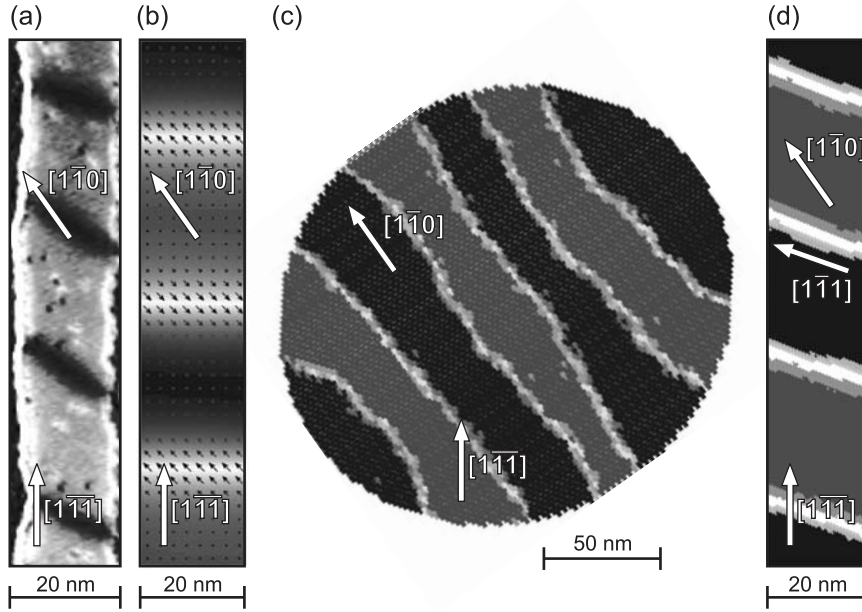


Figure 4.11: Comparison between experiment and two different simulations [48]. (a) dI/dU map of a double-layer stripe of Fe on W(110), domain walls are imaged as dark lines; (b) simulation with a continuum theory; (c) Monte-Carlo simulation of a continuous double-layer with $J_1 = J_2$ and $J_3 = 0$; (d) Monte-Carlo simulation of a 20 nm wide double-layer stripe with $J_1 = J_2$ and $J_3 = 0$.

walls (imaged as dark lines) run approximately along $[1\bar{1}0]$. This result cannot be reproduced easily within a continuum theory. When an isotropic exchange is assumed the walls run perpendicular across the stripes, taking the shortest possible path. An in-plane anisotropy along $[1\bar{1}0]$ turns the spins within the wall but does not change the direction of the wall itself as shown in Fig. 4.11(b). Only when an anisotropic exchange is introduced, continuum theory shows a tilting of the domain wall [49], but it is not possible to distinguish between contributions from the non-fourfold lattice symmetry and the varying exchange integral.

Monte-Carlo simulations for an ideal continuous double-layer film with a bcc (110) surface and an isotropic nearest neighbour exchange ($J_1 = J_2, J_3 = 0$, cf. Fig. 4.12) produce domain walls that run preferentially along $[1\bar{1}0]$ as shown in Fig. 4.11(c). This result is consistent with the experimental results shown for the double-layer of Fe on W(110) in Fig. 4.10. When performing Monte-Carlo simulations for a stripe similar to the one shown in Fig. 4.11(a), i.e. with a width of 20 nm and the direction of the long axis along $[1\bar{1}1]$, domain walls along $[1\bar{1}1]$ are observed as shown in Fig. 4.11(d). Obviously there is a size effect, which is responsible for the tilting of the direction of domain walls from $[1\bar{1}0]$ in continuous films to a shorter domain wall length in narrow stripes (walls along $[1\bar{1}1]$).

These results can be understood phenomenologically on the basis of a simple model to calculate the energy of domain walls along the different directions. Figure 4.12 shows a unit cell of a double-layer with a bcc crystalline lattice and a (110) surface in a top view (a) and a perspective view (b). Black connections between atoms (1) indicate bonds for which the surface projection is along $[001]$. The projection of grey bonds ($2_I, 2_{II}$) is along $[1\bar{1}1]$ and $[1\bar{1}\bar{1}]$, while white bonds (3) run along $[1\bar{1}0]$ when considering the projection of the unit cell onto the surface. All bonds of one unit cell are sketched and four bonds 1 are observed (the ones on the border of the unit cell are counted as half because they belong to two unit cells), eight bonds 2 (four 2_I and four 2_{II}) and four bonds 3 (again bonds belonging to two unit cells) are counted as half). To obtain the domain wall energy per unit cell in this simple model, in a first step all projections of the bonds to the axis perpendicular to the plane of the wall were calculated. In the case of domain walls running along $[001]$ these are the projections of the bonds onto the $[1\bar{1}0]$ direction. The same calculations were done for walls along $[1\bar{1}0]$ and $[1\bar{1}1]$ (perpendicular axes are $[001]$ and $[3\bar{1}1]$ respectively) and the following projections (b_{\perp}) are derived:

	$b_{\perp 1}[a]$	$b_{\perp 2}[a]$	$b_{\perp 3}[a]$	
wall along $[001]$:	0	$\frac{1}{\sqrt{2}}$	$\frac{1}{\sqrt{2}}$	projection onto $[1\bar{1}0]$,
wall along $[1\bar{1}0]$:	$\frac{1}{2}$	$\frac{1}{2}$	0	projection onto $[001]$,
wall along $[1\bar{1}1]$:	$\frac{1}{\sqrt{6}}$	$\frac{\sqrt{3}}{2}$	$\frac{1}{\sqrt{6}}$	projection onto $[3\bar{1}1]$.

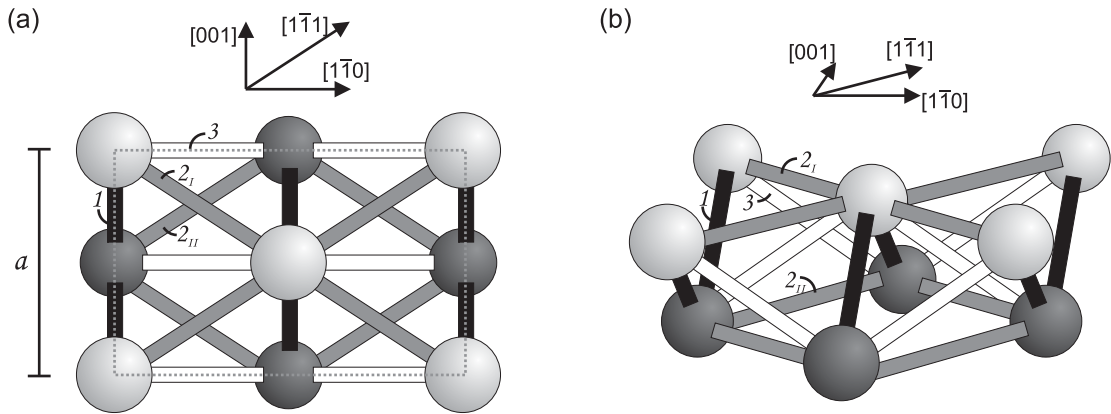


Figure 4.12: Sketch of the structure of a double-layer with a bcc crystalline structure with lattice constant a and a (110) surface [48]. (a) top view, dotted line indicates surface unit cell; (b) perspective view.

If an ideal bcc (110) surface is considered the black (1) and the grey (2) bonds are nearest neighbours while the white bonds (3) can be neglected. This can be simulated with exchange coupling constants (J) with a ratio:

$$J_1 : J_2 : J_3 = 1 : 1 : 0$$

The energy per unit cell for a wall along one of the directions $[xyz]$ can now be calculated by summing up the exchange coupling constant (J_i) multiplied by the projection of the bond length normal to the plane of the wall ($b_{\perp i}$) for all bonds (i) in the unit cell:

$$E_{[xyz]} [\text{arb. units /unit cell}] = \sum_i b_{\perp i} \cdot J_i \quad (4.1)$$

For a wall along $[001]$ this results in:

$$E_{[001]} [\text{arb. units}] = 4 \cdot (J_1 \cdot 0) + 8 \cdot (J_2 \cdot \frac{1}{\sqrt{2}}) + 4 \cdot (J_3 \cdot \frac{1}{\sqrt{2}}) = 8.52 \text{ per unit cell}$$

The calculation of the energy per unit cell for walls along the other directions can be performed similarly. The results calculated are:

$$\begin{aligned} \text{wall along } [001] &: 8.52 \text{ per unit cell,} \\ \text{wall along } [1\bar{1}0] &: 6.00 \text{ per unit cell,} \\ \text{wall along } [1\bar{1}1] &: 6.76 \text{ per unit cell.} \end{aligned}$$

This demonstrates, that the energy of a domain wall per unit cell is smallest for the $[1\bar{1}0]$ direction in agreement with the experiments and the Monte-Carlo simulation. Additionally the size effect observed in the Monte-Carlo simulations can be understood because of the relatively small energy difference of 11% between walls along the $[1\bar{1}0]$ and the $[1\bar{1}1]$ direction.

To apply the Monte-Carlo simulation and the simple model to the system of the double-layer of Fe on W(110) one has to take into account more realistic parameters due to lattice relaxations as well as resulting deviations of the exchange coupling constants J_i . As a result of the pseudomorphic growth of Fe on W(110) the bonds lying in the projection to the surface plane are elongated in comparison to the ideal bcc (110) double-layer of Fe. In contrast, the bonds between first and second layer are shortened due to an inward relaxation of the surface layer. This means, that instead of six nearest neighbour bonds (two times 1 and four times 2) also the bonds with the projection along $[1\bar{1}0]$ (two times 3) have to be taken into account, i.e. eight neighbours have to be considered and J_3 is non-zero.

The calculation of the exchange stiffness of Fe films on W(110) has been reported [50]. For one monolayer a ratio of 1 : 4 has been found for the $[001]$ compared to the $[1\bar{1}0]$ direction and this tendency remains the same for the double-layer. When taking lattice relaxations into account and assuming three different

exchange constants for non-equivalent pairs of neighbouring magnetic moments, the Monte-Carlo simulations on a discrete lattice are consistent with the experimental results. Based on the reported exchange stiffness calculations [50] the ratio of exchange coupling constants assumed is:

$$J_1 : J_2 : J_3 = 1 : 2 : 4$$

Figure 4.13(a) shows the same dI/dU image of a double-layer stripe of Fe on W(110) as already shown in Fig. 4.11(a). In Fig. 4.13(b) the result of Monte-Carlo simulations with the more realistic values for the exchange coupling constants J_i for a 20 nm wide stripe is presented. The agreement between experiment and Monte-Carlo simulation is better in this case than for an ideal bcc lattice (see Fig. 4.11(a) and (d)). In Fig. 4.13(c) a 40 nm wide section of the dI/dU map of Fig. 4.10(c) is presented with the long axis of the Fe double-layer stripe approximately along $[1\bar{1}0]$ and domain walls imaged as bright lines. Figure 4.13(d) shows the Monte-Carlo simulation of a 40 nm wide stripe with the long axis along $[1\bar{1}0]$, and domain walls running mainly parallel to this direction. Comparison between Fig. 4.13(c) and (d) proves the good agreement between the experiments and the results of the Monte-Carlo simulations.

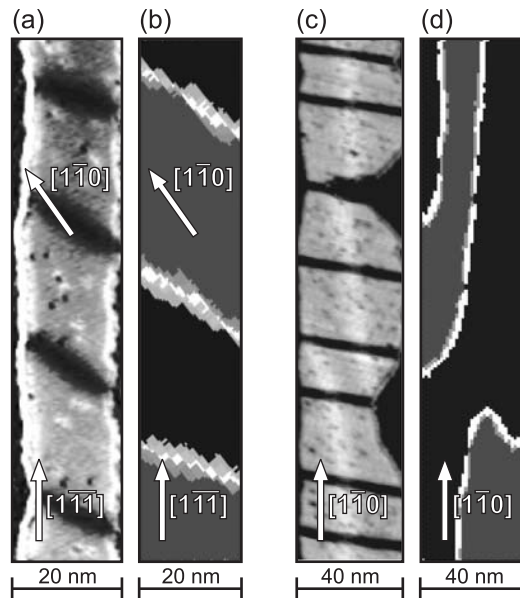


Figure 4.13: Comparison between experiments and Monte-Carlo simulations [48]. (a),(c) dI/dU maps and (b),(d) Monte-Carlo simulations with $J_1 : J_2 : J_3 = 1 : 2 : 4$ for double-layer stripes of Fe on W(110) with different directions of the long axes.

Again this result of the Monte-Carlo simulation can be understood on the basis of the model introduced for the ideal bcc (110) double-layer when the realistic values for J_i of the double-layer Fe on W(110) are considered, and the following energies are calculated:

$$\begin{aligned} \text{wall along } [001] &: 22.72 \text{ per unit cell,} \\ \text{wall along } [1\bar{1}0] &: 10.00 \text{ per unit cell,} \\ \text{wall along } [1\bar{1}1] &: 15.16 \text{ per unit cell.} \end{aligned}$$

These results show that again the energy of a wall is smallest if it runs along $[1\bar{1}0]$. For these more realistic values of J_i the energy difference between walls running along $[1\bar{1}0]$ and $[1\bar{1}1]$ is larger and thus walls approximately along $[1\bar{1}0]$ are dominant. This leads to the conclusion that the domain wall orientation in ultrathin films is governed by the structure of the crystalline lattice and the (anisotropic) exchange interactions among the different lattice sites.

4.5 Chirality

Chirality stems from the Greek root *chiros* which means *hand*. Lord Kelvin's definition stated a century ago is as follows:

"I call any geometrical figure, or group of points, chiral, and say it has chirality, if its image in a plane mirror, ideally realised, cannot be brought to coincide with itself." [51]

In other words, if a molecule, or more generally speaking an object, is not superimposable on its mirror image, it is chiral. Pairs of image and mirror image are called *enantiomers*. They have identical physical and chemical properties except in the following two cases [52]:

- Chiral molecules rotate the plane of polarised monochromatic light. This is called optical activity. Enantiomers rotate the plane in opposite directions but to an equal amount.
- Enantiomers react at different rates with other chiral substances.

Reactions with chiral components

In chemistry there are some general principles for reactions involving chiral substances. Figure 4.14(a) shows a formula (top) and a sketch (middle) of the reaction of an achiral component with a racemic mixture (equal amounts of enantiomers). The product is again a pair of enantiomers which are energetically degenerate as sketched in the plot of the reaction pathway in the bottom panel. If both of the reactants are chiral four different products are possible as sketched in (b). Now the products consist of two pairs of enantiomers (indicated with ε). Those pairs

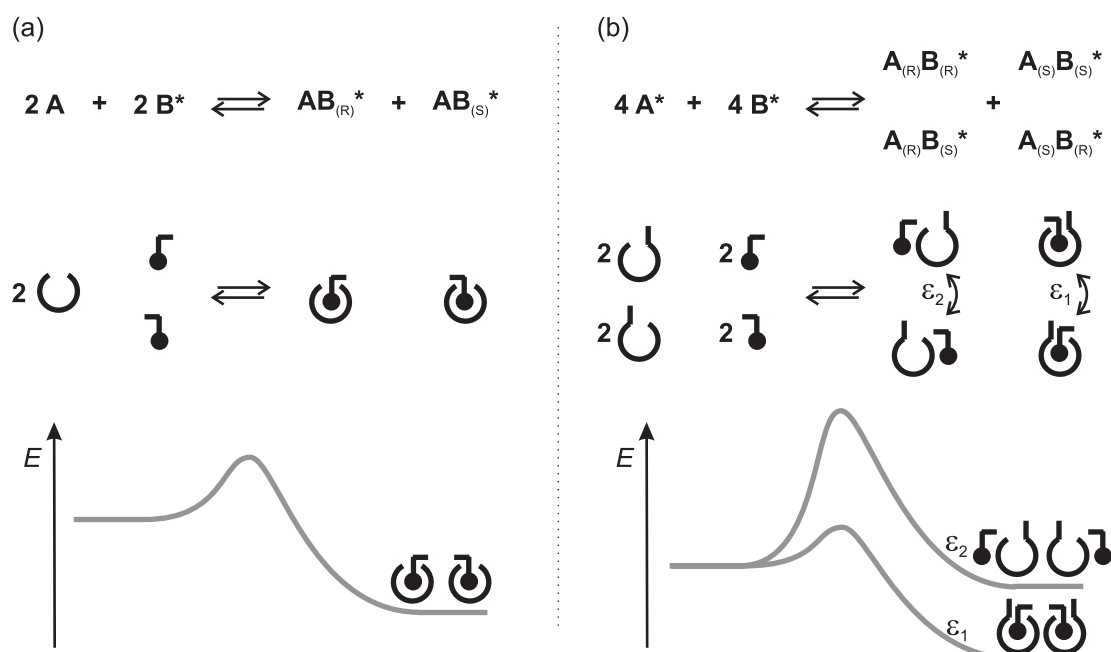


Figure 4.14: Reactions with chiral components (indicated with *): chemical reaction (top panel); illustration with symbols in terms of host-guest-complexes (middle panel); energy of the reaction pathway (bottom panel). (a) achiral component (A) and racemic mixture (B^*); (b) two racemic mixtures.

that are not enantiomers are called diastereomers. In opposition to enantiomers they are not energetically degenerate. A reaction pathway as sketched in the bottom panel of Fig. 4.14(b) would result in the formation of the enantiomers ε_1 but it is unfavourable for the formation of ε_2 . This is called selectivity and can be influenced via the reaction conditions.

Importance of chirality

Most amino acids, the fundament of life on earth, are chiral. Desoxyribosenucleic acids (DNA) are curled like helices in their ternary structure and are therefore chiral not only due to chemical bonds but also because of the configuration of the DNA-strand. Also a lot of receptors or structures inside the human organism are built up from chiral molecules or units. For this reason the pharmaceutical industry invests an extraordinary amount to synthesise enantiomer-pure substances or to separate racemic mixtures. The most prominent as well as alarming example of the enantio-selectivity of chemical interactions in the human organism is the drug *Thalidomide*: one enantiomer combats symptoms associated with morning sickness of pregnant women while the other enantiomer results in birth defects when taken during the first part of a pregnancy. This emphasises the importance of the

fabrication of pure enantiomers or the complete separation of racemic mixtures respectively. To synthesise chiral substances a convenient source of chirality is the so called *chiral pool*. One takes advantage of the fact that in nature there exists often only one enantiomer of a compound. Reaction with an achiral reactant results in a chiral product (see Fig. 4.14(a)). The separation of racemic mixtures can be performed via unequal interaction strength with chiral substances resulting in an excess of one of the two possible chiral products (see Fig. 4.14(b)).

Chirality at surfaces

The interaction of chiral molecules with surfaces has been studied intensely [53, 54, 55, 56]. A separation of enantiomers has been observed upon adsorption on single crystal surfaces. The mechanism can be understood on the basis of Fig. 4.14(a). The reaction of the racemic mixture of chiral molecules with the achiral surface results in a pair of enantiomers. The unequal interaction between these products leads to the formation of domains, one enantiomer covers the surface in one domain, while the other domain consists of the other enantiomer. Averaging over the whole surface the effect is cancelled out and no overall chirality remains.

Considering the system of Fe on W(110) general statements can be made about the chirality. Any layer with out-of-plane anisotropy and periodic Bloch-type walls is a magnetic helix, which is a chiral object. Any crystal surface with a non-zero miscut and its orientation unequal to the principal axes of the crystallographic directions, has terraces which do not have a mirror plane when considering the atomic structure. Thus this surface has an overall chirality if it is homogeneous, i.e. no variation of the orientation of the miscut. Now the system of the helical magnetic double-layer stripe of Fe on the chiral surface of W(110) is analogue to the example in Fig. 4.14(b). Since only one enantiomer of the two possible W(110) surfaces is present, only one product, i.e. 'reaction' with only one magnetic helix, will be energetically favourable.

This is a remarkable example of the mesoscopic chirality of an object, i.e. the result of polishing the crystal surface, imposed on another system, i.e. the magnetic helix, which hence is formed in only one enantiomer. The system has an overall chirality with units on the nanometre scale. A further investigation of this effect is desirable, particularly with regard to heterogeneous enantioselective catalysis.

Chapter 5

Oxygen on Fe/W(110)

Scanning tunneling microscopy (STM) and spectroscopy (STS) are powerful tools to study the interplay between structural and electronic properties of surfaces and to reveal the orbital symmetry of electronic states. A deeper understanding of magnetic properties requires the use of spin-polarised STM/STS investigations which yield further information about the spin character of the electronic states involved. By making use of the high spatial and energy resolution of STM and STS, modulations of the local electron density of states on the nanometre scale caused by scattering at impurities or step edges have been studied recently. The analysis of electron standing wave patterns has allowed the acquisition of characteristic properties as the symmetry of the wave function, dispersion relation or the lifetime of the electronic states [4, 6, 20, 57, 58, 59, 60, 61, 62]. All previous experiments have been performed with non-magnetic tips resulting in spin-averaged data, although scattering processes at magnetic impurities or at non-magnetic impurities on magnetic surfaces should result in spin-polarised (SP) electron waves. A well-studied magnetic model system is Fe on W(110) which has been investigated previously by means of spin-integrated and spin-polarised STM/STS measurements. The most important results are summarised in a previous chapter (see Chap. 4). To further investigate the electronic and magnetic properties of this system single oxygen atoms were adsorbed on the surface and the response of the system to the perturbation was studied.

After a short introduction to the preparation of isolated oxygen adsorbates on the double-layer Fe on W(110) (Sec. 5.1) this chapter starts with a presentation of spin-integrated measurements on this system. Highly anisotropic spatial oscillations in the local density of states (LDOS) in the vicinity of the adsorbates are observed (Sec. 5.2). This is explained in terms of a single-particle model as electron waves scattered at the potential induced by the presence of the oxygen atoms (Sec. 5.3). Analysis of the wavelength of the standing electron waves and comparison to *ab-initio* spin-resolved electronic structure calculations

reveal that minority-spin bands of d -like symmetry are involved in the scattering process (Sec. 5.4). After a conclusion of the results of the spin-integrated measurements (Sec. 5.5) the application of spin-polarised STS to this system is presented (Sec. 5.6). The standing wave patterns are observed on one particular type of magnetic domain only, which proves that the standing electron waves of the system of Fe on W(110) are indeed highly spin-polarised.

All STM measurements were acquired with the cryo-STM at $T = 13$ K (described in Chap. 3.2.2) and details on preparation techniques are given in Chap. 3.3.

5.1 Preparation

First a sample of double-layer (DL) stripes of Fe on W(110) was prepared as described in Chap. 4. Upon Fe deposition the sample surface was exposed to about 0.01% of a Langmuir of O_2 at room temperature. High-resolution electron energy loss spectroscopy (EELS) measurements have shown that the adsorption of oxygen on a clean Fe(110) surface leads to dissociative chemisorption with the O atoms located in the twofold long-bridge sites [63]. The direct determination of the adsorption site by STM has not been successful: even though atomic resolution was obtained on the Fe surface as shown in Fig. 5.1(a) the imaging of oxygen adsorbates has not been possible. Since there was an oxygen atom in the image area before, the adsorbate must have moved when measuring at the extreme measurement parameters used to achieve atomic resolution, presumably due to repulsive interaction between tip and adsorbate. The black cross in Fig. 5.1(b) marks the twofold long-bridge oxygen adsorption site in the sketch of a (110) surface. For each surface atom there exists one of these adsorption sites.

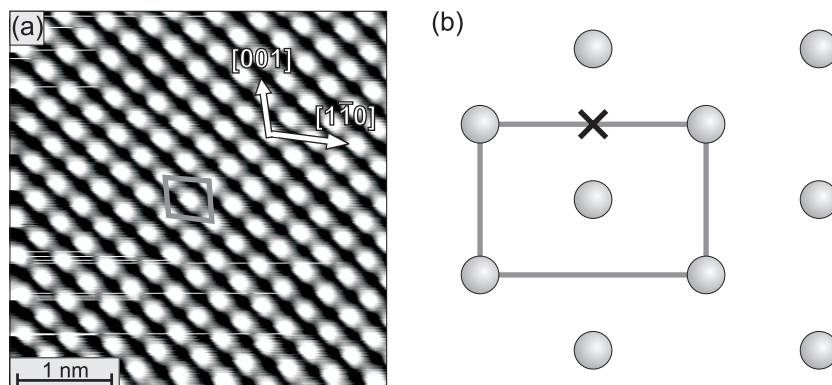


Figure 5.1: Adsorption site of O on Fe/W(110). (a) topography (raw data) with atomic resolution of the DL Fe/W(110) at $U = +1$ mV and $I = 40.0$ nA, the grey box marks a surface unit cell; (b) sketch of the atomic lattice for a Fe(110) surface, the grey rectangle marks a surface unit cell, the black cross marks the adsorption site of oxygen.

The constant-current topography of Fig. 5.2(a) and the corresponding dI/dU map in (b) show that the single oxygen adsorbates are distributed randomly and imaged as depressions on the DL stripes of Fe at a sample bias $U = +0.7$ V. The local tunnel spectra of Fig. 5.2(c) reveal that at the chosen stabilisation parameters oxygen locally causes an attenuation of the dI/dU signal for $U \leq +0.8$ V in comparison to spectra on clean Fe. Overall, the spectra are of approximately the same intensity. A more realistic ratio between the spectra can be estimated on the basis of the discussion of Fig. 2.6. It is well-known, that oxygen adsorbates are imaged as depressions in STM topography images due to a reduced density of states compared to that of the metal. When performing dI/dU spectroscopy the tip is stabilised at the given parameters U and I . This results in dI/dU spectra, which show the same integral from U to E_F , regardless of the specific sample properties. Since the density of states of O is much lower compared to that of Fe, a much lower intensity is expected in comparison to the experimental data. This effect can be calculated quantitatively on the basis of Eq. 2.19 when the work function is known (see Chap. 2.4). If the work function of $\phi = 5.1$ eV for Fe [64] is considered to be unchanged by the adsorption of oxygen, the normalised dI/dU spectra can be calculated. The measured height difference Δz between the Fe surface ($z = 0$) and the centre of the oxygen adsorbate is -0.15 Å. To simulate constant-height conditions these values are put into Eq. 2.19. Since $z_{\text{Fe}} = 0$ the Fe spectrum is unchanged, but the spectrum on top of the oxygen atom has to be corrected by a factor of 0.71. The normalised spectrum for oxygen is shown in Fig. 5.2(c) as a dotted line. The correction leads to a O spectrum which is lower in intensity than the Fe spectrum for all energies.

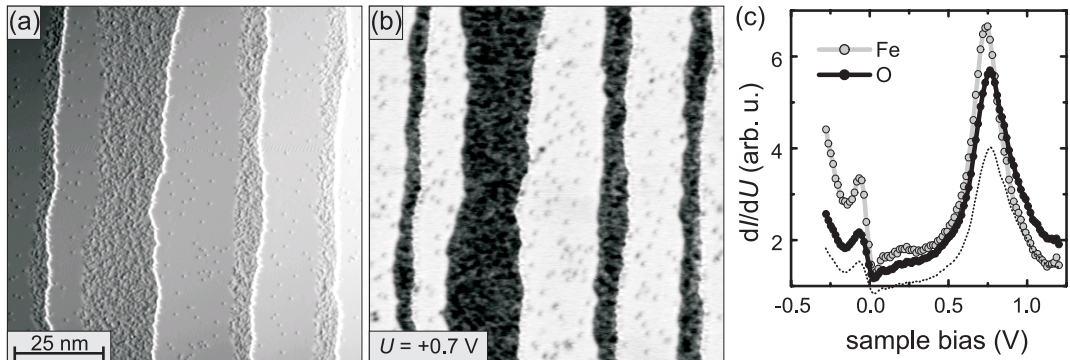


Figure 5.2: STM/STS measurements of 1.8 ML Fe on W(110) after dosing about 0.01% L of O_2 . (a) topography; (b) corresponding dI/dU map; (c) dI/dU spectra on the double-layer of Fe/W(110) and on top of an oxygen atom (stabilisation parameters: $U = +1.2$ V, $I = 0.5$ nA), the dotted line shows a correction of the O spectrum.

5.2 LDOS oscillations

Figure 5.3 shows a high-resolution topography image (a) and corresponding dI/dU maps around a single oxygen atom at $U = +0.3$ V (b) and $U = -0.1$ V (c) as indicated. While the surface of the Fe double-layer shows no corrugation on the clean Fe surface strong variations in the local density of states (LDOS) are observed in the vicinity of the oxygen adsorbate. The patterns at both voltages are highly anisotropic and show a twofold symmetry axis normal to the surface. The black lines in the upper panel of Fig. 5.3 indicate the positions of the line profiles which are plotted in the lower panel. The topography image of Fig. 5.3(a) is acquired in constant-current mode (see Chap. 2.3) with the measurement parameters $U = +0.3$ V and $I = 0.25$ nA. A dip is observed at the position of the oxygen atom with a height difference to the Fe-surface of 0.3 Å. The dip has a conical shape and can be fitted by a gaussian with a full width at half maximum $\text{FWHM} \leq 0.5$ nm. The disturbance in the slow scan direction (vertical) indicates a movement of the oxygen atom due to interactions with the tip in the fast scan direction (horizontal). The Fe surface outside the dip is imaged as a plane with no height variations. In the dI/dU map shown in Fig. 5.3(b) oscillations along the $[001]$ direction of the substrate are observed with a maximum of the dI/dU signal

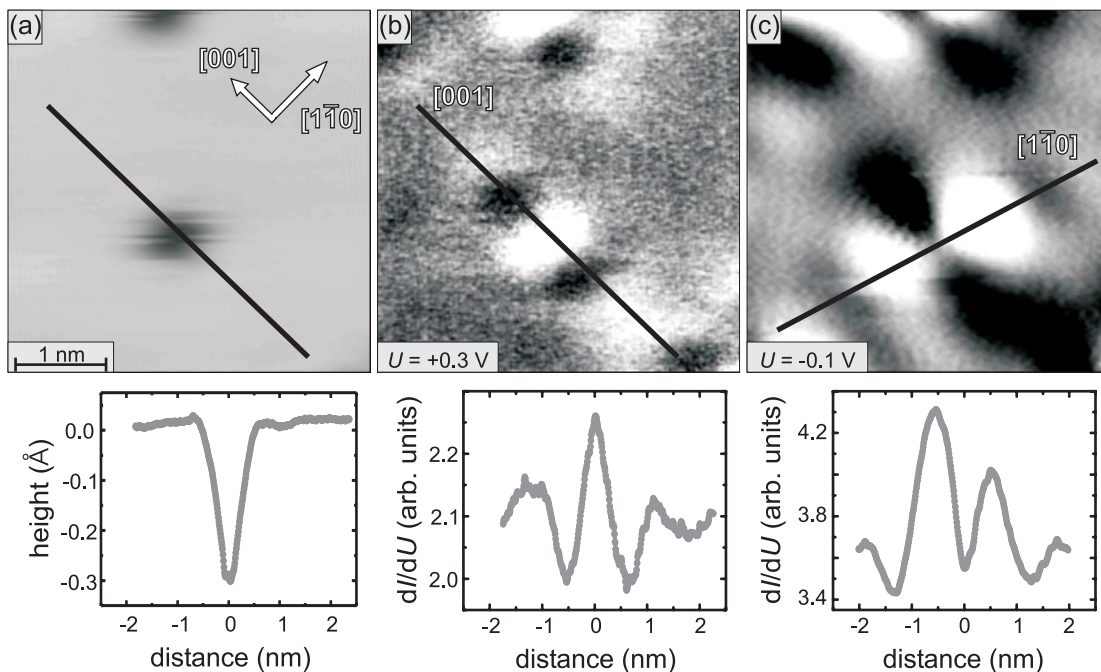


Figure 5.3: Single oxygen adsorbate on Fe on W(110) measured with a W-tip. (a) topography; (b),(c) corresponding dI/dU maps, the lines indicate the positions of the profiles shown in the bottom panel.

at the centre of the oxygen atom (distance $d = 0$ nm). In Fig 5.3(c) the dI/dU map measured at $U = -0.1$ V shows oscillations along the $[1\bar{1}0]$ direction of the substrate. At this particular voltage and $d = 0$ nm a saddle point in the dI/dU map is observed with a local minimum along $[1\bar{1}0]$ but a local maximum along $[001]$. The oscillations of the dI/dU signal show a strong attenuation with increasing distance from the centre of the oxygen adsorbate.

To further investigate the oscillations spatially resolved full dI/dU spectroscopy was performed around single oxygen adsorbates in an image area as shown in Fig. 5.3. With this technique a three-dimensional data set is acquired. Two dimensions are the x and y position of the tip, the third dimension is the energy-resolved dI/dU signal. In other words, full dI/dU spectroscopy is performed at each point (x, y) . Figure 5.4(a) shows smoothed data from this data set. The grey scale represents the dI/dU signal as a function of energy E and distance d from the oxygen adsorbate. The data presented is a cut through three-dimensional parameter space parallel to the $[001]$ direction of the surface including the centre of the oxygen atom at $d = 0$ nm. This means that the data set contains information about spatial oscillations along $[001]$ not only at $U = +0.3$ V as shown in Fig. 5.3(b) but in the whole energy regime of the spectroscopic data. As can be seen in Fig. 5.4(a) the grey scale is white for energies below the Fermi energy E_F . The reason is the comparably high dI/dU signal of the surface at these energies as can be deduced from the spectrum of the clean Fe double-layer in Fig. 5.4(b). For better visibility the dI/dU signal of the raw data has been normalised by dividing it by the dI/dU signal of the clean Fe surface at the corresponding energy:

$$dI/dU_{\text{norm}}(E, d) = \frac{dI/dU_{\text{raw data}}(E, d)}{dI/dU_{\text{Fe}}(E)}. \quad (5.1)$$

The normalised data is presented in Fig. 5.4(c) for the $[001]$ direction of the surface and a characteristic pattern in the dI/dU intensity can be recognised above the Fermi level E_F . The occurrence of maxima and minima in the local density of states is clearly visible. The same normalisation procedure (see Eq. 5.1) has been performed for the $[1\bar{1}0]$ direction and the result is shown in Fig. 5.4(d). The $[1\bar{1}0]$ direction shows a characteristic pattern of the LDOS below E_F .

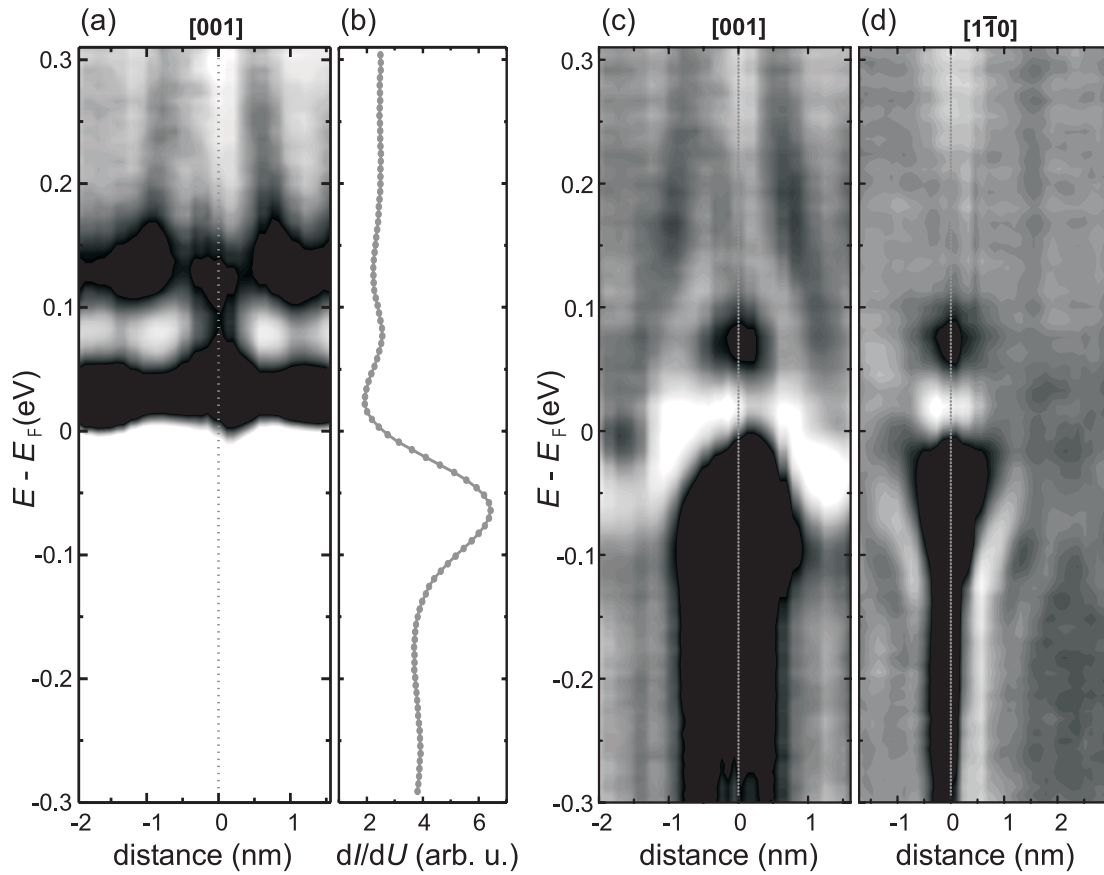


Figure 5.4: Data from dI/dU spectroscopy measured with a W tip (stabilisation parameters: $U = +0.3$ V, $I = 0.25$ nA) and method of normalisation for better visibility, position of the oxygen atom is at distance $d = 0$ nm. (a) smoothed data: energy-dependent dI/dU signal across a single oxygen adsorbate along [001]; (b) dI/dU spectrum of the clean Fe double-layer taken from the same set of full spectroscopy; (c) normalised plot of the dI/dU signal along [001] (logarithmic grey scale); (d) normalised plot of the dI/dU signal along [110] (logarithmic grey scale).

5.3 Scattering theory and analysis

The oscillations in the differential conductance are interpreted in terms of standing electron waves and explained within a single-particle model. In the proximity of impurities electron waves $\Psi(x)$ are scattered by the impurity potential $V(x)$ as sketched in Fig. 5.5(a). Coherent interference of the incoming with the reflected electron wave, $\Psi_i(x)$ and $\Psi_r(x)$ respectively, results in spatial oscillations of $|\Psi(x)|^2$ which correlates with the dI/dU signal of spectroscopic measurements. The real space surface unit cell and the surface Brillouin zone of a body-centred cubic (bcc) (110) surface are sketched in Fig. 5.5(b).

It has been reported that the analysis of standing wave patterns can be very complicated due to topographic effects [20]. The constant-current mode of operation with the STM does not guarantee a constant distance between the tip and the sample surface (see Chap. 2.3). Especially close to the Fermi energy E_F the standing wave patterns can be observed in topographic images as well, which results in large variations of the distance between the tip and the sample plane [4, 5, 6, 20, 57, 59, 60, 65, 66, 67]. The data shown in Fig. 5.4 stems from dI/dU spectroscopy acquired with an open feedback loop at the given stabilisation parameters. The topography shown in Fig. 5.3(a) was measured with the same parameters. As pointed out the observed dip at the oxygen atom can be described with a gaussian fit with a FWHM of less than 0.5 nm while no corrugation is present on the clean Fe double-layer. Therefore the data obtained with full dI/dU spectroscopy can be interpreted without normalisation (using Eq. 2.19) for data points more than approximately 0.5 nm away from the position of the oxygen atom, while an influence of the topographic effect is expected for smaller distances. In the following that data is analysed, which was measured at sufficiently large distance from the position of the oxygen atom, where the undisturbed oscillations

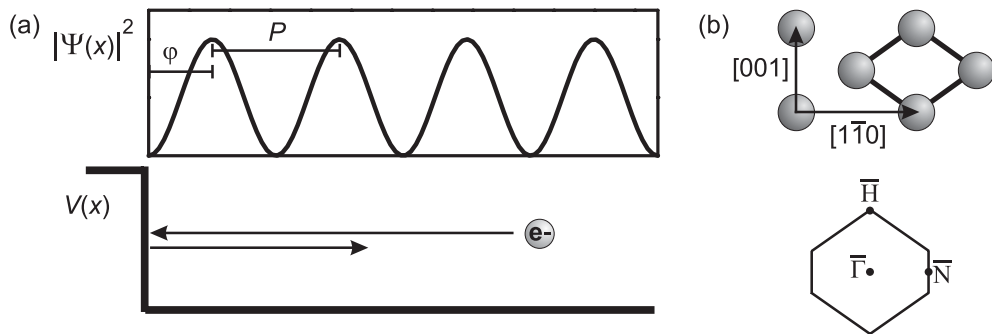


Figure 5.5: (a) Scattering of an electron at a potential $V(x)$ in a single-particle model (lower panel) and the resulting oscillations in the LDOS (upper panel); (b) atomic lattice and crystallographic axes of a bcc (110) surface, the black rhombus indicates the surface unit cell (upper panel), and corresponding first surface Brillouin zone (lower panel).

of the LDOS are observed and where topographic effects are negligible. In the simple single-particle model assumed, oxygen acts as a point scatterer with a very localised influence (≤ 0.5 nm) on the electronic structure of the Fe double-layer surface.

The real-space oscillations observed in Fig. 5.4 can be analysed regarding their periodicity P and phase φ (see Fig. 5.5(a)). The periodicity is connected to the wavelength λ of the electron wave $\Psi(x)$ via

$$P = \frac{\lambda}{2} \quad (5.2)$$

and thus contains information about the wave vector component \vec{k}_{\parallel} of the electron wave:

$$|\vec{k}_{\parallel}| = \frac{2\pi}{\lambda}. \quad (5.3)$$

The phase of the standing wave can be deduced from the distance from the first maximum of the oscillation pattern to the position of the point scatterer. This distance in relation to the wavelength results in the phase, where one wavelength corresponds to 2π .

By analysing the oscillations in the LDOS of Fig. 5.4(c) and (d) the following parameters for both high-symmetry directions have been obtained:

- the relation of the periodicity P to the energy E
- the energy-dependent phase

The real space surface unit cell can be correlated to the first surface Brillouin zone of a bcc (110) surface as shown in Fig. 5.5(b)): the [001] direction corresponds to $\overline{\Gamma\text{H}}$ in reciprocal space and the $[1\bar{1}0]$ direction to $\overline{\Gamma\text{N}}$.

5.4 Comparison: experiment and calculation

The experimental results are compared to first-principles electronic structure calculations based on density functional theory. Figure 5.6 shows the calculated spin-resolved band structure of 2 ML Fe adsorbed pseudomorphically on either side of a five layer W(110) slab [68]. Minority and majority bands are plotted as black and grey lines, respectively. From the data in Fig. 5.4(c) and (d) the periods of the standing waves at various energies were extracted and the k -vectors of the corresponding electron wave functions are calculated using Eqs. 5.2 and 5.3. This allows the comparison of experimental and calculated data. The oscillations in [001] can be assigned to a rising minority-spin band in the $\overline{\Gamma\text{H}}$ direction indicated by the arrow in Fig. 5.6. An analysis of the eigenstates reveals that this band consists basically of a superposition of d_{z^2} - and d_{zy} -like states in the Fe surface layer.

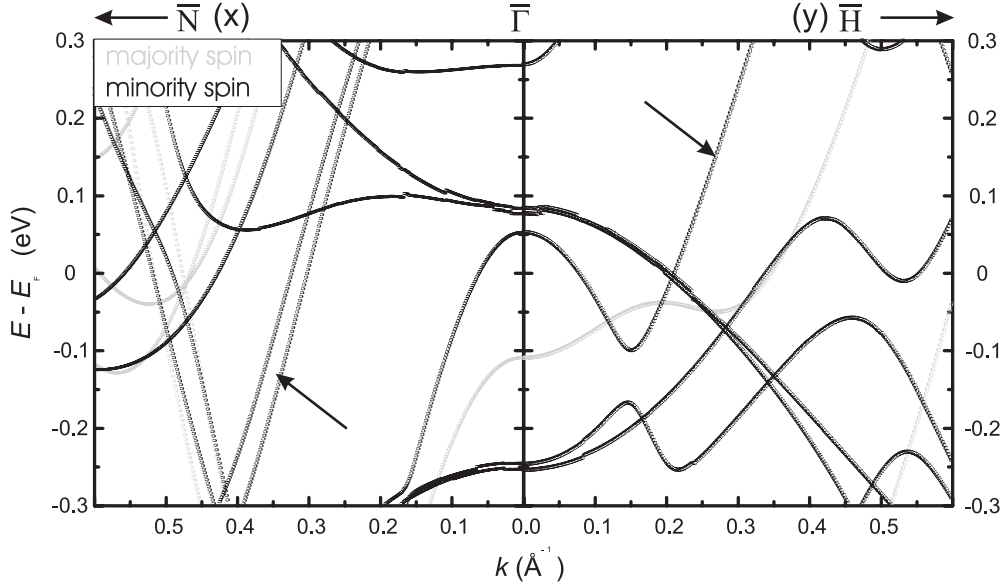


Figure 5.6: Spin-resolved band structure calculation for 2 ML Fe/W(110) [68].

10% of this state is localised in the vacuum, measured at a position 1.2 \AA above the surface Fe layer. The oscillations in $[1\bar{1}0]$ result from scattering involving one of the two bands which are indicated by the arrow in the $\bar{\Gamma}\bar{N}$ direction. Both are of minority-spin character. The band closer to $\bar{\Gamma}$ is a d_{zx} -like state in the Fe surface layer with 8% of its weight localised in the vacuum. The other one is a superposition of d_{z^2-} , d_{zx} - and $d_{x^2-y^2}$ -like states in the Fe surface layer and only 1% is localised in the vacuum. For this reason it is assumed that the band visible in the scattering process is the one closer to $\bar{\Gamma}$. As shown below these two bands allow a precise modelling of the observed dispersion of maxima and minima in the dI/dU signal.

Comparison of the calculated band structure of Fig. 5.6 to the scanning tunneling spectroscopy measurements was done by evaluating the bands identified to be involved in the scattering process as shown in Fig. 5.7 for the $[001]$ direction. The relevant section of the band structure is plotted in (a). Regarding Eqs. 5.2 and 5.3 the energy-dependent wave vector k can be transformed into the energy-dependent electron wavelength λ which is shown in (b). When a phase $\varphi = 0^\circ$ is considered, λ is the distance from the position of the scatterer to the first maximum in the local density of states, which is proportional to the STS signal. Then at all distances corresponding to multiples n of λ there are maxima, while at $(n+0.5)\lambda$ there are minima in the local density of states as sketched in Fig 5.7(c).

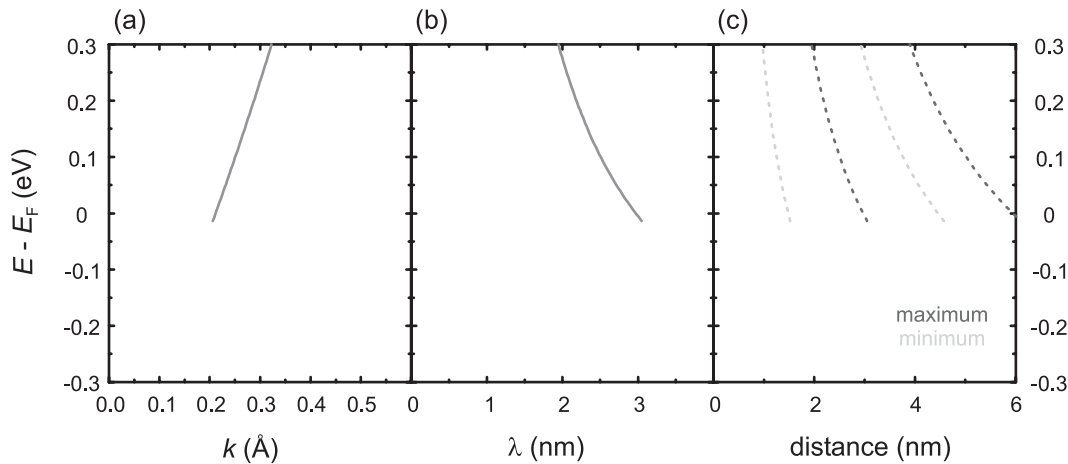


Figure 5.7: Simulation of maxima and minima of LDOS for the scattering process in the [001] direction. (a) the band identified to be involved in the scattering process for the [001] direction; (b) the energy-dependent wave vector k is transformed into the energy-dependent electron wavelength; (c) maxima and minima in the density of states for a phase $\varphi = 0^\circ$.

After correction with the experimentally determined energy-dependent phase the positions of the maxima and minima of the density of states can be simulated as function of energy and of distance from the centre of the oxygen atom. The result is shown in Fig. 5.8 together with data from dI/dU spectroscopy for both high-symmetry directions (dI/dU data is the same as in Fig. 5.4(c) and (d)). The black and white dotted lines in the graphs for the high-symmetry directions of the surface indicate the minima and maxima, respectively, which were simulated on the basis of the band structure calculation. The experimentally determined and simplified energy-dependent phase is shown to the right side of the dI/dU spectroscopy data. In the phase derived for the [001] direction a phase shift at E_F of around $-\frac{\pi}{2}$ is observed. This is identified as an energy-independent background phase as also assumed for other scatterers [4, 6]. A phase shift of π is centred at around $E = +0.15$ eV. The $[1\bar{1}0]$ direction shows a characteristic pattern of the density of states below E_F with a similar phase relation as for [001] and an inflection point at approximately $E = -0.08$ eV. An explanation for an energy-dependent phase shift of π could be a resonance at the inflection point.

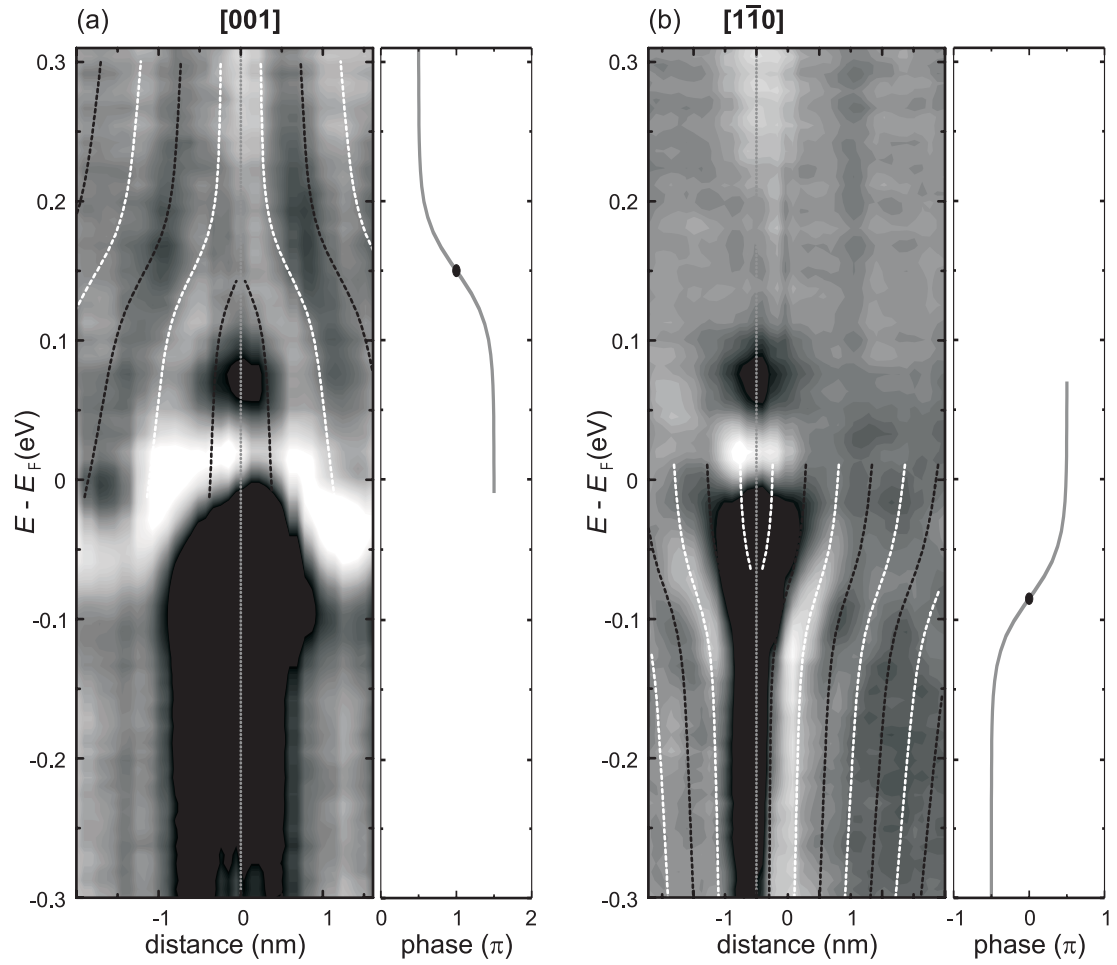


Figure 5.8: Data from dI/dU spectroscopy (stabilisation parameters: $U = +0.3$ V, $I = 0.25$ nA; logarithmic grey scale). (a) energy-dependent dI/dU data along the $[001]$ direction across a single oxygen adsorbate; the black and white dotted lines mark the positions of minima and maxima of LDOS simulated on the basis of the band structure calculation and the experimentally determined energy-dependent phase, which is sketched to the right; (b) corresponding data for the $[1\bar{1}0]$ direction.

Spin-resolved, inverse-photoemission results on a 20 ML thick bcc Fe film grown on a W(110) substrate have shown a peak located just above the Fermi-energy [64]. One-step model calculations including a realistic surface barrier with parameters given from the experiment have been able to model the experimentally observed situation and this peak has been identified as a surface resonance. The published data shows a peak close to $E = +0.15$ eV, the energy of the inflection point of the phase shift for the [001] direction in this work, but it is not clear whether there is a causal relationship. High-resolution electron energy loss spectroscopy (EELS) of oxygen adsorbed on a clean Fe(110) surface has shown a single loss around 500 cm^{-1} in the exposure range up to 6 L [63]. This corresponds to an energy of 0.06 eV and has been interpreted as the stretching vibration of atomic oxygen adsorbed at a twofold long-bridge site. This could correspond to the phase shift of the standing wave in the $[1\bar{1}0]$ direction.

Unfortunately resonances of this kind cannot be deduced from just the band structure calculation of the underlying Fe substrate. Further experimental and theoretical work is necessary to gain a more detailed understanding of the origin of the phase shift.

5.5 Conclusion

The highly anisotropic spatial variations of the LDOS in the vicinity of single oxygen impurities adsorbed on the Fe double-layer on W(110) are explained within a single-particle model. The oscillations are assigned to a scattering process at the adsorbate involving minority-spin bands of d -like character. Even though the band structure calculation does not account for adsorbate-induced modifications of the electronic structure but only models the oxygen atom as a point scatterer, excellent agreement is observed between the dispersion of the maxima and minima simulated on the basis of the band structure calculation and the experimentally determined phase, and the maxima and minima observed in the dI/dU data from full spectroscopy.

5.6 Spin-resolved measurements

If the above mentioned interpretation is correct a significant spin dependence in the electron scattering is expected to be observed by spin-polarised STS. In particular, SP-STS measurements on different types of magnetic domains with the same magnetic tip should provide information on the spin characteristics of the electronic states involved in the scattering process. As shown in Fig. 5.9 the well-known magnetic structure of 2 ML Fe/W(110), which is characterised by about 20-25 nm wide, perpendicularly magnetised domains (see Chap. 4), is unchanged by the adsorption of oxygen. Figure 5.10 gives a closer view of the oxygen adsorbates. The dI/dU map in (a) demonstrates that the characteristic patterns in the differential conductance as known from spin-averaged measurements (e.g. Fig. 5.3) can be recognised on domain A, while they are nearly absent

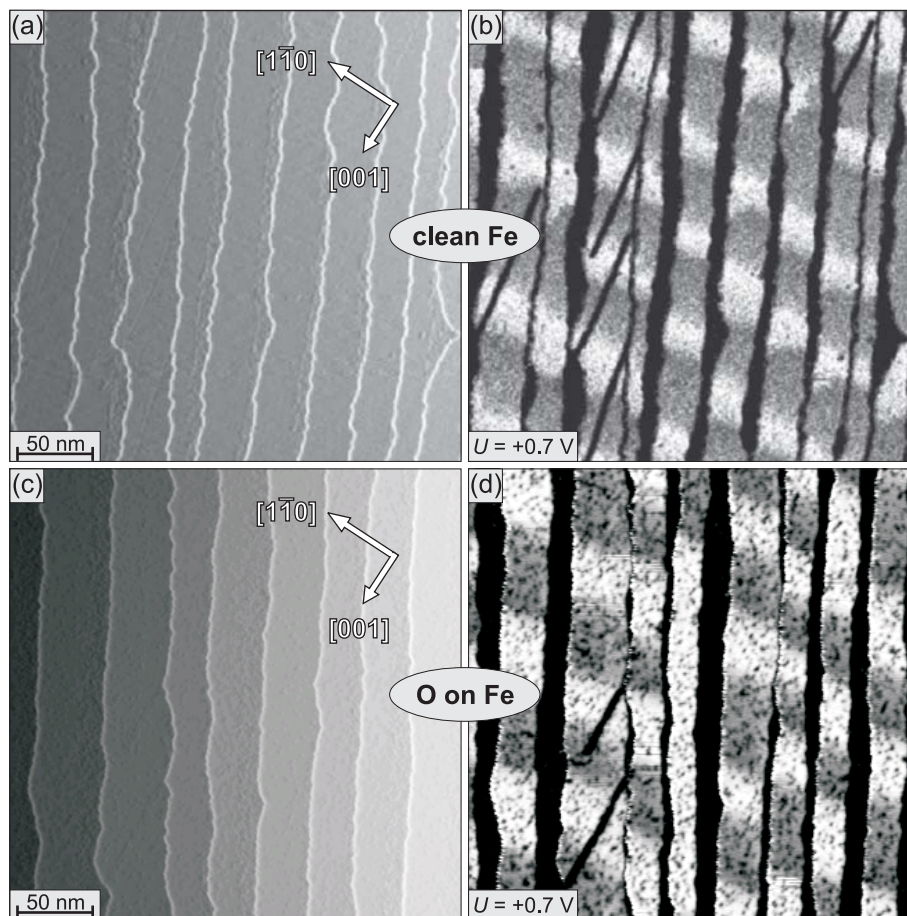


Figure 5.9: STM measurements with Gd/Fe-coated W tips. (a) topography of 1.75 ML Fe on W(110) and (b) corresponding dI/dU map [34]; (c),(d) analogue measurements after dosing 1% of a Langmuir of oxygen.

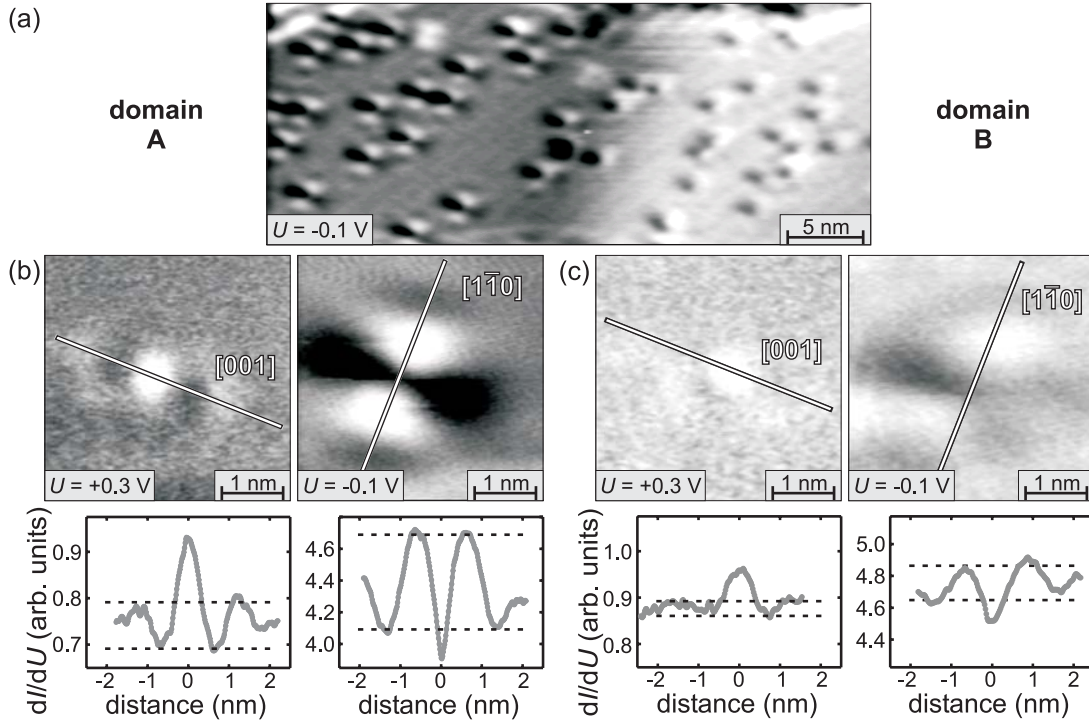


Figure 5.10: Spin-polarised STM measurements (with a Gd/Fe-coated W tip). dI/dU maps showing oxygen adsorbates on (a) two different magnetic domains A and B, with a closer view of single oxygen adsorbates (b) on domain A and (c) on domain B, the lines indicate the positions of the corresponding line profiles shown in the lower panel.

on domain B. Fig. 5.10(b) and (c) show high-resolution dI/dU maps at the labelled voltages U . Lines indicate the position of the corresponding line profiles shown in the lower panel. Around the oxygen atom on domain A the above mentioned scattering states are enhanced for both high-symmetry directions, whereas on domain B they can hardly be detected. Quantitative analysis of the dI/dU variation of these line profiles was performed by measuring the difference of the first maximum and minimum adjacent to the position of the oxygen atom (the dashed lines in the lower panel of Fig. 5.10(b) and (c)) and then dividing it by their mean value. Assuming a reading error of 0.025 arb. units the following ratios are calculated:

	domain A	domain B
[001] :	$13.5 \pm 3.4\%$	$3.1 \pm 2.8\%$
$[1\bar{1}0]$:	$14.1 \pm 0.6\%$	$4.4 \pm 0.5\%$

The factor of about 3-4 between domain A and B proves the strong spin polarisation of the standing electron waves around the impurity.

The energy-dependent oscillations in the local density of states were analysed in the same way as in Fig. 5.8. Full dI/dU spectroscopy was performed around a single oxygen atom adsorbed on one particular type of domain (A). Afterwards, the same measurement was performed around another oxygen atom on the oppositely magnetised domain (B). Finally, the measurement was repeated on the initial domain (A) to exclude the possibility of unwanted tip changes. The experimental data is presented in Fig. 5.11. The black and white lines in the plot for domain A indicate the minima and maxima simulated on the basis of the band structure calculation and the experimentally determined phase shift (cf. Fig. 5.8). Again, excellent agreement is found between the dI/dU data and the simulation of the scattering process in a simple single-particle model for domain A. Domain B on the other hand does not show the characteristic patterns in the local density of states in either of the high-symmetry direction of the surface. This proves that the observed anisotropic scattering state is highly spin-polarised and that the method of SP-STS is able to investigate standing electron waves with spin resolution.

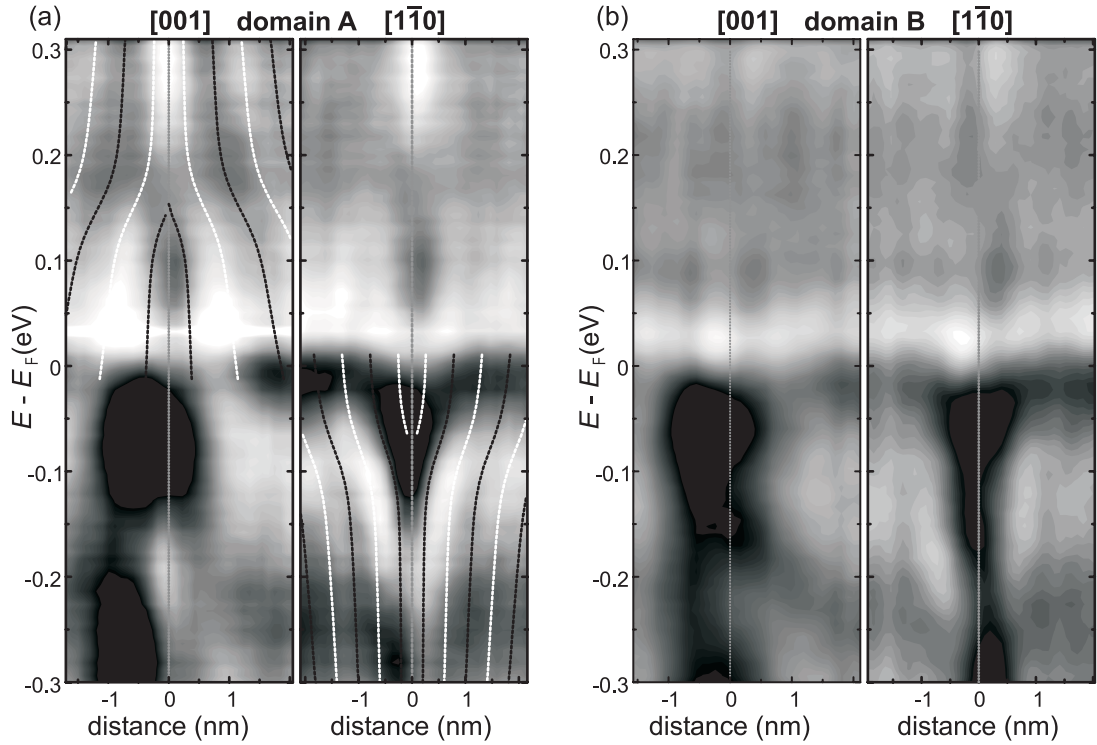


Figure 5.11: Data from spin-polarised dI/dU spectroscopy (with a Gd/Fe-coated W tip; stabilisation parameters: $U = +0.3$ V, $I = 0.25$ nA; logarithmic grey scale). (a) data for domain A along the two crystallographic axes; the black and white dotted lines indicate the minima and maxima simulated on the basis of the band structure calculation and the experimentally determined phase relation; (b) data for domain B along the two crystallographic axes.

Chapter 6

Iron on tungsten (001)

The system of highly strained pseudomorphic Fe films on W(001) has attracted much attention in the past. Conflicting results have been reported concerning the magnetic properties in the low coverage regime which have mainly been studied by spatially averaging methods [25, 69, 70, 71, 72, 73, 74, 75, 76, 77]. Since it is well-known that the morphology can have a large impact on the magnetic structure [1, 2, 7, 8, 9, 10, 11, 12, 13, 14, 15, 16] the importance of investigating the structure as well as the magnetic properties with high spatial resolution to fully understand a system is obvious. Spin-polarised scanning tunneling microscopy (SP-STM) is a powerful tool to study magnetism in reduced dimensions and correlate it directly to the topographic and electronic structure.

This chapter is dedicated to results on the system of Fe on W(001). First a survey of fully relaxed three-dimensional Fe islands is given (Sec. 6.1). Then measurements on systems in a coverage regime of co-existence of pseudomorphic and reconstructed layers are discussed. A correlation of topographic structure with electronic properties reveals a pronounced layer dependence of the differential conductance (Sec. 6.2). The focus of this chapter is put on the spin-resolved measurements investigating the magnetic structure in the pseudomorphic regime (Sec. 6.3). STM is used to overcome the discrepancy concerning the magnetic properties of thin Fe films on W(001). After a brief growth study the investigation of the domain structure with high spatial resolution is presented. Spin-resolved differential conductance measurements allow a direct observation of the fourfold anisotropy. Quantitative analysis of the intensity of the signal reveals a rotation of the easy axis in the pseudomorphic regime. While the second and third monolayer are magnetised along $\langle 110 \rangle$ directions of the surface the fourth monolayer has an easy axis along $\langle 100 \rangle$. These high-symmetry directions and therefore also the layer-dependent easy axes enclose an angle of 45° .

All STM measurements were acquired with the cryo-STM at $T = 13$ K (described in Chap. 3.2.2) and details on preparation techniques are given in Chap. 3.3. The coverage θ is always given in pseudomorphic monolayers, in this chapter referring to W(001). In the context of spatially resolved measurements θ is the local coverage.

6.1 Three-dimensional growth

It is well-known, that at elevated temperatures Fe grows on W(001) in a Stranski-Krastanov mode forming a wetting layer of 2 ML and three-dimensional islands on top [25, 41, 73]. While the amount of Fe deposited onto the W(001) surface affects the height and number of islands, the growth conditions determine the shape of the islands. A compact island shape can be prepared by evaporating Fe with the substrate held at room temperature and subsequent annealing. When the substrate is annealed during the deposition of Fe the morphology of the sample shows islands on top of the 2 ML thick wetting layer which are elongated along $\langle 100 \rangle$ directions of the surface.

6.1.1 Compact island shape

Figure 6.1(a) shows the topography of a sample of 6.4 ML of Fe deposited onto the W(001) crystal at room temperature and subsequent annealing to $T = 750$ K for $t = 5$ min. The island density is 56 ± 9 per μm^2 . The morphology of the islands is rectangular with the axis along the $\langle 100 \rangle$ directions of the surface. The ratio between the longer axis a and the shorter axis b of the islands is 1.7 ± 0.5 (see Fig. 6.1(b)). About 70% of the islands are oriented with the direction of the step edges and a enclosing a smaller angle as compared to b . The average diameter $d = (a+b)/2$ of the islands is 32 ± 11 nm and the height h is 4.2 ± 0.6 nm. Figure 6.1(b) shows a closer view of the island marked with a circle in (a). It is a comparably large island with $a = 54$ nm, $b = 42$ nm, and an average height of $h = 4.5$ nm. A height profile along the line in Fig. 6.1(b) is shown in (c). The island has some screw dislocations at the surface but no ordered reconstruction patterns. This indicates that the surface of the island is almost completely relaxed. A dI/dU spectrum measured on top of the island is shown in Fig. 6.1(d). A pronounced peak at a sample bias $U = +0.19$ V is observed which can be identified as the well-known surface state of Fe(001) surfaces which has been found in other experiments at $U = +0.17$ V [78]. The magnetic properties of these islands have been studied earlier and show single domain states for islands of this size, while larger islands form vortex structures [15, 16].

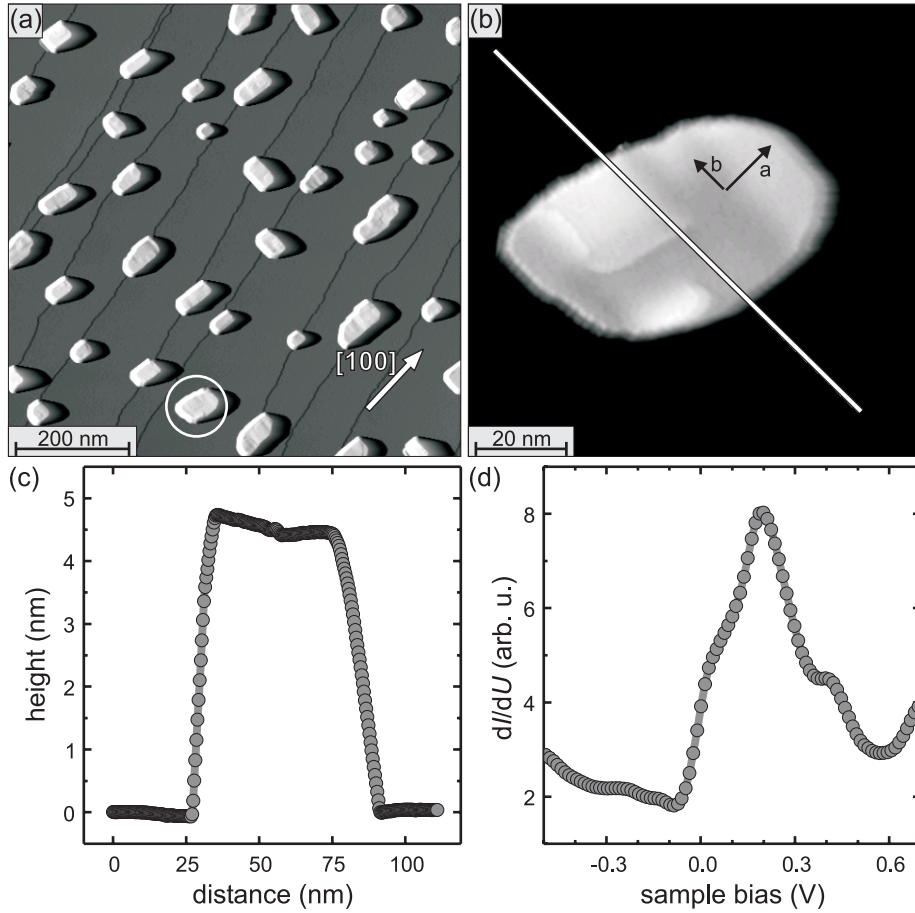


Figure 6.1: Sample of 6.4 ML of Fe on W(001) grown at room temperature with subsequent annealing to $T = 750$ K. (a) topography, the circle indicates the island shown in (b) at a closer view; (c) height profile along the line in (b); (d) dI/dU spectrum taken on top of the island shown in (b) (stabilisation parameters: $U = +1.0$ V, $I = 1.0$ nA).

6.1.2 Long island shape

Figure 6.2(a) shows the topography of a sample of 10.2 ML of Fe deposited onto the substrate held at $T = 650$ K. As also observed for the more compact islands in Fig. 6.1 the long axis is along that $\langle 100 \rangle$ direction which encloses the smaller angle with the step edges. The width of these long islands is 37 ± 11 nm and their height is 2.9 ± 0.3 nm. A closer view of the topography, a height profile across an island and a corresponding dI/dU map at $U = +0.2$ V is shown in Fig. 6.2(b), (c) and (d), respectively. Again no ordered reconstruction on top of the islands is observed, but a lot of dislocations are present. The dI/dU spectra of the long islands (not shown) are very similar to the one shown in Fig. 6.1(c) but show small variations in intensity and position of the surface state. A variation of the substrate temperature during Fe deposition has a strong effect on the island height.

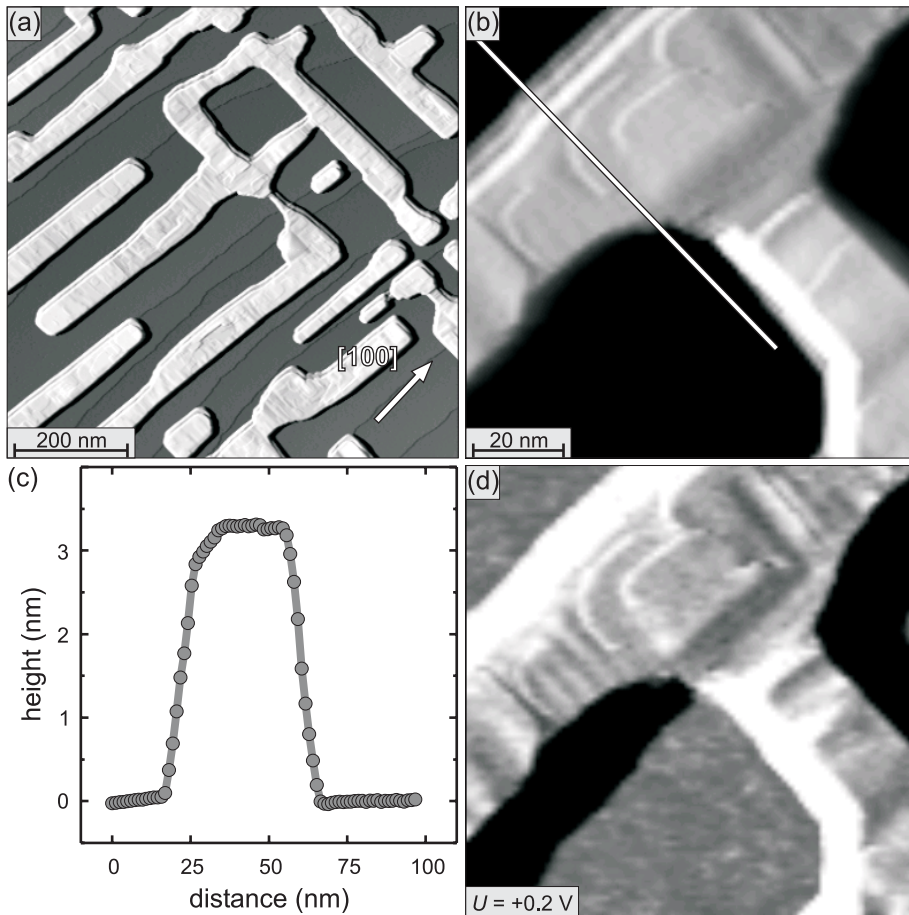


Figure 6.2: Sample of 10.2 ML of Fe on W(001) grown at $T = 650$ K. (a),(b) topography; (c) height profile along the line in (b); (d) dI/dU map corresponding to (b).

When depositing $\theta = 10$ ML of Fe, islands with $h \approx 1.5$ nm can be prepared at a substrate temperature of 600 K, islands with $h \approx 3$ nm at 650 K (see Fig. 6.2) and islands with $h \approx 9$ nm at 750 K. Reduction of the coverage mainly influences the island density but hardly affects the height of the islands. The magnetic properties of these elongated Fe islands have been studied earlier [25]. They are magnetised in the direction of their long axis and show interesting domain wall patterns at intersections.

6.2 Beginning of strain relief

Preparation of a sample of Fe on W(001) with moderate annealing of the substrate during deposition of Fe leads to a morphology with different local coverage in the regime of a few monolayers. For $\theta \geq 2$ ML a pseudomorphic wetting layer of 2 ML

is always observed. The 3rd and 4th ML also grow pseudomorphically but not in a strict layer by layer growth mode. Beginning with the 5th ML strain is relieved by incorporation of dislocation lines along $\langle 100 \rangle$. They form a regular pattern which is identified to be a (9×1) superstructure [77].

6.2.1 Topography

Figure 6.3(a) shows the topography of 5.1 ML of Fe deposited onto the sample held at $T = 550$ K. The elongated islands along the $\langle 100 \rangle$ directions of the surface are of local coverage ≥ 5 ML. As shown below they exhibit dislocation lines along

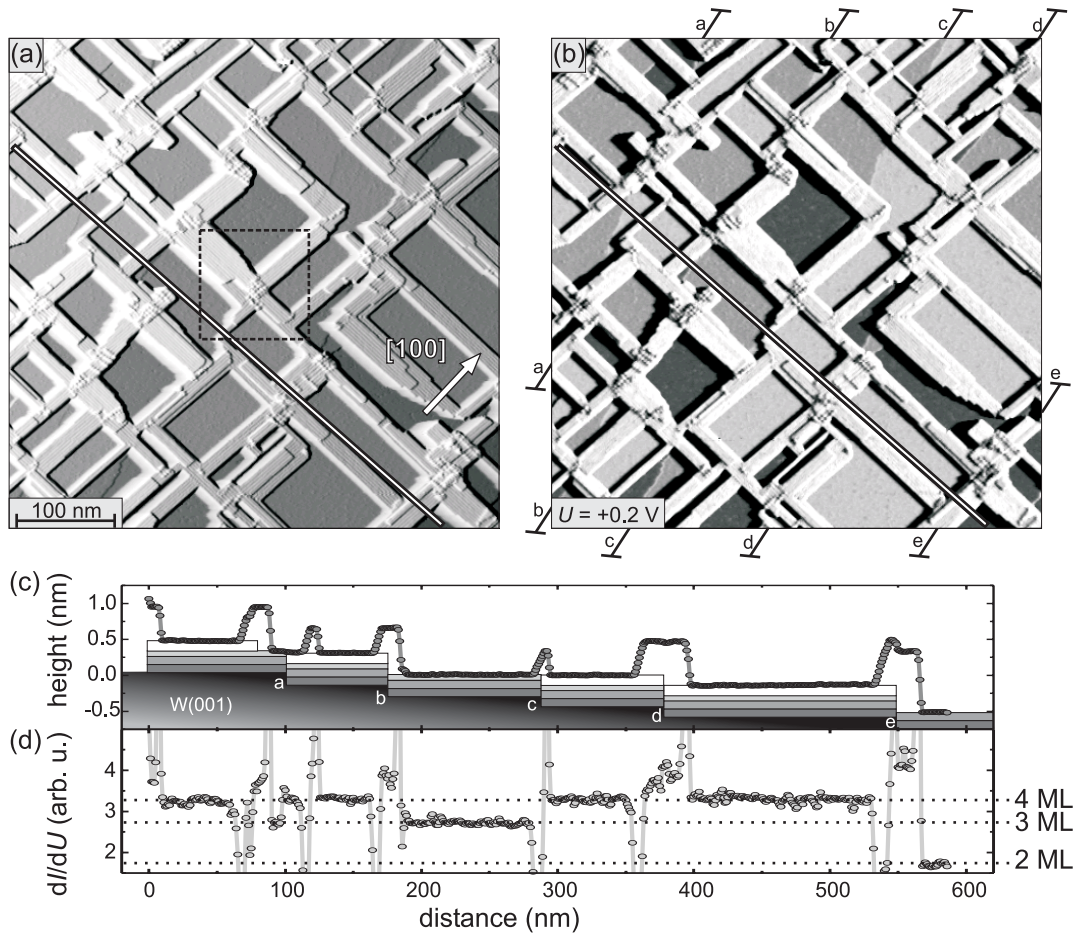


Figure 6.3: Sample of 5.1 ML of Fe on W(001) grown at $T = 550$ K. (a) topography, the dashed rectangle marks the image area investigated more closely in Fig. 6.4; (b) corresponding dI/dU map, the marks a-e indicate steps of the underlying W(001) substrate; (c) height profile along the line in (a) with a sketch of the local coverage; (d) corresponding dI/dU signal along the line in (b) with dotted lines indicating the signal strength for the different local coverage.

the long axis of the islands. While the topography image of Fig. 6.3(a) only allows discrimination between reconstructed and pseudomorphic areas, the dI/dU map at $U = +0.2\text{ V}$ shown in Fig. 6.3(b) makes it possible to distinguish between different local coverage. Besides the fact that at this voltage the dI/dU signal is generally larger on reconstructed islands compared to the signal on pseudomorphic areas, three different contrast levels can be identified in the latter case. This leads to the conclusion that different dI/dU signals correspond to different local coverage, in this case to the 2nd, 3rd and 4th ML. Closed areas which show two different contrast levels are constituted of areas with two different local coverage separated by a tungsten step underneath the surface. The positions of these buried substrate step edges are indicated with letters a-e in Fig. 6.3(b). The information gained from the topographic image together with the dI/dU map lead to an assignment of local coverage as demonstrated for the line profiles in Fig. 6.3(c) and (d). The plots are taken at the position of the lines in (a) and (b) respectively. The three different dI/dU contrast levels in the pseudomorphic growth regime can be identified as follows: the darkest one corresponds to a local coverage of 2 ML, the medium one to 3 ML while the brightest contrast level can be assigned to 4 ML. The local coverage along the height profile is schematically illustrated in Fig. 6.3(c). The sample surface is composed of approximately 10% of 2nd ML, 15% of 3rd ML, 25% of 4th ML and 40% of $\theta \geq 5$ ML.

After identification of the different pseudomorphic coverage regimes the apparent height of the layers was investigated. The topography in Fig. 6.4(a) shows a section of the surface indicated by the dashed rectangle in Fig. 6.3(a). The dashed line marks a buried mono-atomic step of the tungsten substrate from an upper terrace (left) to a lower terrace (right). Again one can easily discriminate unequal local coverage due to different electronic structure of the layers in the dI/dU map at $U = +0.9\text{ V}$ in Fig. 6.4(b). The local coverage is indicated in Fig. 6.4(a) with 2, 3, and 4 ML for the pseudomorphic regime and A, B and C for the reconstructed areas. Figure 6.4(c) displays a model of the (9×1) reconstruction which is formed for $\theta \geq 5$ ML assuming that one additional atom is incorporated per dislocation line. The histograms of Fig. 6.4(d) show the measured height distribution on the two terraces of the W substrate of Fig. 6.4(a). The darker line is a histogram of the left terrace, with the dominating local coverage of 2 ML, 3 ML and coverage C. The brighter line in Fig. 6.4(d) corresponds to the right tungsten terrace of Fig. 6.4(a) with a local coverage of 4 ML, A, B and C. In order to compensate the height of the mono-atomic step of the tungsten substrate the height-axes of the two lines are shifted by 1.6 \AA with respect to each other. Sharp peaks are observed which are assigned to a local coverage of 2, 3 and 4 ML and broader ones for coverage labelled A, B and C with the splitting due to protrusions and depressions of the reconstruction. The height difference between adjacent peaks is given in \AA . The bulk lattice constant for bcc W is $a_W = 3.165\text{ \AA}$ and for

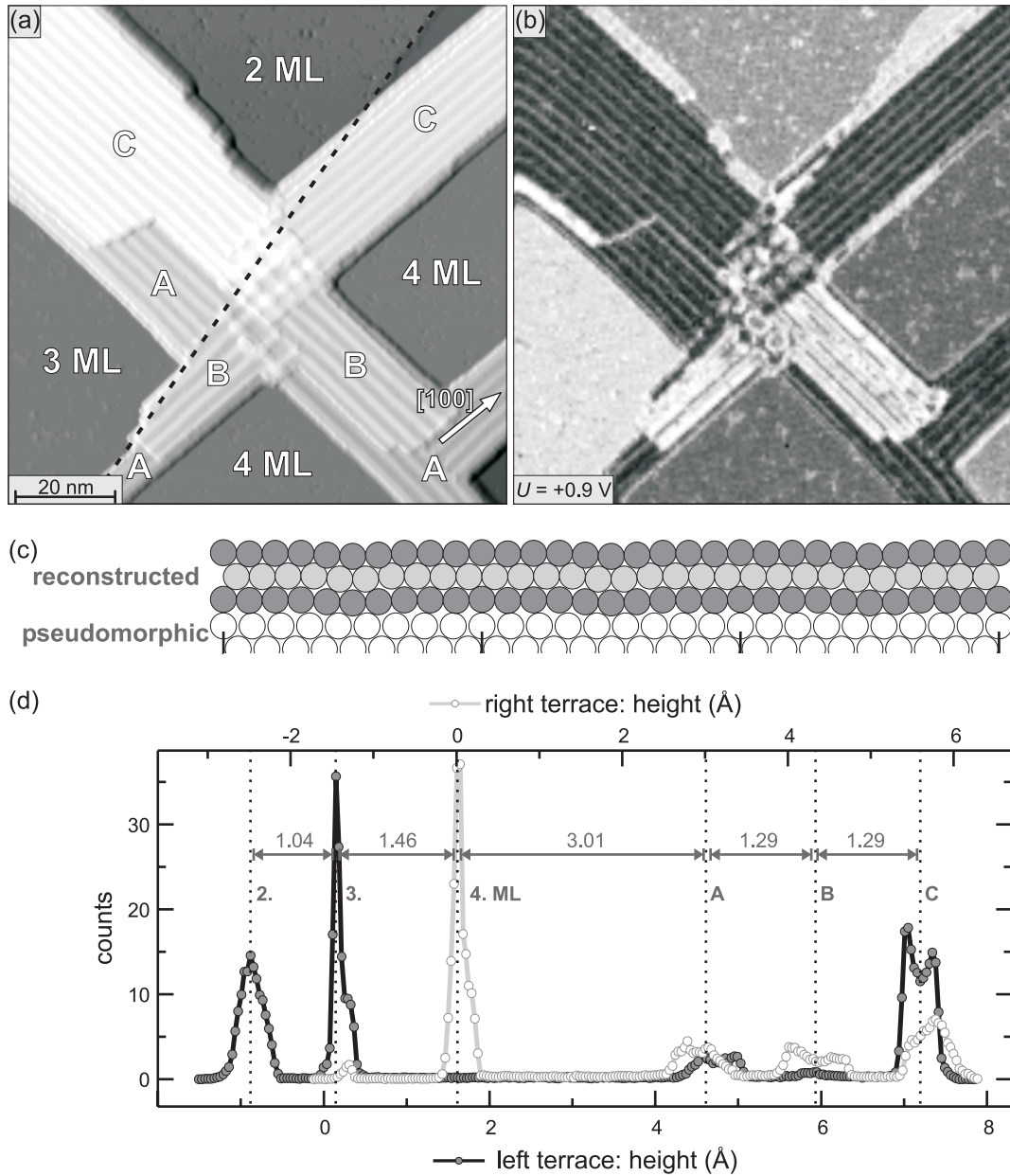


Figure 6.4: Sample of 5.1 ML of Fe on W(001) grown at $T = 550$ K. (a) topography at $U = +1.0$ V, dashed line indicates a step of the tungsten substrate, labels refer to the local coverage; (b) corresponding dI/dU map taken from full spectroscopy (stabilisation parameters: $U = +1.0$ V, $I = 1.0$ nA); (c) model of the (9×1) reconstruction cut along the $[100]$ direction perpendicular to the dislocation lines; (d) histogram of left/upper and right/lower terrace of (a), shifted by 1.6 \AA with respect to each other.

Fe it is $a_{\text{Fe}} = 2.8665 \text{ \AA}$ [37]. Considering a bcc (001) surface one expects the height of an ideal mono-atomic W step to be $h_{\text{W}} = 1.583 \text{ \AA}$ and for Fe $h_{\text{Fe}} = 1.433 \text{ \AA}$. A large variation of the apparent height is observed in the low coverage regime which suggests different electronic properties of the layers. The large height difference of $h = 3.01 \text{ \AA}$ between the 4th ML and layer A could correspond to one additional layer, two layers or even three monolayers (with a height of $h = 1 \text{ \AA}$ each). In order to evaluate which assumption is the most probable the consequence of the formation of the reconstruction and the height of reconstructed areas is discussed. In this context it is assumed that the volume per atom does not change from fully relaxed to strained structures. With the bulk lattice constant of $a_{\text{Fe}} = 2.8665 \text{ \AA}$ for the unit cell with two atoms, the volume per Fe atom is $V_{\text{Fe-atom}} = 11.777 \text{ \AA}^3$. In the pseudomorphic regime of Fe on tungsten (001) the area per atom is $A_{\text{ps}} = 10.017 \text{ \AA}^2$. This leads to a height of $h_{\text{ps}} = 1.176 \text{ \AA}$ when the volume per atom is constant. In the reconstructed areas the strain is relieved in one $\langle 100 \rangle$ direction. The area per atom then is $A_{\text{rc}} = 3.165 \text{ \AA} \times 2.849 \text{ \AA} = 9.017 \text{ \AA}^2$ which results in a height of $h_{\text{rc}} = 1.306 \text{ \AA}$. The height of the 3rd and 4th ML as well as that of layers B and C are in reasonable agreement with this model. The height of 4 pseudomorphic monolayers of Fe on tungsten (001) in this simple model is $4 \times h_{\text{ps}} = 4.704 \text{ \AA}$. Considering the measured value of 3.01 \AA between 4th ML and layer A, calculation of the height of layer A referred to the tungsten surface results in $h_{\text{A}} = 7.714 \text{ \AA}$. It is assumed that layers which are pseudomorphic in the low coverage regime also relax and form the reconstruction to some extent once they are covered with patches of $\theta \geq 5 \text{ ML}$ [25]. In the simple model discussed here the height of layer A can be reproduced best when A is the 6th ML. Assuming one pseudomorphic layer and five reconstructed layers a height of $h_{\text{A}} = 1 \times h_{\text{ps}} + 5 \times h_{\text{rc}} = 7.706 \text{ \AA}$ is calculated. Even though an intermediate height is not observed the conclusion that layer A is the 6th ML and B and C one additional layer each seems to be the most probable. However, this cannot be directly proven with the STM technique, so the areas are simply labelled A, B and C in the following.

6.2.2 Electronic structure

To investigate the electronic structure of the different local coverage regimes in more detail spatially resolved full dI/dU spectroscopy measurements were performed in the sample area shown in Fig. 6.4(a) and (b). Figure 6.5(a) shows layer-resolved dI/dU spectroscopy data measured with stabilisation parameters $U = +1.0 \text{ V}$, and $I = 1.0 \text{ nA}$. Even though each layer has a dominating spectral feature in the unoccupied states of the sample and is rather featureless in the occupied states, the fine structure of the layers proves to be quite layer-dependent. The major peak for the pseudomorphic layers is observed at significantly different energies:

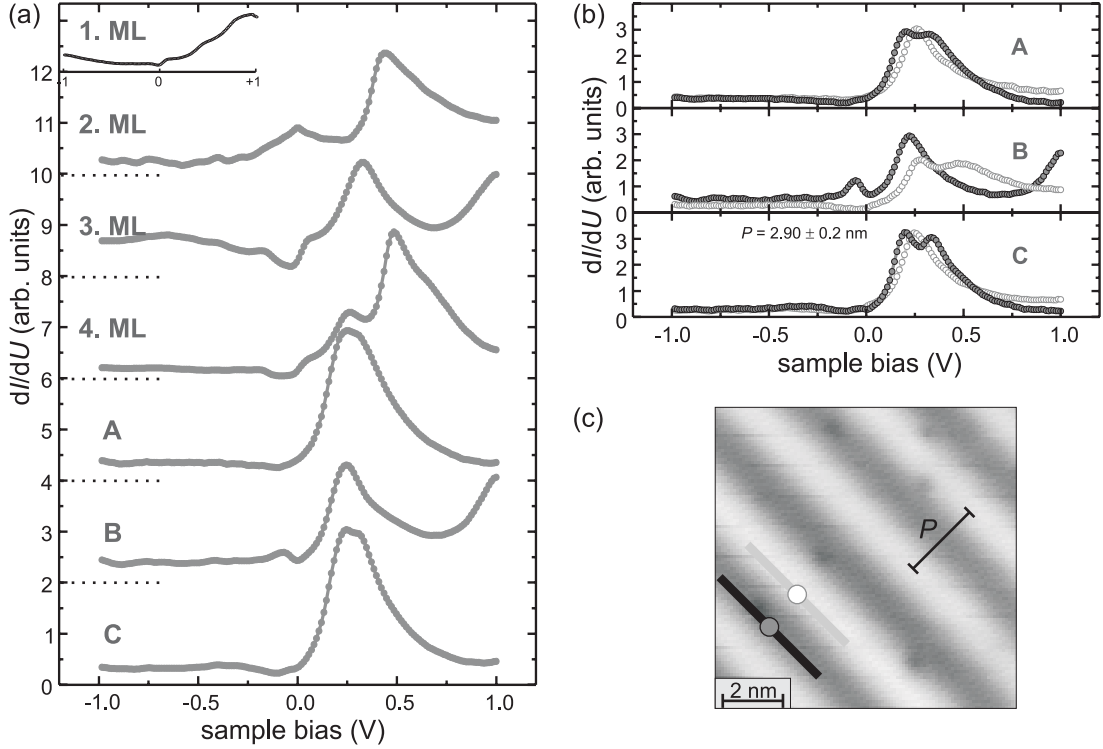


Figure 6.5: Data from measurements of a sample of 5.1 ML of Fe on W(001) grown at $T = 550$ K (cf. Fig. 6.4). (a) layer-resolved dI/dU spectra shifted by $dI/dU = 2$ arb. units for clarity (stabilisation parameters: $U = +1.0$ V, $I = 1.0$ nA), labels refer to the local coverage (cf. Fig. 6.4(a)), inset: dI/dU spectrum of the 1st ML from a different measurement; (b) dI/dU spectra taken on protrusions and depressions of the reconstructed areas, the positions of the spectra are marked in the topography image (c) of an area with local coverage C; P indicates the period of the reconstruction.

at $U = +0.44$ V for 2 ML,
 at $U = +0.33$ V for 3 ML,
 at $U = +0.49$ V for 4 ML.

Theoretical calculations are necessary to reveal the cause and nature of the features in the dI/dU spectra.

The spectra of the reconstructed layers A and C show basically one peak and are very similar. Surprisingly the layer in between, labelled as B, differs significantly. This becomes even more clear in Fig. 6.4(b) where the spectra are resolved to show the electronic structure on the protrusions and in the depressions of the reconstructed areas. A topography image is shown in (c). The period of the reconstruction is $P = 2.9 \pm 0.2$ nm. Both, region A and C, show one peak in the dI/dU spectra at $U = +0.26$ V and $+0.25$ V respectively, on the protrusions

of the reconstruction and two peaks at $U = +0.20$ V and $U = +0.34$ V for the depressions. Region B shows quite different spectral features with one major peak at $U = +0.28$ V and a second one at $U = +0.50$ V on the protrusions. In the depressions one dominating peak in the unoccupied states at $U = +0.22$ V and an additional peak in the occupied states at $U = -0.05$ V of the sample is observed.

For a more detailed understanding of the impact of the reconstruction on the electronic structure theoretical calculations are necessary. The magnetic properties of samples similar to the one shown in Fig. 6.5 have been investigated previously with magneto-optical Kerr effect (MOKE) measurements [77]. It has been proposed that they exhibit a fourfold anisotropy with easy directions along $\langle 110 \rangle$ up to the onset of dislocation formation.

6.3 Pseudomorphic Regime

The system of Fe on W(001) shows pseudomorphic growth when the local coverage is ≤ 4 ML. Again the temperature of the substrate during deposition determines the growth mode. The magnetic properties in the pseudomorphic regime have been studied with various techniques. No magnetisation has been found in the monolayer [73, 76, 77] but calculations have predicted an antiferromagnetic ground state [79]. There have been contrary statements about the easy axis of the magnetisation for the pseudomorphic layers. Surface magneto-optical Kerr effect measurements have shown an easy axis along $\langle 110 \rangle$ for 1.5 ML of Fe on W(001) [71] but measurements with spin-polarised low energy electron diffraction (SPLEED) of up to 5 ML have been interpreted in terms of an easy axis along $\langle 100 \rangle$ even though it has been pointed out that a magnetic easy axis along $\langle 110 \rangle$ is also possible [74]. Referring to the SPLEED measurements it has been assumed that the magnetisation is along $\langle 100 \rangle$ [73, 76] until MOKE measurements have provided evidence for an easy direction along $\langle 110 \rangle$ for moderately annealed pseudomorphic films up to the onset of dislocation formation [77]. In the following the magnetism in the pseudomorphic regime of Fe on W(001) is investigated with high spatial resolution using the method of SP-STM (see Chap. 2.5).

6.3.1 Topography

Figure 6.6 shows the topography of samples prepared under different growth conditions. In all cases the W(001) is covered with a 2 ML thick wetting layer. After deposition of 2 ML of Fe onto a sample held at moderate temperature ($T = 525$ K) islands in the 3rd ML start to nucleate as shown in Fig. 6.6(a). On increasing the coverage islands of the 3rd ML grow and coalesce, but the 3rd ML remains incomplete. As can be seen in Fig. 6.6(b) 4th ML islands start to form before the layer underneath is closed. The edges of the small islands of the 3rd ML (a) as well as the

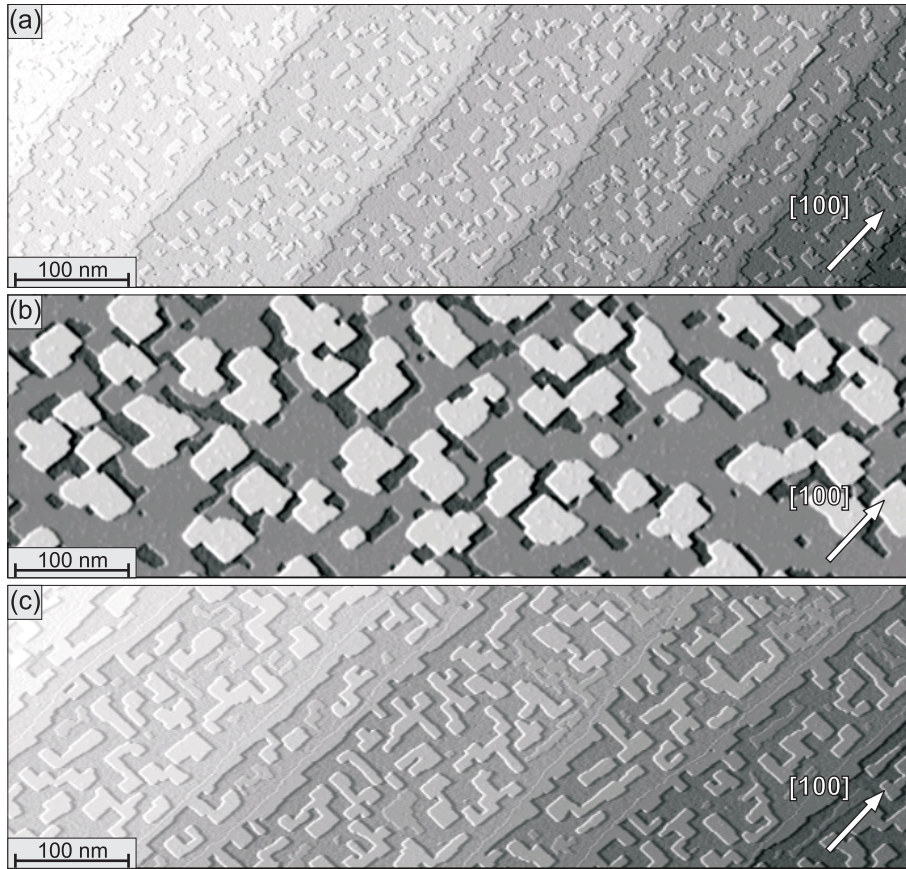


Figure 6.6: Topography of Fe on W(001) in the pseudomorphic regime prepared under different growth conditions. (a) 2.2 ML Fe on W(001) grown at $T = 525$ K; (b) 3.2 ML Fe on W(001) grown at $T = 525$ K; (c) 3.0 ML Fe on W(001) grown at $T = 550$ K.

larger patches (b) are preferentially oriented along $\langle 100 \rangle$ directions. The 4th ML islands on top are of compact shape and also have edges along $\langle 100 \rangle$. At this temperature the inter-layer mass transport is hindered and the proportions of the different layers can be quantitatively understood considering that once patches of the 3rd ML have been formed additional Fe is distributed onto the 2nd and 3rd ML according to the percentage of their respective areas. When the temperature of the W(001) substrate is increased slightly ($T = 550$ K) during deposition, the growth mode changes dramatically as shown in Fig. 6.6(c). Only very few areas with a local coverage of 3 ML are observed and they are of irregular shape. Islands of the 4th ML again have edges preferentially oriented along the $\langle 100 \rangle$ directions but are of elongated shape, in contrast to the compact islands observed before (b). Obviously, the 3rd ML is thermodynamically unstable. When the temperature of the substrate is increased during growth, the mobility of the atoms is high enough to allow inter-layer mass transport and a thermodynamically more

stable arrangement is formed, consisting mainly of local coverage of 2 and 4 ML. The elongated shape of the 4th ML islands can be explained by a partial strain release in the direction of the narrow axis of the island, which is only energetically favourable until a maximum width is reached. Even though no reconstruction is visible the atoms at the edges of the islands can move inwards slightly and thus reduce stress.

6.3.2 Magnetism: wetting layer and 4th ML islands

The magnetic properties of a sample with 4th ML islands on top of the 2 ML wetting layer were investigated using spin-polarised STM. Figure 6.7 shows data acquired with a Fe-coated tungsten tip which is sensitive to the in-plane component of the sample magnetisation (see Chap. 3.3.2). The topography (a) shows a sample of 3.0 ML Fe/W(001) (see Fig. 6.6(c)). The corresponding dI/dU map in Fig. 6.7(b) is measured at a bias voltage of $U = -0.8$ V and shows a strong magnetic contrast for the 2nd ML. For clarity the areas of the 3rd and 4th ML have been put to a uniform medium grey. One can distinguish four different contrast levels on the 2nd ML denoted with small roman numbers (i - iv) starting with the highest intensity. Analysis of the strength of the different dI/dU signals of Fig. 6.7(b) (smoothed data) results in the following in arbitrary units (a.u.):

$$\begin{aligned} (dI/dU)_i &= 2.26 \pm 0.08 \text{ a.u.} \\ (dI/dU)_{ii} &= 1.92 \pm 0.08 \text{ a.u.} \\ (dI/dU)_{iii} &= 1.74 \pm 0.09 \text{ a.u.} \\ (dI/dU)_{iv} &= 1.40 \pm 0.13 \text{ a.u.} \end{aligned}$$

Considering the fourfold symmetry of the (001) surface opposite magnetisation is assumed for domains i and iv and for domains ii and iii , respectively. Calculation of the amplitudes A of the dI/dU signal of oppositely magnetised domains results in

$$\begin{aligned} A_{i-iv} &= 0.86 \pm 0.15 \text{ a.u.} \\ A_{ii-iii} &= 0.18 \pm 0.12 \text{ a.u.} \end{aligned}$$

and on the basis of Eq. 2.20 the relative orientation between tip magnetisation \vec{M}_t and sample magnetisation \vec{M}_s can be described by

$$\tan \alpha = \frac{A_{ii-iii}}{A_{i-iv}}. \quad (6.1)$$

α denotes the angle between \vec{M}_t and \vec{M}_s , in this case of domain i . One derives

$$\alpha_{2\text{ML}} = 11.8 \pm 7.9^\circ.$$

This result is schematically drawn in Fig. 6.7(d) with \vec{M}_t vertically and \vec{M}_s indicated by the arrows. The shaded regions mark the uncertainty. Although an

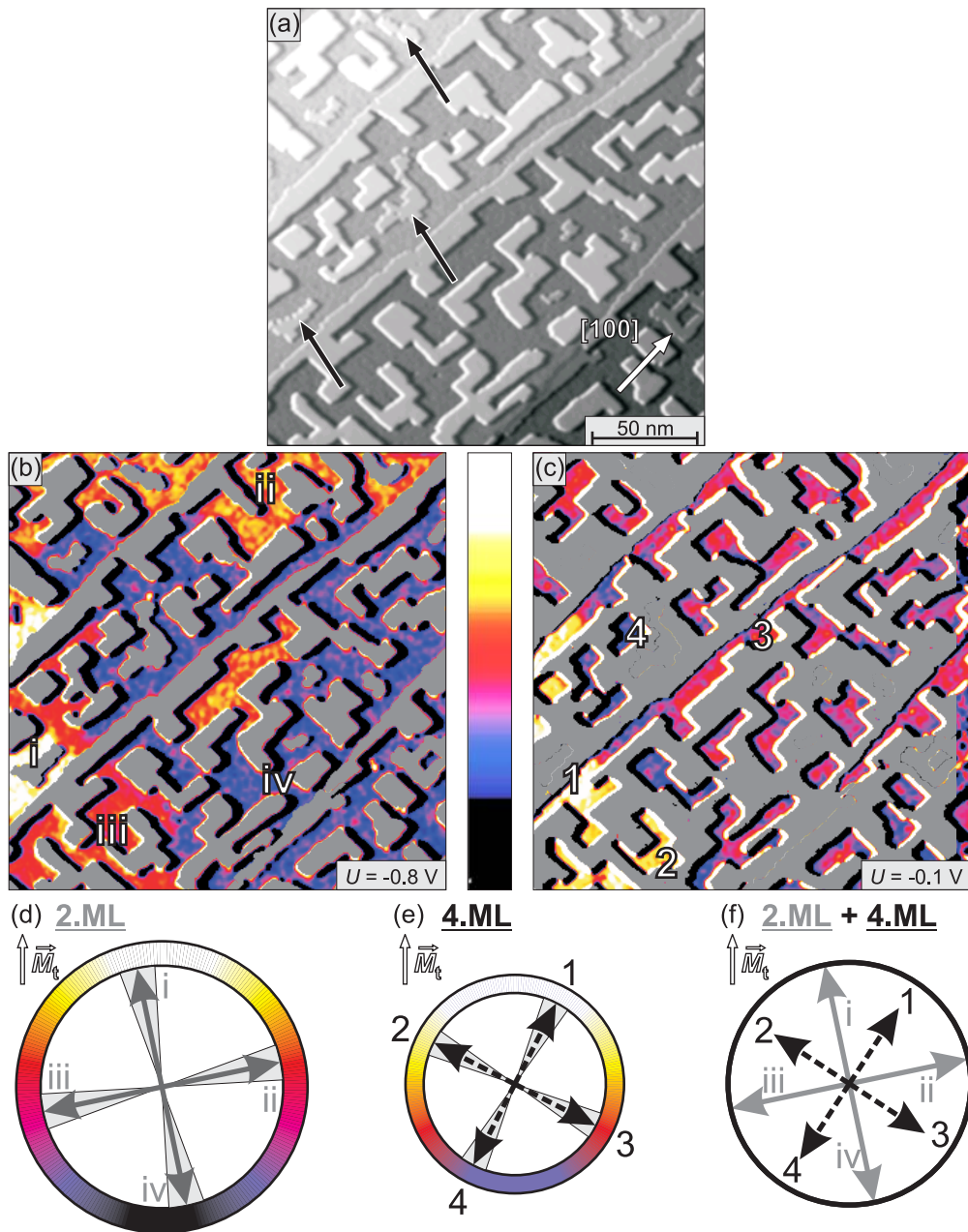


Figure 6.7: Sample of 3.0 ML of Fe on W(001) grown at $T = 550$ K and measured with a Fe-coated W tip. (a) topography (arrows indicate 3rd ML islands which will be referred to in Sec. 6.3.3); (b) corresponding dI/dU map, colour scale: 2nd ML, uniform grey: 3rd, 4th ML; (c) corresponding dI/dU map, colour scale: 4th ML, uniform grey: 2nd, 3rd ML; (d) magnetisation of the 2nd ML with respect to the tip magnetisation; (e) magnetisation of the 4th ML with respect to the tip magnetisation; (f) sketch of the 45° rotation between 2nd and 4th ML magnetisation.

opposite sense of rotation would also be consistent with this data, \vec{M}_i is rotated arbitrarily anticlockwise by $\alpha_{2\text{ML}}$.

Figure 6.7(c) shows the same section of the surface at a different voltage measured simultaneously to (b) (forward and backward scan). At this voltage the 4th ML shows a strong magnetic contrast. The other layers are put to a uniform medium grey for better visibility. Again four different magnetic domains can be distinguished as indicated with arabic numbers (1-4) from highest to lowest intensity. Comparing the domain structure of the 2nd ML (see Fig. 6.7(b)) with that of the 4th ML (c) no direct correlation is found. Quantitative analysis of the dI/dU signal of the 4th ML in the same way as described for the 2nd ML results in:

$$\begin{aligned} (dI/dU)_1 &= 7.61 \pm 0.14 \text{ a.u.} \\ (dI/dU)_2 &= 7.29 \pm 0.16 \text{ a.u.} \\ (dI/dU)_3 &= 6.62 \pm 0.12 \text{ a.u.} \\ (dI/dU)_4 &= 6.30 \pm 0.12 \text{ a.u.} \end{aligned}$$

$$\text{and an angle of } \alpha_{4\text{ML}} = 27.1 \pm 7.7^\circ$$

between the magnetisation of the tip and the magnetisation of domain 1 on the 4th ML as schematically sketched in Fig. 6.7(e). Here the arrow for \vec{M}_1 is arbitrarily turned clockwise by $\alpha_{4\text{ML}}$. Calculating the angle between 2nd and 4th ML magnetisation for the two possible rotation directions of $\alpha_{2\text{ML}}$ and $\alpha_{4\text{ML}}$ ($\pm 11.8^\circ$ and $\pm 27.1^\circ$) one obtains angles of $15.3 \pm 11.0^\circ$ and $38.9 \pm 11.0^\circ$. Since a bcc (001) surface is considered, the only possible high-symmetry axes are $\langle 100 \rangle$ and $\langle 110 \rangle$. Therefore, the magnetisation vectors of the 2nd and 4th ML must either be collinear or include an angle of 45° . Since a collinear arrangement is not within the error it is concluded that a rotation of 45° is realised here.

To directly investigate the correlation between the magnetisation of the 2nd ML with that of the 4th ML the spatially resolved data of Fig. 6.7(b) and (c) are compared. 4th ML islands with \vec{M}_4 are observed both on patches with \vec{M}_{iii} and \vec{M}_{iv} . Also 4th ML islands with \vec{M}_3 are present on two different domains of the 2nd ML, namely \vec{M}_{ii} and \vec{M}_{iv} . Islands with \vec{M}_2 are found on 2nd ML patches with \vec{M}_i (not shown here) and \vec{M}_{iii} , while \vec{M}_1 is observed on \vec{M}_i only. This indicates that the magnetisation axes of the 4th ML lie between those of the 2nd ML. This leads to the conclusion that a rotation of 45° between the magnetisation axes of 2 ML and 4 ML is present, as already proposed after analysing the angles calculated from the dI/dU intensities. This result is sketched in Fig. 6.7(f).

Figure 6.8(a) shows a dI/dU map of again 3.0 ML Fe/W(001) at a larger scale measured with a spin-polarised tip. Here the different magnetisation axes of 2nd and 4th ML can be studied within the same image. Two different signal strengths of the 2nd ML are observed, denoted by i and ii . Three different contrast levels

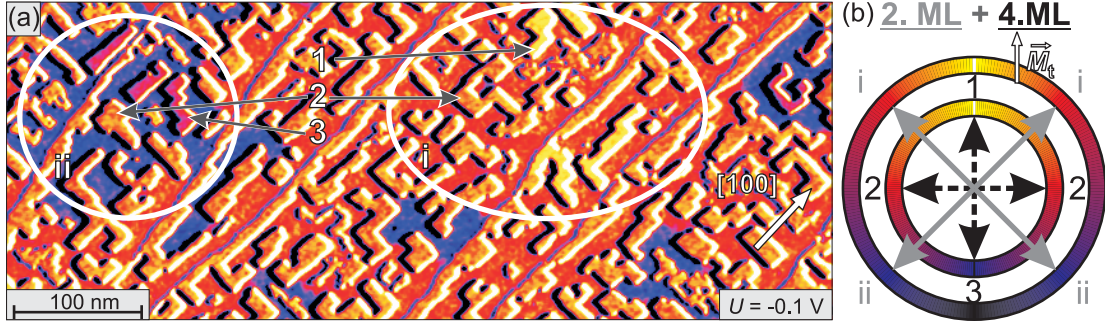


Figure 6.8: Sample of 3.0 ML of Fe on W(001) grown at $T = 550$ K and measured with a Fe-coated W tip. (a) dI/dU map; (b) sketch of the 45° rotation between 2nd and 4th ML magnetisation.

(1-3) are found for the 4th ML. There are no more contrast levels in the whole area of the surface studied with this spin-polarised tip. Again four equivalent magnetisation directions can be assumed in each layer and the dI/dU contrasts of this measurement can be explained with an angle of 45° between \vec{M}_t and \vec{M}_i and an angle of 0° between \vec{M}_t and \vec{M}_1 as sketched in Fig. 6.8(b). Again two types of 4th ML islands can be found on each of the 2nd ML patches. This is indicated in Fig. 6.8(a): islands with \vec{M}_1 and \vec{M}_2 on a patch with \vec{M}_i and islands with \vec{M}_2 and \vec{M}_3 on a patch with \vec{M}_{ii} . Discrimination between the two domains of the 4th ML which both have an angle of 90° to the tip magnetisation \vec{M}_t is not possible, thus both are denoted with 2. Also the two domains of the 2nd ML with an angle of $\pm 45^\circ$ show the same strength of the dI/dU signal, the same holds for the two domains with $\alpha = \pm 135^\circ$.

Figure 6.9(a) and (b) show the topography and the corresponding dI/dU map of 3.0 ML Fe/W(001) measured with a Fe-coated tip. In this case three different signal strengths of the 2nd ML (*i-iii*) but only two nuances of the 4th ML (1,2) are detected in the dI/dU map (b). The explanation of these results is analogue to the one for the previous measurement shown in Fig. 6.8 and the resulting magnetisation axes with respect to \vec{M}_t are sketched in Fig. 6.9(f). Compared to Fig. 6.8(b) the magnetisation of the tip used in this measurement is rotated by 45° . To investigate the spin polarisation of the 2nd and 4th ML in more detail, spatially resolved full dI/dU spectroscopy (stabilisation parameters: $U = +1.0$ V, $I = 1$ nA) was performed in the area indicated by the dashed rectangle in Fig. 6.9(b). The spin-resolved spectra for 2nd and 4th ML are shown in the upper panels of (c) and (d), the asymmetries are plotted in the lower panels. A spectrum of the 3rd ML island in the image area is shown in (e). The spectra of the 2nd ML (c) show that \vec{M}_{ii} is the intermediate of \vec{M}_i and \vec{M}_{iii} . The two peaks observed for the 2nd ML are both highly spin-polarised but with opposite sign. An asymmetry of +14% is

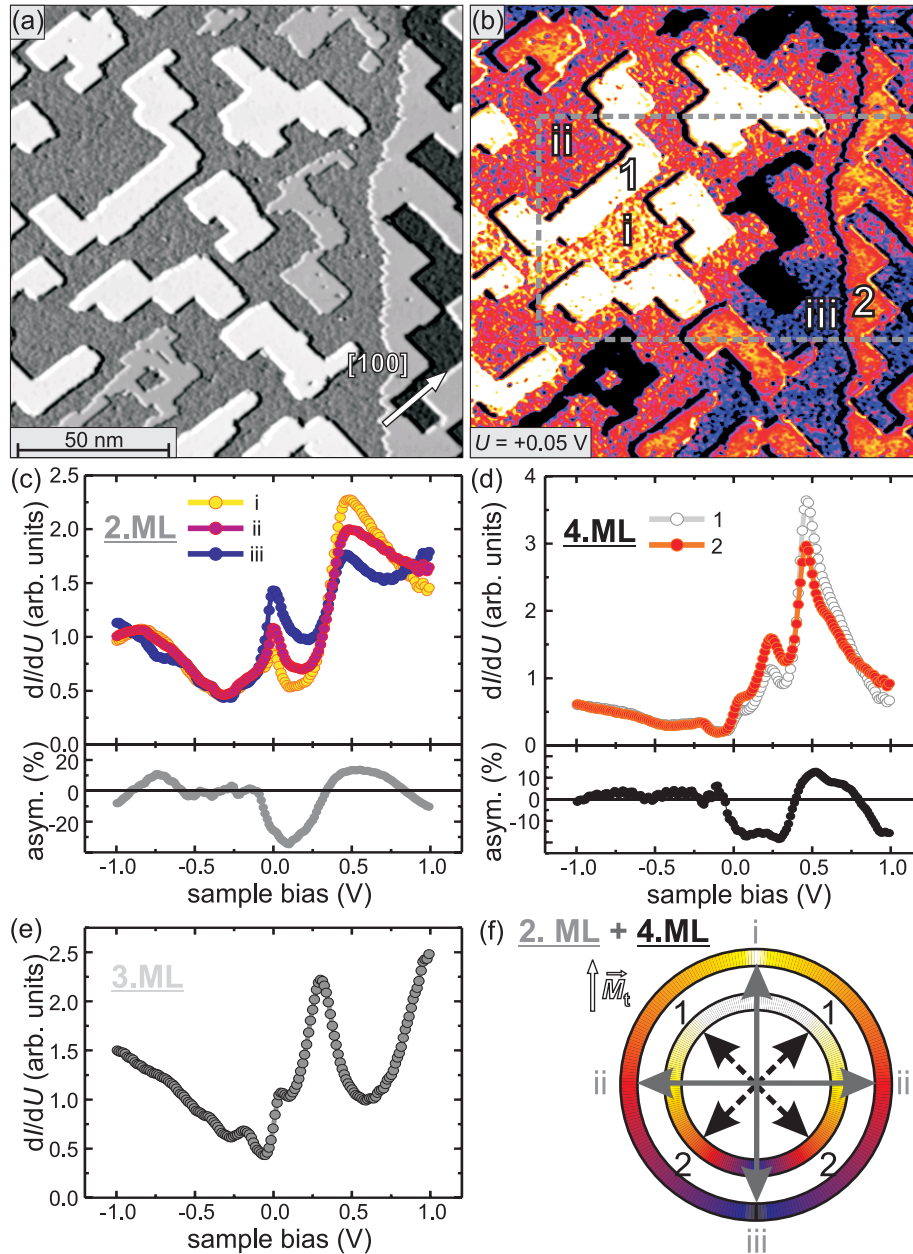


Figure 6.9: Sample of 3.0 ML of Fe on W(001) grown at $T = 550$ K and measured with a Fe-coated W tip. (a) topography; (b) corresponding dI/dU map; (c) dI/dU spectra of different magnetic domains (*i*, *ii*, *iii*) of the 2nd ML and asymmetry (*i*, *iii*); (d) dI/dU spectra of different magnetic domains (1, 2) of the 4th ML and asymmetry; (e) dI/dU spectra of the 3rd ML; (f) sketch of the 45° rotation between 2nd and 4th ML magnetisation.

observed for the peak at $U = +0.47$ V and one of -35% for the one at the Fermi energy $U = \pm 0.00$ V. Figure 6.9(d) shows three peaks for the 4th ML, the one at $U = +0.46$ V with an asymmetry of $+13\%$, the other ones have opposite spin polarisation: $U = +0.24$ V with an asymmetry of -18% , $U = +0.03$ V with an asymmetry of -16% . The 3rd ML shows spectral features at $U = +0.30$ V, $+0.05$ V and -0.18 V (e). In order to specify the character or cause of the different spectral features and to explain the different electronic structure of the pseudomorphic layers or the energy-dependent asymmetry, spin-resolved electronic structure calculations have to be performed for this system.

6.3.3 Magnetism: 3rd ML and 4th ML islands

To investigate the magnetic anisotropy of the 3rd ML a sample with growth conditions as described for Fig. 6.6(b) was prepared. A topography and a corresponding dI/dU map of 3.2 ML of Fe on W(001) measured with a Fe-coated W tip are shown in Fig. 6.10(a) and (b), respectively. The sample consists of a 2 ML thick wetting layer, connected patches of the 3rd ML, and 4th ML islands. The dI/dU map at $U = +0.1$ V (b) shows magnetic contrast for both the 3rd and the 4th ML. Again three contrast levels are observed on one layer (3rd ML: $I-III$) and two on the other layer (4th ML: $1,2$) and it is concluded that the sample magnetisation has an angle of 0° and 45° to \vec{M}_t respectively. The derived magnetisation axes for the 3rd and 4th ML are sketched in Fig. 6.10(c). Just as for the 2nd ML, the magnetisation of the 3rd ML encloses an angle of 45° with that of the 4th ML. This leads to the conclusion, that the 3rd ML couples collinearly to the layer underneath, while the layer on top, the 4th ML is magnetised along the other high-symmetry direction of the surface. The collinear coupling between 2nd and 3rd ML is also observed in the measurement shown in Fig. 6.6: the 3rd ML islands indicated by the arrows in (a) show a magnetic contrast in the dI/dU map at $U = -0.8$ V (b) which is hidden to avoid confusion when analysing the 2nd ML regarding the magnetic signal. All 3rd ML islands on top of 2nd ML domains i show a particularly low dI/dU signal. 3rd ML islands on the oppositely magnetised domain iv appear very bright. A medium dI/dU signal is found for 3rd ML islands on top of domain ii while by chance there is no 3rd ML island on domain iii in the image area. The consideration that an antiferromagnetic coupling between the 2nd and the 3rd ML is highly improbable leads to the conclusion that they couple ferromagnetically but possess an opposite spin polarisation at this voltage.

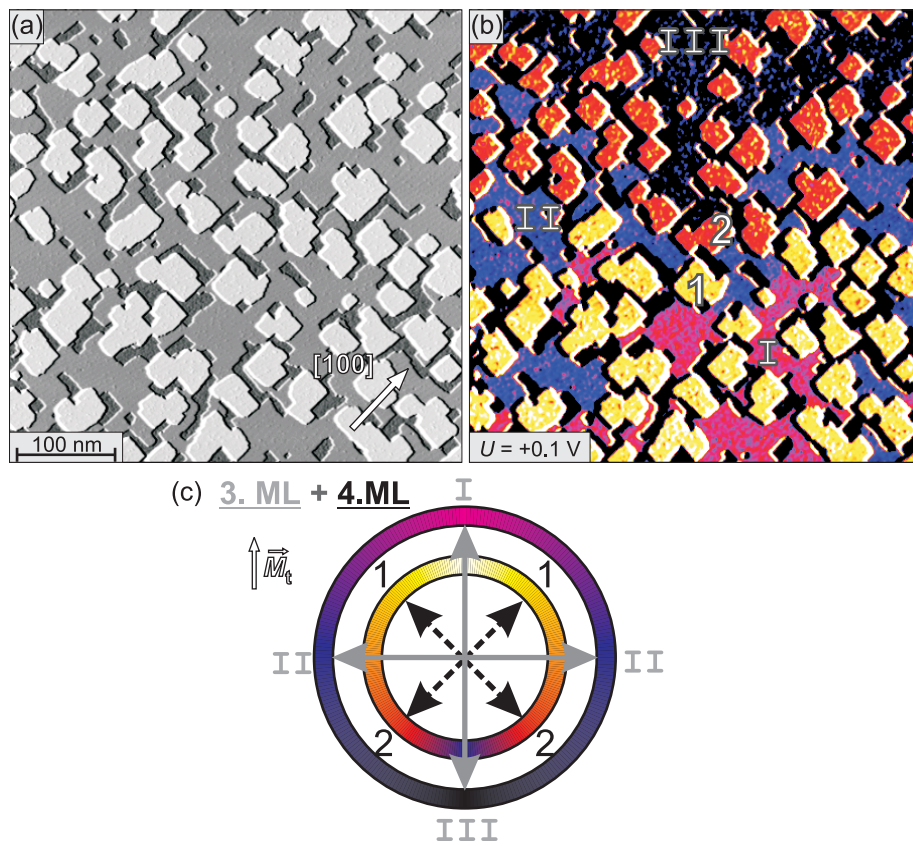


Figure 6.10: Sample of 3.2 ML of Fe on W(001) grown at $T = 525$ K and measured with a Fe-coated W tip. (a) topography; (b) corresponding dI/dU map; (c) sketch of the 45° rotation between 3rd and 4th ML magnetisation.

6.3.4 Magnetism: conclusions

The magnetic measurements show that the 2nd and 3rd ML couple magnetically collinear in moderately annealed samples of Fe on W(001) at a measurement temperature of $T = 13$ K. Even though there have been theoretical calculations that predict an antiferromagnetic monolayer [79], an antiferromagnetic coupling between 2nd and 3rd ML is very unlikely and ferromagnetic coupling is concluded. The method of SP-STM is not able to determine the absolute direction of the magnetisation and thus interpretations have to rely on measurements reported in the literature. MOKE measurements [71, 77] have found an easy magnetisation axis along $\langle 110 \rangle$ for the pseudomorphic growth regime of Fe on W(001). Comparison to the results presented in this thesis leads to the conclusion that the 2nd and 3rd ML both are magnetised along $\langle 110 \rangle$ directions. SP-STM measurements show that the 4th ML has an easy axis which is rotated by 45° with respect to that of 2nd and 3rd ML. Thus the easy magnetisation axis of the 4th ML is $\langle 100 \rangle$. These results are illustrated in Fig. 6.11.

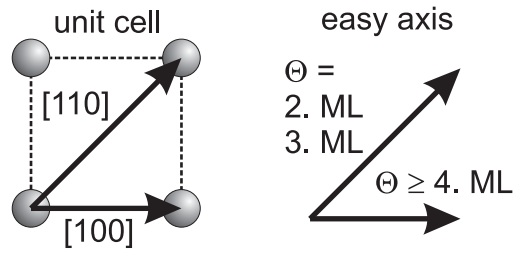


Figure 6.11: Sketch of the surface unit cell of pseudomorphic Fe on W(001) together with the coverage-dependent easy magnetisation axes.

Chapter 7

Summary and Outlook

In this thesis diverse magnetic phenomena were investigated by scanning tunneling microscopy (STM). The results presented for different iron (Fe) nanostructures on tungsten (W) single crystals prove the applicability of this method to various research fields.

Some questions concerning the magnetic properties of the double-layer Fe on W(110) have been answered. Temperature-dependent measurements with high spatial resolution reveal that the reorientation transition temperature is highest for a coverage close to 2 ML. The influence of the width of the double-layer stripes and the orientation of their long axis with respect to the crystallographic direction was studied. The period of the helical magnetic structure reaches an equilibrium value of approximately 42 nm for stripes wider than approximately half that value. The domain walls always run approximately along the $[1\bar{1}0]$ direction of the surface which can be reproduced by Monte-Carlo simulations and understood on the basis of a simple model.

Standing electron waves resulting from scattering at a potential have been investigated with spin resolution which allows not only the characterisation of the orbital symmetry but also the determination of the spin character of the bands involved in scattering processes. In the vicinity of single oxygen atoms on the double-layer Fe on W(110) highly anisotropic oscillations in the local density of states are observed. Comparison to first-principles spin-resolved electronic structure calculations leads to the conclusion that the electronic states involved in the scattering process are of *d*-like symmetry and minority-spin character. STS measurements with a spin-polarised tip support this assumption, since oscillations in the density of states are observed only on one type of domain which proves that they are indeed highly spin-polarised. It is expected that this method can be applied to a great variety of systems involving spin-polarised electron states at surfaces.

In general it is expected that the symmetry of a scattering state is directly correlated to the symmetry of the crystalline lattice. A preliminary result of the electronic structure around single impurities on a ferromagnetic sample with a fourfold axis normal to the surface is presented in Fig. 7.1. The dI/dU map shows an impurity on the surface of three monolayers of Fe on W(001). Oscillations along the $[110]$ directions of the crystal with fourfold symmetry are observed. Further experimental and theoretical work is necessary to investigate this system in more detail.

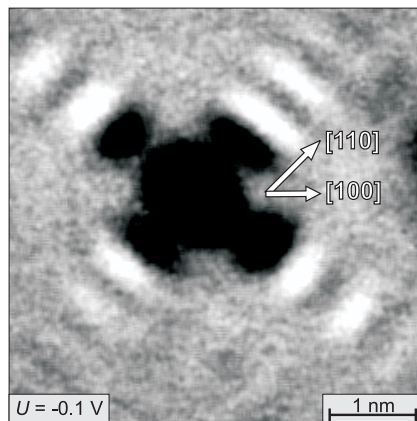


Figure 7.1: dI/dU map of an impurity on 3 ML Fe on W(001) with LDOS oscillations.

The ability of STM to study electronic and magnetic properties of surfaces with high spatial resolution makes it possible to characterise the system of Fe on W(001). A thorough investigation with an emphasis on the low coverage regime was presented. dI/dU spectra reveal the layer dependence of the electronic structure. Depending on local coverage very different features are found which cannot be explained on the basis of STM data. Theoretical calculations of the pseudomorphic regime are required to gain further insight into the character of the spectral features. Spin-polarised STM measurements demonstrated that the sample of pseudomorphic Fe on W(001) with fourfold symmetry breaks up into several magnetic domains on the nanometre scale. The high spatial resolution as well as the magnetic sensitivity allows the investigation of up to eight different dI/dU signal strengths in one image area and thus the direct correlation of magnetisation directions of different layers with respect to the tip magnetisation. The magnetic easy axes in the low coverage regime is found to rotate by 45° from $\langle 110 \rangle$ in layers with a local coverage of 2 and 3 ML, to $\langle 100 \rangle$ at a local coverage of 4 ML. This suggests that further spin-polarised STM measurements will be useful to reach a more detailed understanding of the magnetic state of the monolayer of Fe on W(001) as well. Furthermore theoretical calculations are necessary to investigate the cause of the switching of the easy axis in the low coverage regime.

Bibliography

- [1] F. J. Himpsel, J. E. Ortega, G. J. Mankey, and R. F. Willis, *Adv. Phys.* **47**, 511 (1998).
- [2] C. L. Dennis, R. P. Borges, L. D. Buda, U. Ebels, J. F. Gregg, M. Hehn, E. Jouguelet, K. Ounadjela, I. Petej, I. L. Prejbeanu, et al., *J. Phys.: Condens. Matter* **14**, R1175 (2002).
- [3] H. C. Manoharan, C. P. Lutz, and D. M. Eigler, *Nature* **403**, 512 (2000).
- [4] G. A. Fiete, J. S. Hersch, E. J. Heller, H. C. Manoharan, C. P. Lutz, and D. M. Eigler, *Phys. Rev. Lett.* **86**, 2392 (2001).
- [5] J. Kliewer, R. Berndt, and S. Crampin, *New Journ. Phys.* **22**, 1 (2001).
- [6] M. A. Schneider, L. Vitali, N. Knorr, and K. Kern, *Phys. Rev. B* **65**, 121406(R) (2002).
- [7] R. Allenspach, M. Stampanoni, and A. Bischof, *Phys. Rev. Lett.* **65**, 3344 (1990).
- [8] R. Allenspach and A. Bischof, *Phys. Rev. Lett.* **69**, 3385 (1992).
- [9] J. Thomassen, F. May, B. Feldmann, M. Wuttig, and H. Ibach, *Phys. Rev. Lett.* **69**, 3831 (1992).
- [10] U. Gradmann, in *Handbook of Magnetic Materials*, edited by K. H. J. Buschow, Elsevier, Amsterdam (1993).
- [11] M. Speckmann, H. P. Oepen, and H. Ibach, *Phys. Rev. Lett.* **75**, 2035 (1995).
- [12] J. Hauschild, U. Gradmann, and H. J. Elmers, *Appl. Phys. Lett.* **72**, 3211 (1998).
- [13] S. Pütter, H. F. Ding, Y. T. Millev, H. P. Oepen, and J. Kirschner, *Phys. Rev. B* **64**, 092409 (2001).

-
- [14] M. Bode, A. Kubetzka, O. Pietzsch, and R. Wiesendanger, *Appl. Phys. A* **72**, S149 (2001).
- [15] A. Wachowiak, J. Wiebe, M. Bode, O. Pietzsch, M. Morgenstern, and R. Wiesendanger, *Science* **298**, 577 (2002).
- [16] A. Yamasaki, W. Wulfhekel, R. Hertel, S. Suga, and J. Kirschner, *Phys. Rev. Lett.* **91**, 127201 (2003).
- [17] R. Wiesendanger, *Scanning Probe Microscopy and Spectroscopy*, Cambridge University Press (1994).
- [18] J. Bardeen, *Phys. Rev. Lett.* **6**, 57 (1961).
- [19] J. Tersoff and D. R. Hamann, *Phys. Rev. B* **31**, 805 (1985).
- [20] J. Li and W.-D. S. R. Berndt, *Phys. Rev. B* **56**, 7656 (1997).
- [21] J. C. Slonczewski, *Phys. Rev. B* **39**, 6995 (1989).
- [22] A. Kubetzka, O. Pietzsch, M. Bode, and R. Wiesendanger, *Appl. Phys. A* **76**, 873 (2003).
- [23] O. Pietzsch, A. Kubetzka, D. Haude, M. Bode, and R. Wiesendanger, *Rev. Sci. Instr.* **71**, 424 (2000).
- [24] M. Bode, R. Pascal, and R. Wiesendanger, *Surf. Sci.* **344**, 185 (1995).
- [25] W. Wulfhekel, F. Zavaliche, R. Hertel, S. Bodea, G. Steierl, G. Liu, J. Kirschner, and H. P. Oepen, *Phys. Rev. B* **68**, 144416 (2003).
- [26] M. Henzler and W. Göpel, *Oberflächenphysik des Festkörpers*, Teubner Studienbücher (1994).
- [27] M. Bode, *Rep. Progr. Phys.* **66**, 523 (2003).
- [28] R. Wiesendanger and M. Bode, *Sol. State Commun.* **119**, 341 (2001).
- [29] A. Kubetzka, M. Bode, O. Pietzsch, and R. Wiesendanger, *Phys. Rev. Lett.* **88**, 057201 (2002).
- [30] H. J. Elmers, J. Hauschild, H. Fritzsche, G. Liu, and U. Gradmann, *Phys. Rev. Lett.* **75**, 2031 (1995).
- [31] T. K. Yamada, M. M. J. Bischoff, T. Mizoguchi, and H. van Kempen, *Appl. Phys. Lett.* **82**, 1437 (2003).

-
- [32] O. Pietzsch, A. Kubetzka, M. Bode, and R. Wiesendanger, Phys. Rev. Lett. **84**, 5212 (2000).
- [33] O. Pietzsch, A. Kubetzka, M. Bode, and R. Wiesendanger, Science **292**, 2053 (2001).
- [34] M. Bode, S. Heinze, A. Kubetzka, O. Pietzsch, X. Nie, G. Bihlmayer, S. Blügel, and R. Wiesendanger, Phys. Rev. Lett. **89**, 237205 (2002).
- [35] M. Bode, A. Kubetzka, S. Heinze, O. Pietzsch, R. Wiesendanger, M. Heide, X. Nie, G. Bihlmayer, and S. Blügel, J. Phys. C **15**, S679 (2003).
- [36] A. Kubetzka, O. Pietzsch, M. Bode, and R. Wiesendanger, Phys. Rev. B **67**, 020401 (2003).
- [37] <http://www.webelements.com>.
- [38] H. Bethge, D. Heuer, C. Jensen, K. Reshöft, and U. Köhler, Surf. Sci. **331–333**, 878 (1995).
- [39] M. Bode, *Strukturelle und lokale elektronische Eigenschaften ultradünner Eisenfilme auf W(110)*, Dissertation, Universität Hamburg (1996).
- [40] A. Kubetzka, O. Pietzsch, M. Bode, and R. Wiesendanger, Phys. Rev. B **63**, 140407(R) (2001).
- [41] P. J. Berlowitz, J.-W. He, and D. W. Goodman, Surf. Sci. **231**, 315 (1990).
- [42] N. Weber, K. Wagner, H. J. Elmers, J. Hauschild, and U. Gradmann, Phys. Rev. B **55**, 14121 (1997).
- [43] H. J. Elmers, J. Hauschild, H. Höche, and U. Gradmann, Phys. Rev. Lett. **73**, 898 (1994).
- [44] R. Kurzawa, K.-P. Kämper, W. Schmitt, and G. Güntherodt, Sol. State Commun. **60**, 777 (1986).
- [45] M. Bode, O. Pietzsch, A. Kubetzka, and R. Wiesendanger, J. Electr. Spectr. Relat. Phenom. **114**, 1055 (2001).
- [46] H. J. Elmers, J. Hauschild, and U. Gradmann, Phys. Rev. B **59**, 3688 (1999).
- [47] H. J. Elmers, J. Hauschild, and U. Gradmann, J. Magn. Magn. Mater. **221**, 219 (2000).
- [48] E. Y. Vedmedenko, A. Kubetzka, K. von Bergmann, O. Pietzsch, M. Bode, J. Kirschner, H. P. Oepen, and R. Wiesendanger, Phys. Rev. Lett. **92**, 077207 (2004).

- [49] A. Kubetzka, *Spinpolarisierte Rastertunnelmikroskopie an magnetischen Nanostrukturen: Fe/W(110)*, Dissertation, Universität Hamburg (2002).
- [50] R. B. Muniz, A. T. Costa, and D. L. Mills, *J. Phys. C* **15**, S495 (2003).
- [51] <http://www.chiral.com>.
- [52] J. March, *Advanced organic chemistry*, Wiley, 4th ed. (1992).
- [53] G. P. Lopinski, D. J. Moffatt, D. D. M. Wayner, and R. A. Wolkow, *Nature* **392**, 909 (1998).
- [54] M. O. Lorenzo, C. J. Baddeley, C. Muryn, and R. Raval, *Nature* **404**, 376 (2000).
- [55] A. Kühnle, T. R. Linderoth, B. Hammer, and F. Besenbacher, *Nature* **415**, 891 (2002).
- [56] R. Fasel, M. Parschau, and K.-H. Ernst, *Angew. Chem. Int. Ed.* **42**, 5178 (2003).
- [57] M. F. Crommie, C. P. Lutz, and D. M. Eigler, *Nature* **363**, 524 (1993).
- [58] J. Li, W.-D. Schneider, R. Berndt, O. R. Bryant, and S. Crampin, *Phys. Rev. Lett.* **81**, 4464 (1998).
- [59] O. Jeandupeux, L. Bürgi, A. Hirstein, H. Brune, and K. Kern, *Phys. Rev. B* **59**, 15926 (1999).
- [60] B. G. Briner, P. Hofmann, M. Doering, H.-P. Rust, E. W. Plummer, and A. M. Bradshaw, *Phys. Rev. B* **58**, 13931 (1998).
- [61] J. I. Pascual, Z. Song, J. J. Jackiw, K. Horn, and H.-P. Rust, *Phys. Rev. B* **63**, 241103(R) (2001).
- [62] O. Y. Kolesnychenko, R. de Kort, M. I. Katsnelson, A. I. Lichtenstein, and H. van Kempen, *Nature* **415**, 507 (2002).
- [63] W. Erley and H. Ibach, *Sol. State Commun.* **37**, 937 (1981).
- [64] J. Braun, C. Math, A. Postnikov, and M. Donath, *Phys. Rev. B* **65**, 184412 (2002).
- [65] P. Hofmann, B. G. Briner, M. Doering, H.-P. Rust, E. W. Plummer, and A. M. Bradshaw, *Phys. Rev. Lett.* **79**, 265 (1997).
- [66] L. Petersen, P. Laitenberger, E. Lægsgaard, and F. Besenbacher, *Phys. Rev. B* **58**, 7361 (1998).

-
- [67] L. Petersen, B. Schaefer, E. Lægsgaard, I. Stensgaard, and F. Besenbacher, *Surf. Sci.* **457**, 319 (2000).
- [68] M. Heide, group of Prof. S. Blügel, Institut für Festkörperforschung, Forschungszentrum Jülich (2003).
- [69] J. Chen, M. Drakaki, C. A. Ballentine, and J. L. Erskine, *Bull. Amer. Phys. Soc.* **35**, 199 (1989).
- [70] R. L. Fink, G. A. Mulhollan, A. B. Andrews, J. L. Erskine, and G. K. Walters, *J. Appl. Phys.* **69**, 4986 (1991).
- [71] G. A. Mulhollan, R. L. Fink, J. L. Erskine, and G. K. Walters, *Phys. Rev. B* **43**, 13645 (1991).
- [72] J. Chen and J. L. Erskine, *Phys. Rev. Lett.* **68**, 1212 (1992).
- [73] H. J. Elmers and J. Hauschild, *Surf. Sci.* **320**, 134 (1994).
- [74] T. L. Jones and D. Venus, *Surf. Sci.* **302**, 126 (1994).
- [75] D. Venus and H. L. Johnston, *Phys. Rev. B* **50**, 15787 (1994).
- [76] M. Plihal, D. L. Mills, H. J. Elmers, and U. Gradmann, *Phys. Rev. B* **51**, 8193 (1995).
- [77] W. Wulfhekel, F. Zavaliche, F. Porrati, H. P. Oepen, and J. Kirschner, *Europhys. Lett.* **49**, 651 (2000).
- [78] J. A. Stroschio, D. T. Pierce, A. Davies, R. J. Celotta, and M. Weinert, *Phys. Rev. Lett.* **75**, 2960 (1995).
- [79] R. Wu and A. J. Freeman, *J. Magn. Magn. Mater.* **127**, 327 (1993).

Publications

- K. von Bergmann, M. Bode, A. Kubetzka, M. Heide, S. Blügel, and R. Wiesendanger, *Spin-Polarized Electron Scattering at Single Oxygen Adsorbates on a Magnetic Surface*, Phys. Rev. Lett. **92**, 046801 (2004).
- E. Y. Vedmedenko, A. Kubetzka, K. von Bergmann, O. Pietzsch, M. Bode, J. Kirschner, H. P. Oepen, and R. Wiesendanger, *Domain Wall Orientation in Magnetic Nanowires*, Phys. Rev. Lett. **92**, 077207 (2004).
- K. von Bergmann, M. Bode, and R. Wiesendanger, *Magnetism of iron on tungsten (001) studied by spin-resolved scanning tunneling microscopy and spectroscopy*, submitted to Phys. Rev. B.

Conferences

- 13.03.2002
K. von Bergmann, M. Bode, M. Getzlaff, A. Kubetzka, O. Pietzsch, R. Wiesendanger, *Temperaturabhängigkeit der magnetischen Struktur von 2 ML Fe auf W(110)*, Frühjahrstagung der Deutschen Physikalischen Gesellschaft, Regensburg, Germany (talk).
- 09.09.2002
K. von Bergmann, M. Bode, M. Getzlaff, A. Kubetzka, O. Pietzsch, R. Wiesendanger, *Investigation of Magnetism by Scanning Tunneling Microscopy on the System Fe/W(110)*, 3rd International Conference on Inorganic Materials, Konstanz, Germany (poster).
- 28.03.2003
K. von Bergmann, M. Bode, A. Kubetzka, O. Pietzsch, R. Wiesendanger, *Influence of isolated oxygen adsorbates on the local electronic structure of 2 ML Fe/W(110)*, Frühjahrstagung der Deutschen Physikalischen Gesellschaft, Dresden, Germany (talk).
- 21.07.2003
K. von Bergmann, M. Bode, A. Kubetzka, O. Pietzsch, R. Wiesendanger, *Spin-Polarised Friedel oscillations on 2 ML Fe on W(110)*, 12th International Conference on Scanning Tunneling Microscopy, Eindhoven, Netherlands (talk).
- 08.03.2004
K. von Bergmann, M. Bode, R. Wiesendanger, *Magnetism of Fe on W(001)*, Frühjahrstagung der Deutschen Physikalischen Gesellschaft, Regensburg, Germany (talk).

Acknowledgements

Sincere thanks to all who contributed to this work.
In particular I would like to acknowledge:

- *Prof. Wiesendanger* not only for the chance to do research in his group, but also for his accomplishment to enforce my admission to the PhD-procedure.
- *Prof. Johnson* and *Prof. Oepen* who agreed to referee this thesis and the disputation, respectively.
- *Dr. Mathias Getzlaff* for the supervision until his transfer.
- *Dr. Matthias Bode* for the supervision, help with applied and theoretical problems and for proofreading this thesis.
- *Dr. André Kubetzka* and *Dr. Oswald Pietzsch* for technical assistance with the cryo-STM and fruitful discussions.
- *Marcus Heide* for the spin-resolved electronic structure calculations and *Dr. Elena Vedmedenko* for the Monte-Carlo simulations.
- *Torben Hänke* for providing some of his computer capacity including the required knowledge.
- everyone else from *Group R* not mentioned by name.
- *Mike* for the important things in life.
- my family: *Jens*, *Jutta* and *Klaus* for everything.